A Novel View on the Early Stage of Crystallization

Dissertation zur Erlangung des akademischen Grades

„doctor rerum naturalium“

(Dr. rer. nat.)

in der wissenschaftlichen Disziplin Physikalische Chemie

Eingereicht an der

mathematisch-naturwissenschaftlichen Fakultät

der Universität Potsdam,

angefertigt am

Max-Planck-Institut für Kolloid- und Grenzflächenforschung Potsdam

von Denis Gebauer

Potsdam, 14.04.2008

Selbstständigkeitserklärung

Ich erkläre, dass ich die vorliegende Arbeit an keiner anderen Hochschule eingereicht sowie selbstständig und nur mit den angegebenen Mitteln angefertigt habe.

Ort, Datum	Unterschrift des Verfassers

Contents

Οιδα ουκ ειδωζ…

Vorwort

“Ich weiß, dass ich nichts weiß…!“ Dieses geflügelte Wort aus der Apologie Platons wird als verfälschtes Zitat dem Philosophen Sokrates zugeschrieben. Es mag abgegriffen erscheinen und doch steht es –wie ich finde- in direktem Bezug zur Wissenschaft im Allgemeinen und zur Doktorarbeit im Besonderen: Eine solche Arbeit wird eigentlich nie fertig. Man beginnt, Neues zu verstehen, das Wissen wächst. Gleichzeitig jedoch wirft man neue Fragen auf, die das erlangte Wissen zwar nicht unbedingt in Zweifel stellen aber es in der Quantität zumeist übersteigen. Das mag abschreckend klingen, für mich aber liegt genau in dieser Eigenschaft der Wissenschaft der Reiz, und eine Doktorarbeit muss einfach für abgeschlossen erklärt werden, wenn die Zeit dafür gekommen ist.

Diese Arbeit entstand im Zeitraum vom Winter 2005 bis Frühjahr 2008 am Max-Planck-Institut für Kolloid- und Grenzflächenforschung in der Abteilung Kolloidchemie. Unserem Direktor Prof. Dr. Markus Antonietti möchte ich dafür danken, dass er mir die Möglichkeit gegeben hat, diese Arbeit in seiner Abteilung anzufertigen. Mein besonderer Dank gilt seiner stetigen Unterstützung, der Zuversicht in das Gelingen der Arbeit sowie der hilfreichen Diskussionen.

Meinem Gruppenleiter PD Dr. Helmut Cölfen möchte ich für die Betreuung dieser Arbeit danken, für sein jederzeit offenes Ohr, seine Ratschläge, viele Diskussionen und nicht zuletzt für sein Vertrauen in meine Arbeit.

Dr. Klaus Tauer und Prof. Dr. Peter Fratzl möchte ich für die Diskussionen über die Theorie zur Nukleation danken.

Ich danke Prof. Dr. Matthias Epple und Dr. Jens Rieger für ihre Bereitschaft, Gutachter dieser Arbeit zu sein.

Meinen Bürokollegen Dr. Ruiqi Song und Engin Karabudak und meiner Laborkollegin Antje Völkel möchte ich für eine sehr angenehme und ruhige Arbeitsatmosphäre und gleichzeitig viele, viele Lacher danken.

Ferner gibt es viele weitere Personen, bei denen ich mich für ihre Hilfe bedanken möchte: Antje für gleichsam virtuose AUZ Experimente, Ingrid Zenke für die nette Hilfe bei WAXS Messungen, Rona Pitschke für viele, kreative SEM und TEM Messungen und Dr. Jürgen

Hartmann für die TEM Einweisung. Joachim Thomas und Thomas Ketterer von der Deutschen Metrohm danke ich für ihre apparative Hilfestellung. Außerdem geht mein herzlicher Dank für ihre Hilfe an Margit Barth und Andreas Kretschmar, René Genz und Marco Henning.

Für viele schöne Momente abseits der Arbeit möchte ich Anna, Andreas, Jörg, Jens, Micha, Nicole, Sille und Erich C. danken.

Zum Schluss möchte ich meiner Familie und meinen Freunden danken. Ohne Euch wäre ich erst gar nicht so weit gekommen.

1 Introduction

Crystals are part of both biological and geological Nature, and their beauty has probably fascinated human kind since its origin. Selected examples of crystal beauty are shown in Figure 1.1: Scale (left) is a crystalline conglomerate of pure non-living background, which forms in water boilers, e.g. Protein crystals (middle) provide a basis of the analysis of protein folding in structural biology, and coccoliths (right) –calcium carbonate crystals that form the exoskeleton of some plankton algae- are of pure biological origin.

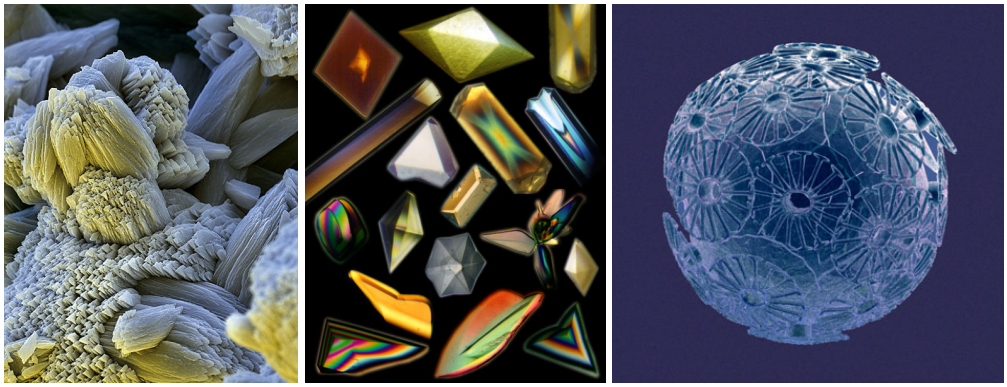

Figure 1.1: Crystal beauty; left: scale ($CaCO_3$), image taken from [1]; middle: protein crystals grown in space, image taken from [2]; right: $CaCO_3$ crystals –coccoliths- form the exoskeleton of some plankton algae, image taken from [3].

For chemists, crystals are not just of fascinating beauty but also part of daily business as many employed solid compounds are crystalline, and crystallization is used for purification and isolation. Of course, there is a classical view on crystallization, which is presented in textbooks, e.g. [4], and in a huge number of scientific publications. Here, the process of crystallization is subdivided into nucleation and crystal growth. In the classical picture, nucleation is considered to take place in a solution of ions or molecules exceeding a critical supersaturation or concentration leading to the nucleation of the new phase *via* stochastic solute clustering [5-8]. The growth of nucleated particles and crystals is then considered to take place *via* addition of single ions or molecules. Historically, nucleation theory was derived for droplet formation in supersaturated vapor and has been transferred to crystallization for the reason of both obvious and ostensible similarity [9]. However, the concept of classical nucleation theory in the view of crystallization is challenged by

mesocrystal formation -so called non-classical crystallization [10-12]- and biomineralization [13-15].

Mesocrystals is used as abbreviation for mesoscopically structured crystals. An example is given by helical fibers of barium carbonate illustrated in Figure 1.2, which are grown in presence of a double hydrophilic block copolymer [16]. The proposed mechanism of mesocrystal formation works *via* parallel crystallization towards amorphous intermediates followed by crystalline nanostructures, which act as material deposits and intermediates for the arrangement and densification towards the final mesocrystalline structure. This means that there is another reaction channel than classically discussed, which allows for the freedom to form complex crystals such as biominerals.

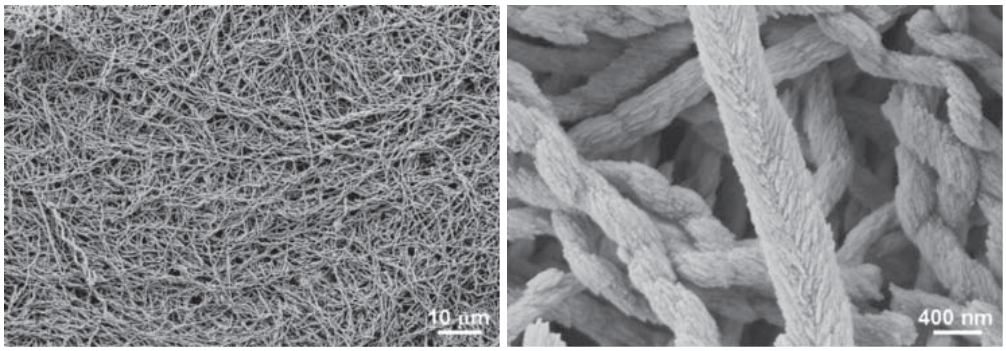

Figure 1.2: Example of mesocrystals: Helical barium carbonate fibres grown in presence of a double hydrophilic block copolymer; left: overview, right: illustration of the fibre surface. Scanning electron microscopy images taken from [16].

Biomineralization refers to the processes by which organisms from bacteria to single-celled protists, plants, invertebrates and vertebrates precipitate and form inorganic materials. Biominerals are often iso-oriented crystal structures with amazingly complex morphologies like coccoliths [17] (cp. Figure 1.1). Recently, there is increasing evidence that biomineralization takes place *via* the colloidal pathways of non-classical crystallization utilizing amorphous precursor species as reported for sea urchin spines [18]. Retrosynthesis of nacre -which is a structure of pseudo-hexagonal aragonite platelets of 5 µm - 15 µm diameter and 0.5 µm height embedded in an organic matrix like a three-dimensional wall of bricks- could be achieved utilizing biological nacre matrix, which was filled with amorphous calcium carbonate precursors that transform mesoscopically into calcite [19].

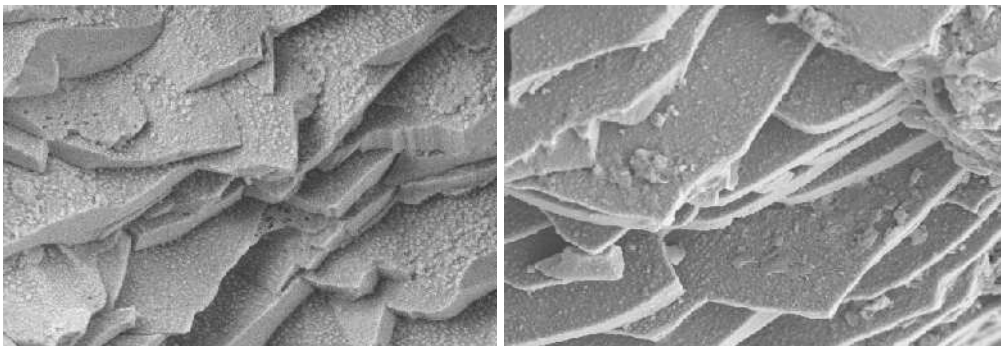

Figure 1.3: Fracture edge of retro-synthesized nacre (left) and biological nacre (right). Scanning electron microscopy images taken from [19].

As illustrated in Figure 1.3, the structures of retro-synthesized and biological nacre platelets are hardly distinguishable, suggesting that the biological formation of nacre works analogously.

Consideration of mesocrystal formation and biomineralization raises the question if the classical molecule- or ion-mediated and the non-classical particle-mediated crystallization path can be unified [20]. In this regard, it is crucial to note that a non-classical crystalline assembly might not be recognized, because a mesocrystal can scatter like a classical single-crystal making classical/non-classical differentiation very difficult. A better question is: Is classical theory of crystallization applicable at all? Figure 1.4 (taken from [21]) emphasizes the important unanswered questions during the process of particle formation.

Starting from homogeneous solution, the question raises, if homogeneous supersaturation as considered in classical theory is achievable, are there precursor species that form prior to critical nuclei? If such precursors exist, is the concept of critical nuclei applicable? What is then the structure of 'critical nuclei'? How do 'critical nuclei' determine the structure of intermediate stages, which are a requisite for mesoscopically structured particles? How can the structure formation of the final particles then be controlled by the process and/or additives?

This thesis is considered to pave the way to an answer to these questions, while calcium carbonate is chosen as a model system of crystallization. Calcium carbonate, which is the major source of water hardness, is one of the most frequently studied minerals, with great scientific relevance in biomineralization and geosciences forming enormous scales of biological (reefs, ocean sediments) and geological origin. Calcium carbonate sediments bind an immense amount of CO_2 and affect the chemistry of ocean water, and with it, the earth's

atmosphere and climate. Scale formation (incrustation) is also a serious issue in daily life, industry and technology, and the addition of scale inhibitors to laundry detergents, household cleaners but also in many industrial applications is necessary.

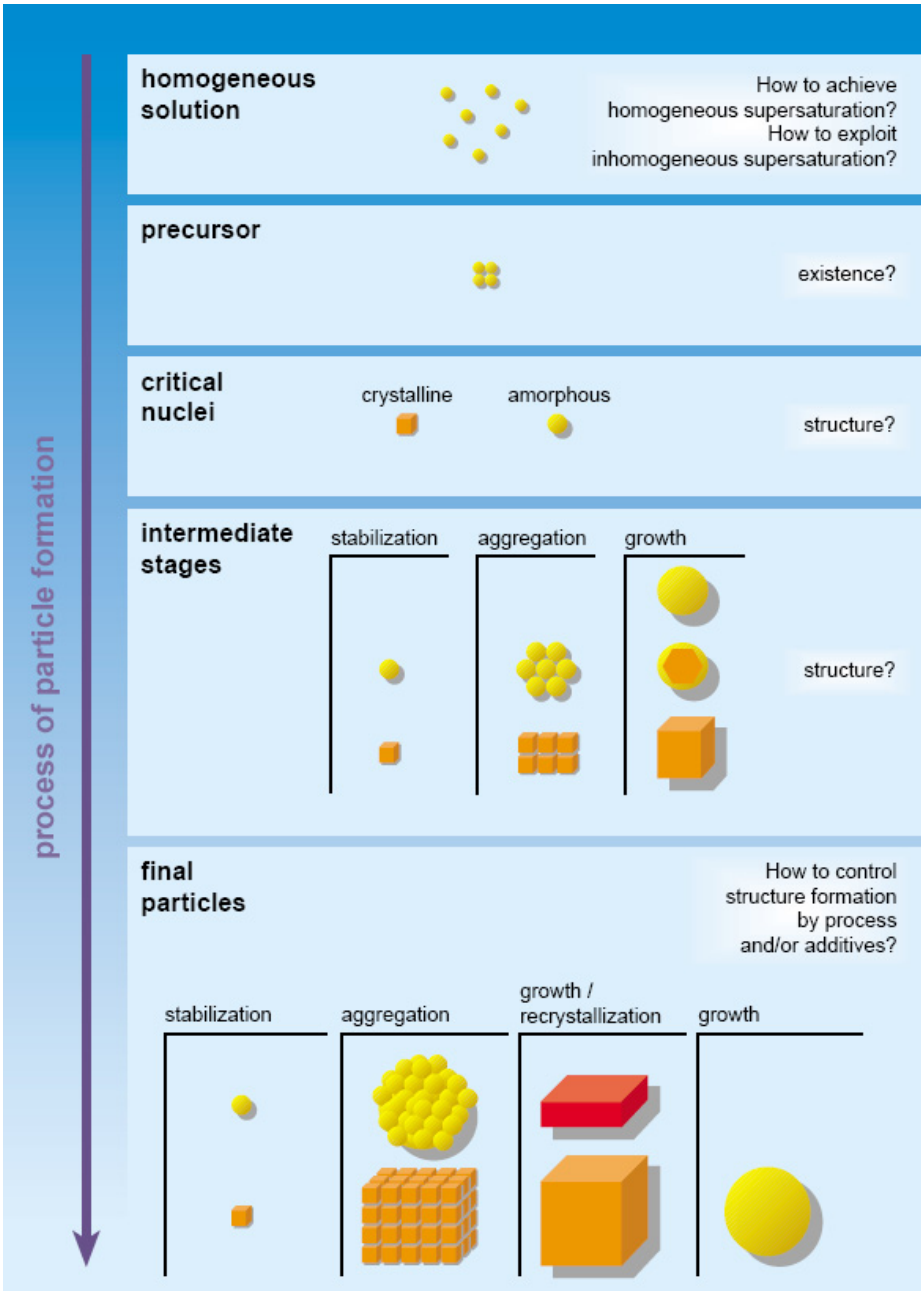

Figure 1.4: The process of particle formation starting at a homogeneous solution and ending with the final particles emphasizing intermediate stages and raised questions taken from [21]. For explanations see text.

The brilliance of dishes or softness of clothes is a question of comfort, but continuous scale formation also lowers the technical efficiency of heating devices and finally results in machine damage. Water hardness causes enormous costs –which have been estimated to be

about $50 billion per year for the industrial world overall [22], or 0.25% of the countries' gross national product. However, despite of these enormous economical and ecological consequences, the molecular mechanism of scale formation and the molecular basis for the reduction or prevention of scaling are yet not fully understood.

$CaCO_3$ has been studied for more than a century now but nevertheless, little is known about the very early stages of its crystallization. Amorphous calcium carbonate (ACC) is identified as a precursor phase in bio- [23] and biomimetic mineralization [24] and liquid precursors (PILP) have been identified in some cases [25]. Precursor species that form still earlier -i.e. directly after ion contact- have been postulated as indicated above, but could not yet be revealed [26] due to limitations of the applied analytical techniques. Even fast synchrotron scattering utilizing a stopped flow mixing technique directly monitors only ACC formation [27], and polycarboxylates like polyaspartic acid just inhibit crystallization [28, 29] and work as scale inhibitors. Because of the classical picture of nucleation, the target of scale inhibitors has been ions and small nucleated particles. However, there is an increasing evidence that small inorganic polymeric species and clusters rather than ions play a dominant role in the pre-nucleation stage of biomineralization and the formation of organic nanoparticles [21, 30]. Such soluble cluster-species have been reported for the polycondensation of silicic acid [31], precipitation of aluminum oxyhydroxide [32] and aqueous solutions of hydrated ions of the transition metals iron, chromium, uranium, molybdenum and tungsten [33]. In the above examples, the pre-nucleation cluster formation is a polymerization-like event, since the chemical bonds formed are mostly covalent (silica) to partly ionic (transition metals). For non-polymerizing ionic crystals, solute clustering has only been reported for highly soluble compounds such as citric acid, urea, sodium nitrate and potassium sulphate at high supersaturation [34]. Cluster formation for low concentrations, i.e. under-saturated and slightly supersaturated ionic solutions, has not yet been reported.

This thesis presents an accurate description of the pre-nucleation, nucleation and particle growth stages of calcium carbonate by a series of critical experiments in both absence and presence of additives. These show that metastable pre-nucleation species of $CaCO_3$ are neutral clusters of proximately averaged constant size and not charged ions, while the clusters are even present in undersaturated solution. This not only changes the view on crystallization but also has deep consequences for the interaction of the early $CaCO_3$ clusters

with additives like scale inhibitors or biomolecules in Biomineralization as well as CO_2 binding in carbonates as such.

The thesis is organized as follows: Section 2 addresses nucleation theory - both the classical and non-classical approach- in a rather pronounced manner emphasizing the particular weak points. Section 3 gives an overview of applied methods. Section 4 introduces the experimental procedures, while section 5 presents experimental results and discussion of calcium carbonate precipitation in absence and presence of additives. Section 6 summarizes the results and emphasizes the impact on nucleation theory introducing a precipitation scenario of calcium carbonate complying with the experimental results; further on, it gives an outlook on future work suggested by remaining questions.

2 Nucleation Theory

Nucleation –the initiation of a phase transformation- is a major concern of this thesis while nucleation theories provide a basis for the understanding of nucleation phenomena giving a model for the evaluation of experimental data. Nucleation theory distinguishes homogeneous and heterogeneous nucleation. Homogeneous nucleation is considered to take place in the volume of a supersaturated phase via stochastic formation of particle clusters, i.e. nuclei, whereas nucleus formation in heterogeneous nucleation is considered to take place on existing extrinsic interfaces. The interaction of nuclei and interfaces in heterogeneous nucleation lowers the free energy of nucleus formation and heterogeneous nucleation takes place at lower supersaturation if compared to homogeneous nucleation. This overview of nucleation theory is presented for the homogeneous case mainly following [35].

Nucleation was quantitatively treated for the first time by VOLMER and WEBER in 1926 [5]. This work was based on ideas of GIBBS in 1877. The theory was further improved by FARKAS [36] in 1927 and by BECKER and DÖRING in 1935 [8]. The work of BECKER and DÖRING is commonly designated classical nucleation theory (CNT) and has been modified on various occasions –e.g. [37], [38] or [39]- in both physically exact and empirical manner. However, CNT is rarely capable of a quantitative description of experimental data and can only give a qualitative description of nucleation. The major desideration of CNT is the assumption that even very small nuclei of a nascent phase can be described as if they were macroscopic; this assumption is known as the "capillarity assumption".

According to [40], the quantitative approach avoiding this assumption is designated non-classical nucleation theory (NCNT). Such an approach is the density-functional approach, which was first employed by CAHN and HILLIARD [41] on nucleation in two-component incompressible fluids in 1959. Analogously to CNT, this work was modified and improved -see e.g. review articles [42], [43], [44].

Both CNT and NCNT provide a basis for a different approach to understanding nucleation -the modeling or simulation approach. Here, CNT provides the basis of a macroscopic modeling of nucleation, i.e. the evolution of sharp interfaces, while NCNT provides a mesoscopic approach describing the evolution of smooth interfaces with a finite length.

Finally, the most precise approach is given by the description of an interface at the atomic level. An important class of microscopic models is based on the kinetic ISING model utilizing interacting energies at the atomic level.

CNT is described rather detailed in the following section, because it is still the most frequently applied theory in physico-chemical characterization. NCNT is described briefly in order to introduce the concept and point out the difference to CNT. Modeling and simulation are left out because they exceed the coverage of an experimental, physico-chemical work.

2.1 Classical Nucleation Theory

2.1.1 Basic Concept

The driving force of phase transformation at constant pressure is the change in GIBBS free energy

$$-\frac{\Delta_R G_{p.t.}}{N} = \Delta\mu = \mu_{old} - \mu_{new} \,. \tag{2.1}$$

μ_{new} is the chemical potential of the calcium carbonate solution in presence of nucleated, solid calcium carbonate and μ_{old} is the chemical potential of the ionic calcium carbonate solution before nucleation occurs, and N is the number of ions in the system. Assuming an activity coefficient of dissolved ions close to unity, the chemical potential μ_{old} introduced in equation (2.1) may be written as

$$\mu_{old} = \mu_{eq.} + kT \ln \frac{c\left(Ca^{2+}_{aq.}\right) c\left(CO^{2-}_{3,aq.}\right)}{\left[c\left(Ca^{2+}_{aq.}\right) c\left(CO^{2-}_{3,aq.}\right)\right]_{eq.}}, \tag{2.2}$$

where index eq. indicates the particular values at which the solute and precipitate are in phase equilibrium. $\left[c\left(Ca^{2+}_{aq.}\right) c\left(CO^{2-}_{3,aq.}\right)\right]_{eq.}$ gives the solubility product of the formed calcium carbonate phase, which is amorphous calcium carbonate (cp. section 5). Thus, μ_{new} is practically independent of the solubility product and approximately

$$\begin{aligned}&\mu_{new}\left(c\left(Ca^{2+}_{aq.}\right)c\left(CO^{2-}_{3,aq.}\right)\right)\\&=\mu_{new}\left(\left[c\left(Ca^{2+}_{aq.}\right)c\left(CO^{2-}_{3,aq.}\right)\right]_{eq.}\right)=\mu_{eq.}\end{aligned}\quad (2.3)$$

Introducing the supersaturation ratio $s=\dfrac{c\left(Ca^{2+}_{aq.}\right)c\left(CO^{2-}_{3,aq.}\right)}{\left[c\left(Ca^{2+}_{aq.}\right)c\left(CO^{2-}_{3,aq.}\right)\right]_{eq.}}$, combination of equations (2.1), (2.2) and (2.3) gives for the change in GIBBS energy due to phase transformation in molar dimension

$$\Delta_R G_{p.t.}=-RT\ln s. \quad (2.4)$$

Considering a solution (cp. equation (2.1)) of W 'monomers', which are randomly distributed, this phase has the GIBBS energy

$$G_1=W\mu_{old}. \quad (2.5)$$

The solution may undergo fluctuations forming a cluster containing w (w = 1, 2, …) ions. GIBBS energy of the solution is then

$$G_2(w)=(W-w)\mu_{old}+G(w). \quad (2.6)$$

The first summand is the remainder of the solution surrounding the cluster, whereas G(w) is GIBBS energy of a w-sized cluster. This summand is

$$G(w)=w\mu_{new}+\gamma(w)A(w). \quad (2.7)$$

Here, the second summand accounts for an energy excess of the formed clusters due to less and weaker bonds of ions in the surface layer, whereas $\gamma(w)$ is the surface GIBBS energy of a cluster of size w and $A(w)$ is the surface of a cluster of size w.

Combination of equations (2.4), (2.5), (2.6) and (2.7) gives the change in GIBBS energy for the formation of a cluster of size w

$$\begin{aligned}&\Delta G_{nucl.}(w)=G_2(w)-G_1\\&=\underbrace{-w\cdot kT\ln s}_{\Delta G_{nucl.,volume}}+\underbrace{\gamma(w)A(w)}_{\Delta G_{nucl.,surface}}.\end{aligned}\quad (2.8)$$

As indicated, the first summand gives the volume contribution and the second summand the surface contribution to GIBBS energy change for the formation of a nucleus of size w. The volume contribution is negative for a supersaturation ratio s > 1 and the surface contribution is always positive. It is crucial to note that the volume energy is proportional to the cube of the radius of formed clusters and the surface energy is proportional to the square of the radius of formed clusters. Thus, there is a radius at which the change in GIBBS energy for the formation of a cluster of size w exhibits a maximum. This regard is illustrated in Figure 2.1. The parameters defining this special point are classically designated critical parameters. The critical point characterizes a metastable equilibrium since $\frac{\partial[\Delta G_{nucl.}]}{\partial r} = 0$ while $\frac{\partial^2[\Delta G_{nucl.}]}{\partial r^2} < 0$. This means that nuclei formed bigger than the critical size will grow without limit and nuclei formed smaller than the critical size will dissolve completely. According to MULLIN [4], the critical GIBBS enthalpy change can be calculated by

$$\Delta G_{nucl.}^{*} = \frac{16\pi \cdot \sigma^3 v^2}{3(kT \cdot \ln s)}, \tag{2.9}$$

assuming a spherical nucleus with molecular volume v and macroscopic surface tension σ of the phase, which will be formed. To escape the metastable state requires a fluctuation to become a critical nucleus, i.e. to overcome the activation barrier for nucleation.
Assuming that nuclei only grow or dissolve *via* addition and subtraction of single solute ions, the nucleation rate $\hat{k}$ is given by the BOLTZMANN approach

$$\hat{k} = \hat{k}_0 \exp\left[-\frac{\Delta G_{nucl.}^{*}}{kT}\right]. \tag{2.10}$$

BECKER and DÖRING [8] express the kinetic pre-factor $\hat{k}_0$ by

$$\hat{k}_0 = v N_w^2 \left[\frac{2\gamma}{\pi \cdot M}\right]^{0.5}, \tag{2.11}$$

where N_w is the number of nuclei of size w and M is the molecular weight.

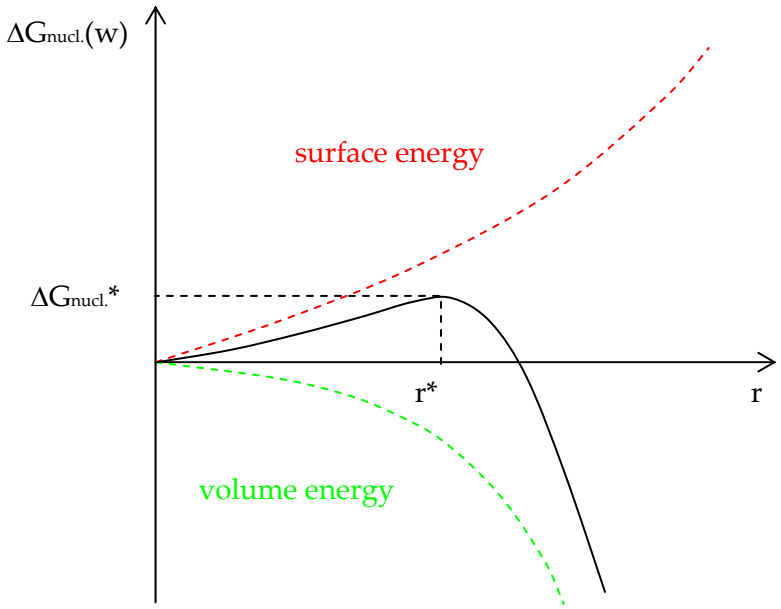

Figure 2.1: Schematic plot of GIBBS energy change due to the formation of a nucleus of size w *versus* the radius of the nucleus r for s > 1 (cp. equation (2.8)). The point at which the volume energy (green line) balances the surface energy (red line) characterizes the critical parameters; here the critical radius r* and the critical GIBBS energy $\Delta G_{nucl.}$*. For further explanations see text.

Two different treatments [45] correct the pre-factor by the reciprocal supersaturation ratio 1/s, however, none of the derivations is capable to fit experimental data satisfactory. Thus, there have been empirical improvements of CNT, which lack a physical basis but are capable to fit experimental data.

The failure of CNT to quantitatively describe experimental data has different reasons. On one hand, there are neglected energy terms within the nucleation process: volume work, entropy effects and hydration/solvation phenomena. The classical derivation accounts only for GIBBS surface energy which is commonly expressed by the macroscopic surface tension, while this dimension is rather ill-defined for small nuclei (cp. equation (2.7) and (2.9)). On the other hand, the theory neglects molecular interactions and collective phenomena, e.g. the fluctuation of concentration. This simplification is introduced with equation (2.5) and therefore, equation (2.8) implies that subcritical cluster formation is thermodynamically impossible –at least at a macroscopic scale. Summarizing, it is important to note that CNT hardly gives a quantitative but rather a qualitative description of nucleation phenomena.

2.1.2 Equilibrium Cluster Size Distribution

As already indicated, the appearance of clusters in classical theory is an "unnatural process" from a thermodynamic point of view. They still do form classically, randomly in both time and space, while this is the way of circumventing the thermodynamic law. An important consequence of this stochastic clustering process is that a temporarily fluctuating and locally different number of clusters of different sizes exist. This number can be averaged over a long enough observation time as well as over the observed volume and then divided by this time and volume giving the time-independent and spatially uniform equilibrium cluster size distribution c(w). It is crucial to note that c(w) is just a theoretical abstraction since the supersaturated solution prior to nucleation can only stay temporarily in the corresponding metastable state.

The stochastic formation of clusters can be considered to be a product of the reaction of 'monomers' X (w = 0, 1, 2,…)

$$w \cdot X \rightleftharpoons (X)_w, \tag{2.12}$$

Considering a mutual equilibrium between all w-mers of all possible sizes, equation (2.12) suitably describes an averaged equilibrium of cluster formation. The thermodynamic condition for chemical equilibrium gives (cp. equation (2.1))

$$w \cdot \mu_{old} = \mu_w . \tag{2.13}$$

Here, μ_w is the chemical potential of a w-mer, which is considered as a separate macromolecule. The chemical potential of a w-mer is related to its chemical potential in a reference one-component phase of only this w-mer. Thus, the chemical potential of all w-mers of different sizes may be written as

$$\mu_w = G(w) + kT \cdot \ln \frac{c(w)}{c_0}, \tag{2.14}$$

where c_0 is the concentration of sites in the system on which clusters of the new phase can form and $G(w)$ is the quantity introduced in equation (2.7). The logarithmic term accounts for the existence of clusters of all sizes by the entropy of mixing. Substituting μ_w from

equation (2.14) in equation (2.13) using equations (2.1), (2.7) and (2.8) gives the equilibrium cluster distribution

$$c(w) = c_0 \exp\left[-\frac{\Delta G_{nucl.}(w)}{kT}\right]. \qquad (2.15)$$

It is obvious from equation (2.15) that the exponent becomes distinctly negative for increasing cluster size in subcritical solution, i.e. most of ions are 'monomers'.

2.2 Non-Classical Nucleation Theory

Critical clusters predicted by classical nucleation theory usually show numbers of $n^* < 100$. This small number raises questions, which cannot be answered by the classical approach: What is a cluster and is there a criterion for the positioning of an interfacial energy? What are the shape, structure and density of such small clusters? Is the specific surface energy independent on the cluster size? What is the physical meaning of the specific surface energy if a cluster has more surface ions than bulk ions? Why is $\Delta G_{nucl.} \neq 0$ at $s = 1$ –while $\lim_{s\to\infty} \Delta G_{nucl.} = 0$ - (cp. equation (2.9)) contradicting the thermodynamic requirement for the annulment of nucleation work at the spinodal?

The atomistic theory of nucleation, e.g. based on the kinetic ISING model, operates with a cluster binding energy rather than with a cluster surface energy and is thus not concerned with the third and the fourth question above; however, it cannot solve the remaining ones. Therefore, a way of dealing with such questions is to follow an approach, which is dispensing with the concept of cluster formation.

A solution of molecules undergoing statistical fluctuations is now considered to undergo a continuous change of the molecule number density ρ_m. $\rho_m(\vec{r})$ is called the density of ions at a point indicated by position vector $\vec{r}$. The spatially constant pressure p of the solution becomes a $\vec{r}$-dependent tensor. The HELMHOLTZ free energy f_H per molecule becomes locally different and is a function of $\vec{r}$, ρ and its derivatives, shortly denoted as $f_H(\vec{r})$. HELMHOLTZ free energy for a system undergoing statistical fluctuations is thus given by

$$F_2\{\rho\} = \int_V f_H(\vec{r})\rho(\vec{r}) \cdot d\vec{r}, \qquad (2.16)$$

with volume V. Using $G = F + pV$, GIBBS free energy can be calculated with

$$G_2\{\rho\} = \int_V \left[f_H\left(\vec{r}\right)\rho\left(\vec{r}\right) + p \right] d\vec{r} \,. \tag{2.17}$$

Equation (2.17) is the non-classical analogue to equation (2.6). The free energy change for a density fluctuation –not cluster formation as considered in equation (2.8)- can be written as

$$\Delta G_\rho = \int_V \left(\left[f_H\left(\vec{r}\right) - \mu_{old} \right] \rho\left(\vec{r}\right) + p \right) d\vec{r} \tag{2.18}$$

Equation (2.18) is the general formula for the free energy change to form a density fluctuation of arbitrary profile in homogeneous nucleation for T = p = const. It is valid for any shape of the density fluctuation and does not assume the formation of an interface and thus does not distinguish between bulk and surface molecules. Thus, it overcomes the limitations affecting CNT. The derivation of μ_{old} in equation (2.18) as well as the modeling of $f\left(\vec{r}\right)$, which requires several assumptions due to considerable mathematical difficulties, clearly exceed the coverage of this thesis.

3 Methods

3.1 Analytical Ultracentrifugation

Analytical Ultracentrifugation (AUC) was invented by THEODOR SVEDBERG in 1923, who won the NOBEL Prize in 1926 for his research on colloids and proteins. The ultracentrifuge is optimized for spinning a rotor at very high speeds providing accelerations up to 10^6 g (acceleration of gravity $g = 9.8\ m\ s^{-2}$). There are preparative and analytical ultracentrifuges, both having important applications in molecular biology, biochemistry and polymer science. The ultracentrifuge utilized in this thesis is an analytical ultracentrifuge Beckman-Coulter XL-I using RAYLEIGH interference optics for the detection of sedimenting species.

The experimental setup is schematically illustrated in Figure 3.1. A sector shaped cell is filled with the sample solution and rotated at angular velocity ω. The cell is sector-shaped in order to avoid sedimentation on the cell walls, i.e. accumulation of concentration, which accompanies convection. The sample solution surface developed against air is the meniscus. A particle –molecule, macromolecule or ion- in the sample solution will at first experience two different forces, the centrifugal force

$$F_c = \omega^2 r \cdot m \tag{3.1}$$

with radial position r and mass of the particle m and a buoyant force

$$F_b = -\omega^2 r \cdot m_0 \tag{3.2}$$

with mass of solution displaced m_0. As a result of these forces, the particle will acquire a velocity v_{AUC} giving rise to a retarding frictional force

$$F_d = -f \cdot v_{AUC} \tag{3.3}$$

with frictional coefficient f. Equilibrium of the different effective forces according to equations (3.1) to (3.3),

$$\begin{aligned} &F_c + F_b + F_d = 0 \\ &\omega^2 r \cdot m - \omega^2 r \cdot m_0 - f \cdot v_{AUC} = 0 \end{aligned}' \tag{3.4}$$

will result in the particle acquiring a constant velocity v_{AUC} just great enough to make the total force zero.

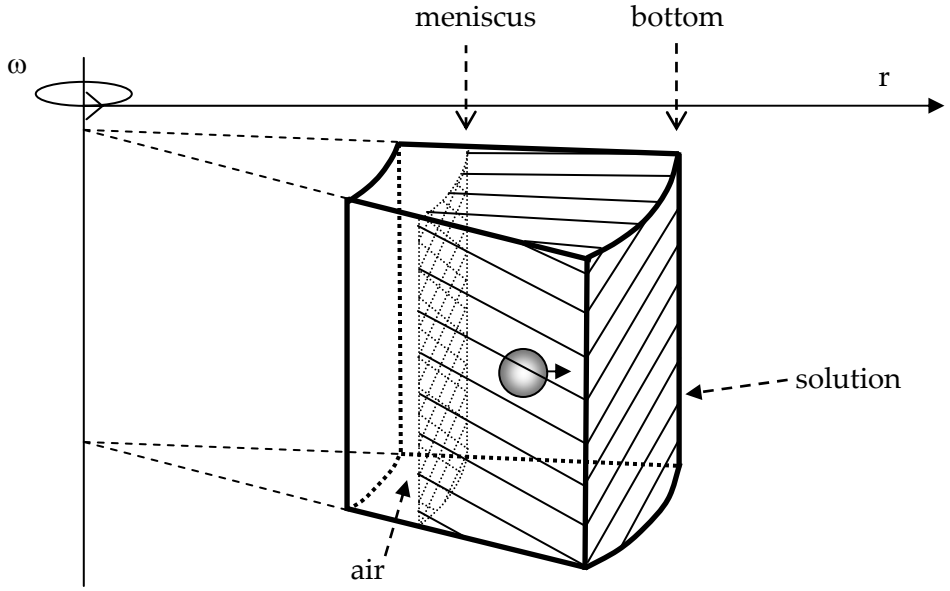

Figure 3.1: Schematical setup of a sedimentation experiment. Not to scale. For explanations see text.

Introducing the partial specific volume $\bar{v}$ of the particle, the density of the solution ρ and AVOGADRO's number N_A, equation (3.4) can be written as

$$(3.5) \qquad s = \frac{v_{AUC}}{\omega^2 r} = \frac{M\left(1-\bar{v}\rho\right)}{N_A f},$$

with molecular weight M giving the sedimentation coefficient s, which is the experimentally accessible ratio of velocity to the centrifugal field strength. The unit of s is seconds, while the quantity of 10^{-13} seconds is called SVEDBERG and conventionally denoted by S. The diffusion coefficient D is given by

$$(3.6) \qquad D = \frac{RT}{N_A f}$$

with gas constant R and temperature T. Combination of equations (3.5) and (3.6) gives the SVEDBERG equation

$$\frac{s}{D} = \frac{M\left(1-\bar{v}\rho\right)}{RT}. \tag{3.7}$$

The sedimentation coefficient cannot yield an unambiguous value for the molecular weight by itself. This is due to the frictional coefficient (cp. equation (3.5)), which depends on size, shape and hydration in a complicated way. The SVEDBERG equation eliminates the frictional coefficient by the diffusion coefficient, which can be measured experimentally. If s and D are measured at (or corrected to) the same conditions, equation (3.7) gives accurate molecular weights.

The sedimentation process is described completely by the LAMM equation (s = const., D = const.)

$$\frac{\partial c}{\partial t} = D\left(\frac{\partial^2 c}{\partial r^2} + \frac{1}{r}\frac{\partial c}{\partial r}\right) - s\cdot\omega^2\left(r\frac{\partial c}{\partial r} + 2c\right) \tag{3.8}$$

with concentration c of the particle. The LAMM equation is explicitly solvable for some boundary conditions, e.g. for a state of equilibrium all over the cell $\frac{\partial c}{\partial t} = 0$ using equation (3.6) gives

$$\frac{\partial \ln c}{\partial x^2} = \frac{M\left(1-\bar{v}\rho\right)}{2RT}\omega^2. \tag{3.9}$$

Equation (3.9) facilitates the determination of the molecular weight in so called sedimentation-diffusion equilibrium experiments. In contrast to sedimentation velocity experiments which usually apply rotor speeds of 60,000 rpm, the rotor rotates at lower speeds of usually around 40,000 rpm depending on the particle size and solution density. Modern Ultracentrifugation evaluation software bases on the LAMM equation (3.8), for example Sedfit by P. SCHUCK, cp. [46, 47].

3.2 Ion Potential Measurement and Titration

3.2.1 Ion Potential Measurement

The basis of the measurement of ion potentials is given by the NERNST equation,

$$U = U^{\otimes} + \frac{RT}{zF_A} \ln \frac{a_{ox.}}{a_{red.}},$$

with reduction potential U, standard reduction potential $U^{\otimes}$, universal gas constant R, temperature T, number of electrons transferred or valency z, Faraday constant F_A, activity of oxidized species $a_{ox.}$ and activity of reduced species $a_{red.}$. In dilute systems, the NERNST equation can be expressed directly in terms of concentration c, because activity coefficients are close to unity, $\ln \frac{a_{ox.}}{a_{red.}} \cong \ln \frac{c_{ox.}}{c_{red.}}$. For the practical measurement of potentials, two electrodes have to be applied –a reference electrode and a measurement electrode. Historically, the reference electrode is the standard hydrogen electrode, which forms the basis of the thermodynamic scale of reduction-oxidation potentials. In practical applications, the construction of standard hydrogen electrodes is rather unhandy. Thus, calomel or silver-silver chloride electrodes are applied predominantly in aqueous electrochemistry. Such reference electrodes have the advantage of a highly stable potential. This is provided by a highly stable concentration of the ions of the electrode electrolyte. For example, the silver-silver chloride electrode consists of a silver electrode in 3 M KCl in presence of silver chloride precipitate. As silver chloride is hardly soluble, the Ag^+ concentration and thus the electrode potential are highly stable.

The principal set-up of a measurement and reference electrode providing ion selectivity is illustrated in Figure 3.2. The reference electrode is electrically connected to the sample solution *via* a diaphragm. It is important that the reference electrode is opened during measurements: Slow out-flux of electrode electrolyte through the diaphragm eliminates in-diffusion of sample ions into the reference electrolyte. Electrode electrolyte of Ag/AgCl electrodes is KCl. Potassium ions are chosen because K^+ and Cl^- have almost equal diffusion coefficients and the development of interfering diffusion potentials is decreased. The key component of the reference electrode/measurement electrode setup is an ion-selective

membrane. The membrane separates two phases, i.e. the internal electrolyte and the sample solution, and if ions can penetrate the boundary between those phases, an electrochemical equilibrium will be reached then forming different potentials in both phases. If the membrane boundary is selective for a single type of ion, the potential difference is governed only by the activity of these ions in the separated phases. The electrochemical line-up can be written as

Ag(s)|AgCl(aq)||membrane||sample solution||diaphragm||AgCl(aq)|Ag(s).

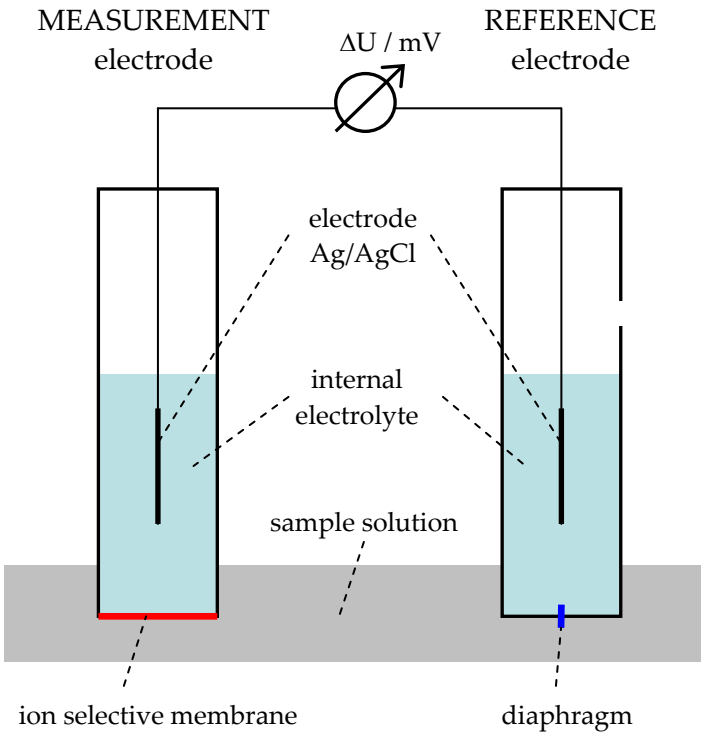

Figure 3.2: Measurement set-up of ion selective electrodes. For explanations see text.

The measured potential is the sum of different potentials generated at all interfaces. The NERNST equation gives for the electrochemical potential of the reference electrode $U_{ref.}$ and of the measurement electrode $U_{meas.}$

$$U_{ref.} = U^{\otimes}_{Ag_s / Ag^+_{aq.}} + \frac{RT}{F_A} \ln \frac{a\left(Ag^+_{aq.}\right)}{a\left(Ag_s\right)}$$

$$U_{meas.} = U^{\otimes}_{Ag_s / Ag^+_{aq.}} + \frac{RT}{F_A} \ln \frac{a\left(Ag^+_{aq.}\right)}{a\left(Ag_s\right)} + U^{\otimes}_{Analyte} + \frac{RT}{z_{Analyte} F_A} \ln \frac{a_{sample\ solution}\left(Analyte\right)}{a_{electrolyte}\left(Analyte\right)}$$

The measured signal is the potential difference

$$\begin{aligned}\Delta U &= U_{\text{meas.}} - U_{\text{ref.}} \\ &= U^{\otimes}_{\text{Analyte}} + \frac{RT}{z_{\text{Analyte}} F_A} \ln \frac{a_{\text{sample solution}}(\text{Analyte})}{a_{\text{electrolyte}}(\text{Analyte})}.\end{aligned} \tag{3.10}$$

If the activity of the analyzed ion in the measurement electrode electrolyte is constant and the sample solution is dilute, equation (3.10) gives

$$\Delta U \cong C + \frac{59.16\ [\text{mV}]}{z_{\text{Analyte}}} \log\left[c_{\text{sample solution}}(\text{Analyte})\right], \tag{3.11}$$

where C is the electrode intercept, which is determined *via* calibration. Here, the theoretical electrode slope at 298 K is maintained within an error of 5 mV for most ion selective electrodes. A distinct deviation indicates insufficient selectivity or damage of the ion selective membrane. However, a membrane exclusively selective for a single type of ion does not exist. The measured potential may be influenced by interfering ions, though. Distinctly interfering ions are taken into account by the NIKOLSKI-EISENMAN equation,

$$\Delta U = C + \frac{59.16\ [\text{mV}]}{z_{\text{Analyte}}} \left[\log\left(c_{\text{Analyte}}\right) + \frac{z_{\text{Analyte}}}{z_2} \log\left(\Phi_2 \cdot c_2\right)\right], \tag{3.12}$$

where index 2 indicates the interfering species and Φ is an empirical selectivity coefficient. An interfering influence of certain ions on a particular ion selective electrode has to be detected experimentally.

A typical calibration curve of an ion selective electrode without any distinctly interfering influence is illustrated in Figure 3.3. For most ion selective electrodes, the range of linear response is in between 10^{-5} M and 10^{-1} M for metal ion electrodes and in between pH = 12 and pH = 2 for most pH-electrodes. The low detection limit is in the order of 10^{-5} M to 10^{-6} M for metal ion electrodes. The interference of cations in the range of low concentrations is caused by imperfection of selectivity as mentioned above. The interference of anions in the range of high concentration is due to physicochemical non-ideality, i.e. the activity coefficient distinctly differs from 1 and cation/anion clusters are formed.

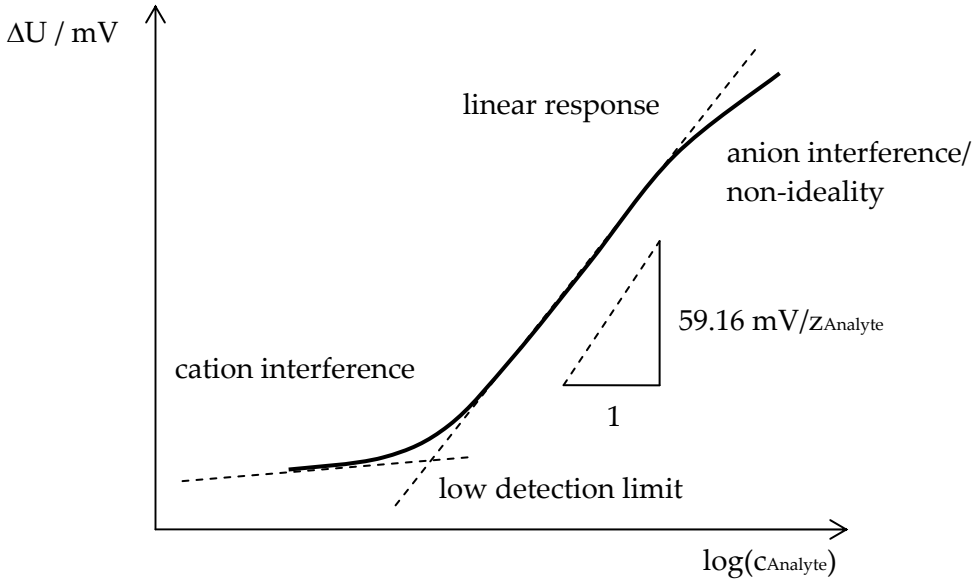

Figure 3.3: Typical calibration curve of ion selective electrodes. For explanations see text.

There are three main types of ion selective membranes: solid membrane (e.g. glass or crystal membrane), liquid membrane (based on e.g. classical ion-exchanger) and special membranes (e.g. gas sensing or enzyme electrode). The electrodes utilized in this thesis –calcium ion selective electrode and pH-electrodes- are liquid membrane electrodes. Here, immiscible liquid (organic) phases with ion exchanger properties are used, which are stabilized against the sample solution utilizing a polymer or ceramic membrane. The main compound of the membrane is a neutral or charged carrier specific for the particular ion. The carrier is mobile inside the membrane in complexed as well as free configuration and facilitates a specific translocation of ions across the membrane.

Common pH-electrodes contain both the reference and the measurement electrode. Figure 3.4 schematically illustrates the configuration of pH-electrodes, which is best visualized as a tube in a tube. The inner tube is closed and forms the measurement electrode, whereas the outer tube forms the reference electrode (cp. Figure 3.2). Commercial ion selective electrodes usually require a second reference electrode. For calcium potential measurements of this thesis, the reference system of pH-electrodes is gripped.

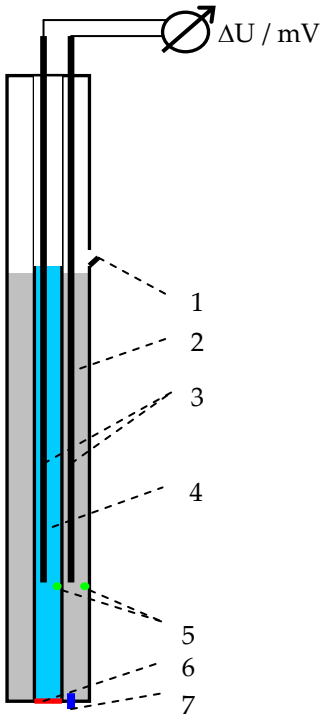

Figure 3.4: Scheme of pH-electrodes. 1: charging notch; 2: outer electrolyte; 3 M KCl; 3: silver wire; 4: inner electrolyte, 3 M KCl, phosphate buffer, pH = 7; 5: AgCl; 6: proton sensitive membrane; 7: diaphragm. The body of the electrode is made from non-conductive glass or plastics. For further explanations see text.

3.2.2 Titration

Titration is a volumetric technique, which is commonly used in quantitative chemical analytics in order to determine the concentration of a compound. The different main types of titration are acid-base titrations, red-ox titrations and complexometric titrations. This classification is based on the chemical reaction, which provides the quantitative analysis. In any case, a solution of known concentration (titrant) is used to react with a solution of the analyte of unknown concentration. The equivalence point of titration then gives the volume of the titrant necessary to neutralize the analyte. Knowledge of all volumes, of the titrant concentration and of the particular chemical reaction, which neutralizes the analyte, then facilitates the calculation of the unknown analyte concentration. Equivalence points are detected utilizing different kinds of indicators, which base on color change, precipitation, potential change, etc.

The titration applied in this thesis is an acid-base titration utilizing pH-electrodes (cp. section 3.2.1). However, acid-base titration is not used in order to determine an equivalence point but in order to maintain a constant pH-value. The chemical reaction analyzed,

$$(3.13) \qquad Ca^{2+}_{aq.} + HCO^{2-}_{aq.} \rightleftharpoons [CaCO_3]_{cluster_{aq.}/s} + H^{+}_{aq.},$$

causes a decreasing pH-value due to the removal of base and the generation of protons. The volume of base necessary in pH = constant titration can be converted into the bound amount of carbonate ions as discussed in detail in section 5.1.

3.3 Light Microscopy

Light microscopy uses visible light to magnify an image of small samples. The magnification is carried out by a system of optical lenses; the magnification -the resolution of details that are not visible with the naked eye- is based in principal on an objective lens with very short focal length, i.e. a highly magnifying lens. The short focal length requires a short distance to the specimen. Following lens systems are carefully aligned in order to further increase magnification and reduce optical aberrations. The optical microscope is limited in resolution by the properties of light and the utilized lens materials. The definite limit d_{LM} of optical resolution neglecting optical aberrations is given by ABBE's theory to

$$d_{LM} = \frac{\lambda_{LM}}{2A_N},$$

where $\lambda_{\Lambda M}$ is the wavelength of light and A_N is the numerical aperture of the optical system. The numerical aperture is given by $A_N = n_r \sin\theta_{LM}$ with refractive index n_r of the medium in which the lens is working and the half angle of the maximum cone of light that can enter or exit the lens θ_{LM}. Usually, a wavelength of 550 nm is assumed while the highest practical numerical aperture with air as medium is 0.95 (oil up to 1.5). This gives a limit of optical resolution of approximately 0.3 µm. Other, modern designs -e.g. Stimulated Emission Depletion Microscopy- can offer improved resolution for self-luminous particles because ABBE's limit is not applied.

Polarized light microscopy facilitates the detection of optical anisotropy of samples. An optical filter, which is permeable for light oscillating in a single plane, is placed in the optical

path previous to the sample. A second filter is placed in the optical path after the sample. If the filters are rotated by 90°, no light can be observed. If the analyzed sample is birefringent, the particular ray of light is decomposed into the ordinary and extraordinary ray. The polarization plane and phase velocity of the extraordinary ray are modified and the birefringent sample illuminates a dark background.

The light microscope employed in this thesis is a transmission light microscope Olympus BX41 which can be equipped with light polarizers.

3.4 Scanning Electron Microscopy

The scanning electron microscope (SEM) is a valuable tool for the analysis of surface structures. The imaging bases on a high energy beam of electrons, which is focused on the sample surface in high vacuum. The incident beam induces the generation of secondary electrons in the surface layer of the sample in a depth of $5-50$ nm depending on the analyzed material. The emitted type of signal detected can include secondary electrons, characteristic x-rays and back scattered electrons. Non-conductive samples are coated with a fine layer of conducting material in order to prevent the accumulation of static electric fields on the sample surface.

The sample is scanned point by point as a grid, while the image is generated by the particular yield of emitted signal, which increases on edges and with increasing decline of the surface. The signal is detected and displayed on a faceplate synchronically to the scanning electron beam, while the intensity correlates the height of the scanned point. The yield of signal is inversely proportional to the diameter of the incident electron beam, while the focussing of the beam is technically limited. Thus, depending on the instrument, the maximum resolution falls in between less than 1 nm and 20 nm.

The SEM utilized in this thesis is a LEO 1550-GEMINI. The samples are covered with gold.

3.5 Transmission Electron Microscopy

Transmission electron microscopes (TEM) operate in analogy to transmission light microscopes, while electrons instead of light are utilized for magnification. Electrons are accelerated in an electrical field and possess a wavelength according to DE BROGLIE wave particle dualism. The wavelength λ_{dB} can be calculated according to $\lambda_{dB} = \frac{h}{m_e v_e}$, where h is

the PLANCK constant, m_e is the electron mass and v_e is the electron velocity. The acceleration voltage adds up to between 80 kV and 400 kV and it is crucial to note that the resulting electron velocity is close to the speed of light. Thus, the electron velocity has to be calculated with a relativistic approach, while a reduced mass has to be considered for the calculation of the DE BROGLIE wavelength. The distinctly shorter wavelength of accelerated electrons than the wavelength of light provides a resolution in high-resolution TEM in the sub-ÅNGSTRÖM domain.

The principle path of electrons in TEM is similar to the optical path in light microscopy. Instead of optical lenses, electromagnetic fields carry out magnification. High vacuum provides a long free path length of electrons and facilitates a minimal expansion of the electron beam due to interactions with gas particles. Since the electron beam is to be transmitted through the sample, the sample has to be thin enough to allow electrons to permeate. Various interactions of the electron beam with the sample depending on density and chemistry are the basis of contrast that is visualized on an appropriate detector such as a fluorescent film or CCD camera.

The TEM utilized in this thesis is a Zeiss EM 912 Omega.

3.6 Wide Angle X-Ray Scattering and Electron Diffraction

Wide angle x-ray scattering (WAXS) and electron diffraction (ED) are both diffraction techniques giving information about the arrangement of atoms, ions or molecules, which are periodically aligned resulting in an atomic lattice. Diffraction occurs if the spacing between the planes in the atomic lattice is in the order of magnitude of the wavelength of the radiation applied. Common WAXS instruments utilize the copper K-alpha x-ray with a wavelength of 0.154 nm, while ED is performed in TEM with similar wavelengths depending on the acceleration voltage (cp. section 3.5). In contrast to common WAXS, which mostly gives the average scattering of a powder, ED has the advantage of giving locally resolved diffraction patterns, which is important for the analysis of inhomogeneous samples.

The physical basis of the generation of WAXS spectra and ED diffraction patterns is the BRAGG equation

$$2 \cdot d \cdot \sin\theta = n \cdot \lambda ,$$

with $n = 0, 1, 2, \ldots$, the wavelength of the applied radiation λ, spacing between the lattice planes d and angle θ as illustrated in Figure 3.5.

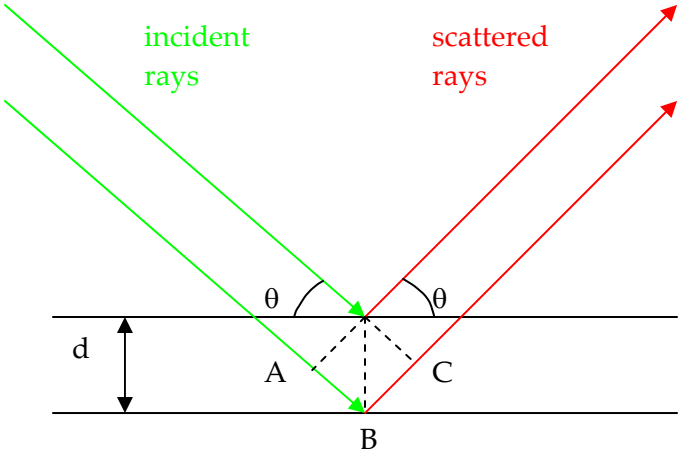

Figure 3.5: Scheme clarifying the BRAGG equation. For explanations see text.

Due to constructive and destructive interference, the intensity of scattering changes in dependence of the angle θ. Constructive interference of scattered radiation exhibits a maximum if the phase shift of two rays is a multiple of the wavelength. Since the additional distance for the lower ray in Figure 3.5 is $ABC = 2 \cdot d \cdot \sin\theta$, the BRAGG equation gives the condition for constructive interference.

In WAXS measurements, the scattered beam is detected angle-dependent, while the scattering intensity exhibits maxima at angles complying with the BRAGG equation, while ED measurements give a two-dimensional diffraction pattern showing rings (polycrystalline sample) or spots (single crystalline sample).

4 Experimental

All experiments are performed at 24 ± 1 °C.

4.1 Preparation of Solutions

All solutions are prepared using Millipore water that is purged with nitrogen overnight in order to remove residual carbon dioxide. Calcium chloride solutions for calcium ion sensitive electrode calibration of double diffusion experiments are prepared from 0.100 M standard solution (Metrohm, No. 6.2301.070) by stepwise 1:10 dilution.

The 10 mM sodium hydroxide solution used in pH = constant titrations is prepared by 1:100 dilution of 1 M standard solution (Riedel-de Haën, No. 33256), 10 mM hydrochloric acid solution for pH = constant titration is prepared analogously from 1 M standard solution (Riedel-de Haën, No. 35328).

The 10 mM calcium chloride solution for diffusion experiments, beaker experiments and gas diffusion experiments is prepared using calcium chloride dihydrate (Fluka, Ultra ≥ 99.5 %, No. 21098). The 10 mM carbonate buffers are prepared from mixtures of 10 mM sodium carbonate (Sigma, 99.95 – 100.05 %, No. 223484) and 10 mM sodium bicarbonate (Acros Organics, ACS grade, No. 424270010) solutions giving the desired pH-value.

Polyacrylic acid (molecular weight 5,100 g/mol, Fluka, No. 81132) is utilized without further purification. Peptide additives are prepared according to section 4.4.

Polyacrylic acid is directly weighed into carbonate buffer for additive experiments. Peptide additives are prepared in a concentrated stock solution, which pH-value is set to the pH-value of the carbonate buffer and subsequently added to the particular carbonate buffer while volume dilution is negligible (approx. $1/100 = V_{stock}/V_{buffer}$).

4.2 Calcium Measurements and Crystallization at Constant pH-Values

4.2.1 Principal Setup

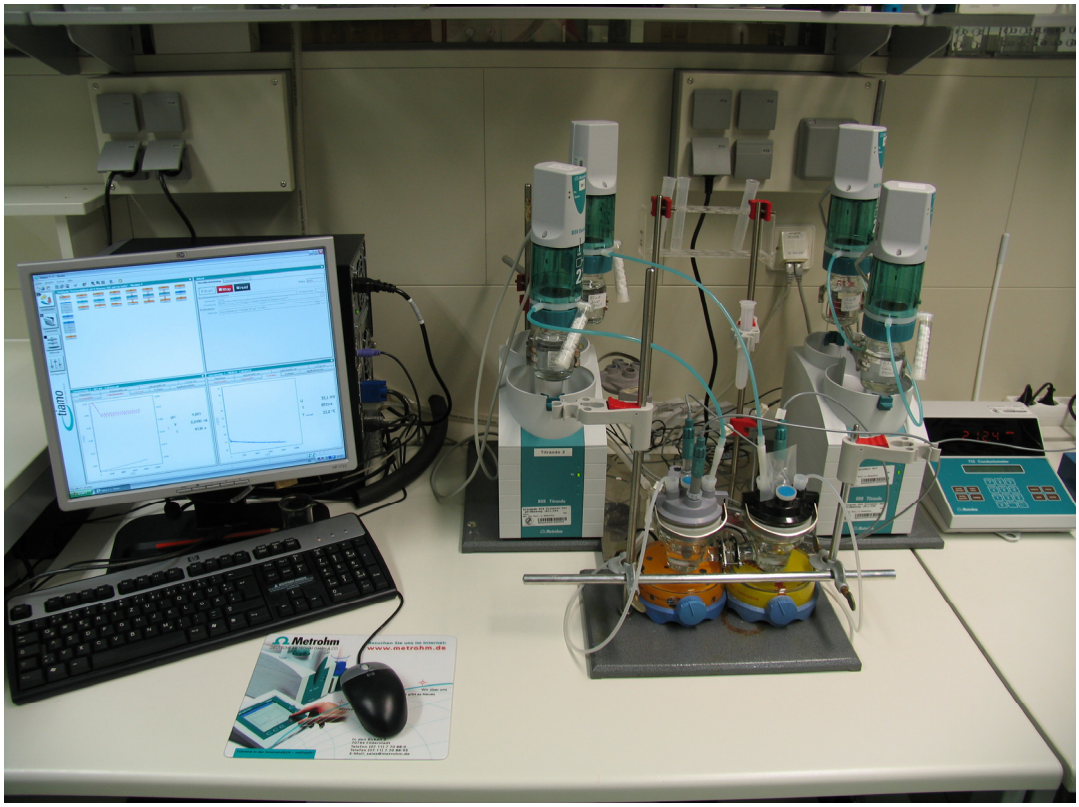

Figure 4.1: The utilized Metrohm setup during a double diffusion experiment.

The setup is a commercial, computer controlled titration system manufactured by Metrohm[1]. The titration software is tiamo 1.1. The setup consists of two titration devices Titrando 809 controlling four dosing devices 800 Dosino that operate a 807 Dosing Unit, respectively. The 807 Dosing Unit incorporates a 2 mL glass cylinder, whose depletion is divided into 10,000 steps resulting in a minimal dose-able volume of 0.2 µL. Two pH-electrodes (No. 6.0227.100 and No. 6.0256.100) and one calcium ion sensitive electrode (No. 6.0508.110) are utilized. For calcium potential measurements the reference system of pH-electrodes is gripped.

[1] www.metrohm.com

4.2.2 Calibration of Electrodes

The pH-electrodes are calibrated weekly utilizing pH = 4.0, pH = 7.0 and pH = 9.0 Metrohm buffers (No. 6.2307.100, No. 6.2307.110, No. 6.2307.120). A weekly calibration is sufficient because electrode slope and electrode intercept turned out to be highly reproducible.

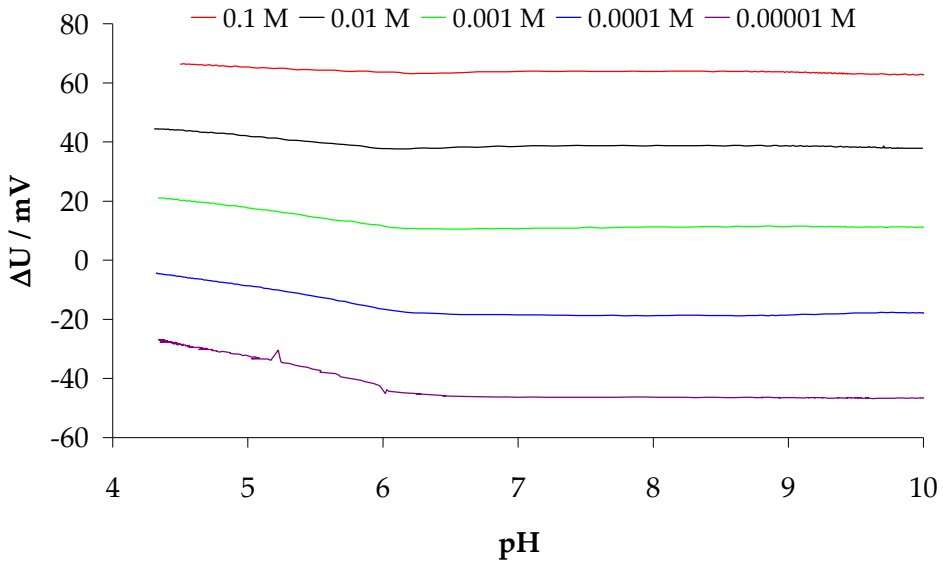

Figure 4.2: Calcium potential as measured with the utilized calcium ion selective electrode. The potential is nearly pH-independent above pH = 7.0. The ideal electrode slope of approximately 28 mV per order of magnitude in calcium concentration is maintained up to concentrations of 0.1 M. Since the pH was changed by addition of dilute NaOH, an interfering influence of Na^+ can be excluded.

The calcium ion selective electrode has to be calibrated at the particular pH-value before every experiment because electrode slope and intercept differ between most experiments and turned out to be pH-dependent (cp. Figure 4.2). Here, the pH-value is titrated constant by 10 mM sodium hydroxide solution and 10 mM hydrochloric acid in order to achieve high pH-constancy. The volume dilution necessary due to pH = constant titration is considered. It is crucial to perform the calibration under nitrogen atmosphere, because in-diffusion of carbon dioxide causes cluster formation and thus binding of calcium ions. The nitrogen atmosphere is provided by a nitrogen shower, which is designed by pipelining nitrogen from a gas container through a wash bottle filled with water in order to roughly saturate the nitrogen gas with water and prevent showered solutions from drying. The nitrogen gas is then directed onto the solution's surface, whereas the beaker is sealed against the air atmosphere with Parafilm in order to give the nitrogen gas a minimum sized outlet.

In double diffusion experiments, the calcium ion sensitive electrode is calibrated using $1 \cdot 10^{-3}$ M and $1 \cdot 10^{-4}$ M calcium standards (2-point calibration).

In beaker experiments, the calcium ion sensitive electrode is calibrated by addition of the dilute calcium chloride solution particularly used in the following experiment into nitrogen saturated Millipore water. Here, the advantage is to perform calibration in almost the same environment (immersion depth, volume, stirring rate, etc.) as in the following experiment. Moreover, around 50 points can be fitted.

4.2.3 Double Diffusion Experiments

The counter diffusion experiments are performed in a custom made diffusion cell according to Figure 4.3. Two compartments are connected via a dialysis membrane (Spectra/Por, Cellulose Ester, molecular weight cut-off 100,000 g/mol, No. 131417) to prevent uncontrolled mixing of solutions. The surface of the membrane is approx. 1.74 cm^2. The calcium compartment contains 25 mL 10 mM calcium chloride solution and the other compartment contains 25 mL water or 10 mM carbonate buffer. Both compartments are kept at constant pH-value *via* titration of 10 mM sodium hydroxide solution as the pH-value tends to decrease with time as discussed in section 5.1.

Before the addition of solutions to the double diffusion cell illustrated in Figure 4.3, the pH-value is pre-set in a beaker (50 mL) under nitrogen atmosphere (cp. section 4.2.2) except for carbonate buffers, which pH-values were adjusted by the variation of the amounts of carbonate and bicarbonate ions (cp. section 4.1). The in-diffusion of calcium ions is monitored in the water and carbonate buffer compartment, respectively, *via* a calcium ion selective electrode. The experiments of the calcium/water diffusion system are performed under nitrogen atmosphere applying a nitrogen shower as described in section 4.2.2 in both compartments. The experiments of the calcium/carbonate buffer diffusion system are performed in nitrogen atmosphere in the calcium compartment only, since the nitrogen shower removes carbon dioxide from the carbonate buffer equilibrium system influencing pH = constant titration. Electrodes, diffusion cell and burette tips are cleaned with 10% acetic acid and carefully rinsed with distilled water after every experiment.

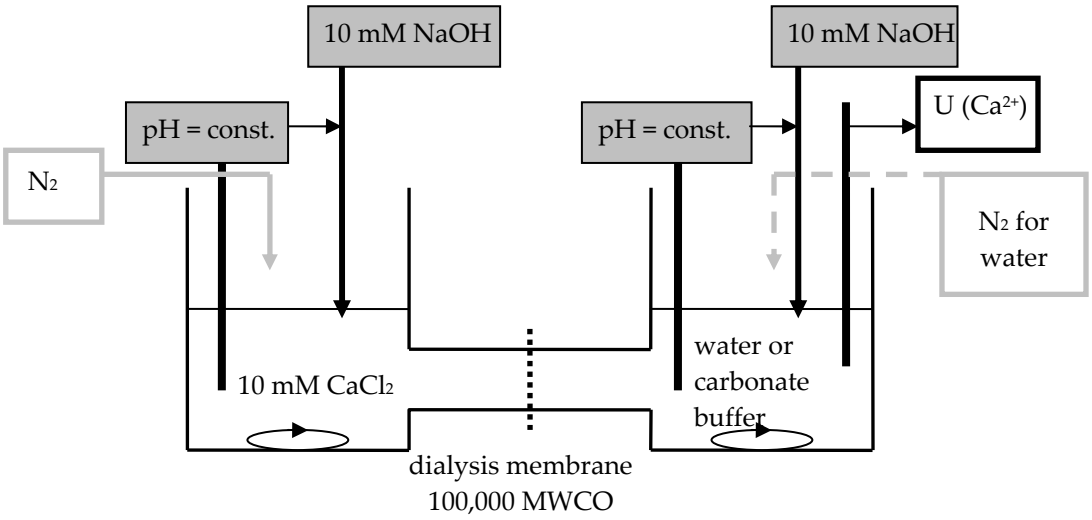

Figure 4.3: Scheme of the custom made diffusion cell with solutions and electrodes. For further explanations see text.

4.2.4 Beaker Experiments

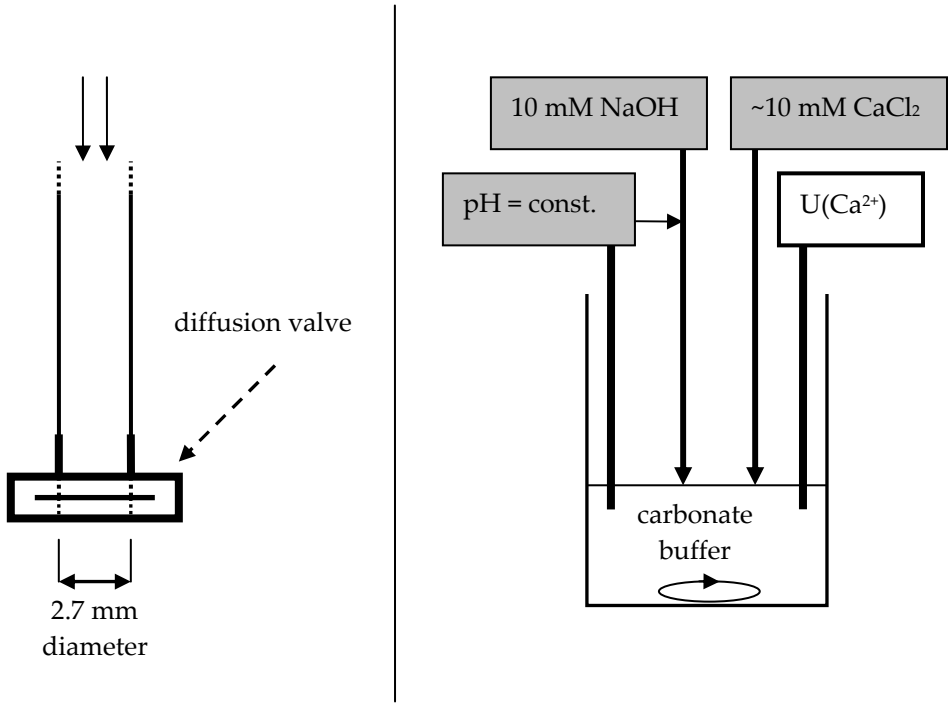

Figure 4.4: Left: Scheme of Metrohm® burette tips. The outlet has a diameter of 2.7 mm and is equipped with a diffusion valve that opens only if solution is dosed avoiding out-diffusion of dosed solutions. Right: Scheme of beaker experiments. For further explanations see text.

4.2.4.1 Crystallization Experiments

The beaker experiments are performed in a 50 mL beaker filled with 25 mL of 10 mM carbonate buffer (with or without the particular additive) of the particular pH-value according to Figure 4.4. All solutions are prepared according to section 4.1. 10 mM dilute calcium chloride solution set to the particular pH-value (volume dilution due to pH-adjustment is considered) is dosed at a rate of 10 µL per minute. The pH-value is kept constant *via* pH = constant titration with 10 mM sodium hydroxide solution and the calcium potential is monitored. Electrodes, beaker and burette tips are cleaned with 10% acetic acid and carefully rinsed with distilled water after every experiment.

4.2.4.2 Calcium Titration

Calcium titration is performed in analogy to the crystallization experiments, while the pH-value is titrated constant by alternating titration with 10 mM sodium hydroxide solution and 10 mM hydrochloric acid. 0.1 M calcium chloride solution (Metrohm standard) is dosed at a rate of 10 µL/minute into 25 mL 0.1 g/L polyacrylic acid solution in pure water while the calcium potential is monitored.

4.2.5 Yield of Crystals

Crystals are sedimented in earth's gravity field and the supernatant is transfused or pipetted off. The crystals are subsequently repeatedly washed with acetone and dried.

4.3 Crystallization Experiments at Shifting pH-Values -Gasdiffusion Experiments

Gasdiffusion experiments are a common method for the precipitation of calcium carbonate working through in-diffusion of carbon dioxide and ammonia into calcium chloride solution. The common starting pH-value of such experiments is in the range of pH = 5-6 and precipitation takes place at pH = 8.5-9.

5 mL of 10 mM calcium chloride solution (with or without additive) are filled into a 20 mL disposable glass, which is covered by Parafilm furnished with three pinholes. The glass is placed together with a disposable glass containing 2 g ammonium carbonate (also covered with Parafilm furnished with three pinholes) in a dessicator.

The results of gasdiffusion experiments are very sensitive to volumes, number of applied pinholes, position in the exsiccator, etc. Thus, it is important not to change details of the experimental setup in order to facilitate comparable experiments [48].

Cover slips are put on the bottom of glasses in order to increase the yield of precipitated crystals.

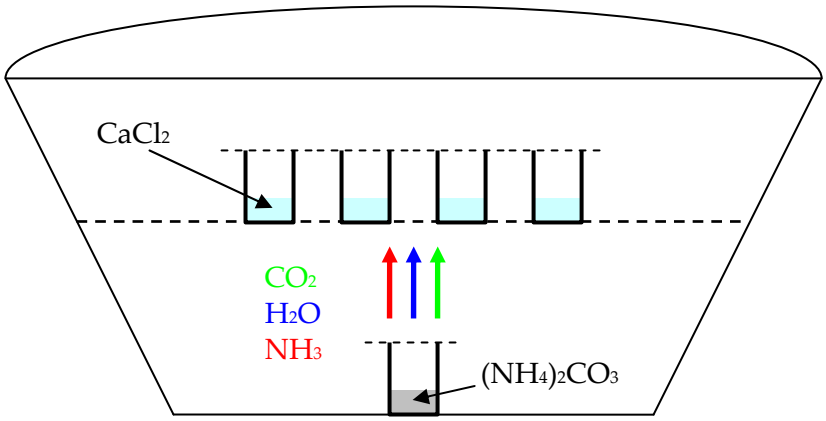

Figure 4.5: Scheme of gasdiffusion experiments. Glasses containing 5 mL 10 mM calcium chloride solution and a glas containing 2 g ammonium carbonate are placed in a closed dessicator. Decomposition of ammonium carbonate at room temperature forms carbon dioxide, water and ammonia. The in-diffusion of carbon dioxide and ammonia into the calcium chloride solution facilitates precipitation of $CaCO_3$.

4.4 Synthesis of Peptide Additives

4.4.1 Materials

Diisopropylethylamine (DIPEA; Acros, peptide grade), piperidine (Acros, peptide grade), trifluoracetic acid (TFA; Acros, peptide grade), have been applied as received. Fmoc-amino acid derivatives, N-methyl-2-pyrrolidone (NMP, 99.9+%, peptide synthesis grade) and 2-(1H-benzotriazole-1-yl)-1,1,3,3-tetramethyluronium hexafluorophosphate (HBTU) were used as received from IRIS Biotech GmbH, Germany. 1,3-dicyclohexylcarbodiimide (DCC, 1 M in NMP), diethyether and triethylsilane have been applied as received from Aldrich. Dichloromethane (DCM; IRIS Biotech GmbH, peptide grade) was distilled from CaH_2. Wang Resin was purchased from Rapp, Polymere GmbH, Tübingen, Germany.

4.4.2 Synthesis

The loading of the Wang resin (0.24 mmol/g; 0.1 mmol scale) was performed using standard solid-phase supported peptide synthesis protocols applying DCC/DIPEA/NMP chemistry [49, 50]. The resin was loaded on an Applied Biosystems ABI 433a peptide synthesizer. Oligopeptide synthesis was performed in NMP as solvent following standard ABI-Fastmoc double coupling protocols. Amino acid coupling was facilitated using HBTU/DIPEA. The liberation of the different peptides was accomplished by 2 h treatment with the cleavage mixture [95% TFA, 1% triethylsilane, 4% H_2O], followed by two washing cycles with DCM. The oligopeptide was isolated by diethyl ether precipitation, centrifugation and ultrafiltration (MWCO ≈ 1000 g/mol) followed by lyophilization from water.

5 Results and Discussion

5.1 Calcium Carbonate Precipitation and pH-Value

It is important to note that binding of carbonate ions –in cluster formation as well as precipitation of calcium carbonate- causes a decrease of the pH-value that again changes the ratio of carbonate species, carbon dioxide, carbonic acid, bicarbonate and carbonate, in the carbonate buffer equilibrium. The decrease of the pH-value is due to the removal of carbonate ions from the buffer equilibrium. A constant pH-value maintains a constant ratio of carbonate species, which is essential for quantitatively analyzable experiments, and is ensured by pH = constant titration. This section quantifies the distribution of carbonate species in a carbonate buffer as a function of pH-values and total concentration of carbonate species in order to facilitate the calculation of the bound amount of carbonate ions from the volume of dilute base necessary in pH = constant titration.

The equilibrium system of a carbonate buffer can be written as

$$\begin{aligned} &CO_{2,aq.} + H_2O \rightleftharpoons \\ &H_2CO_{3,aq.} \rightleftharpoons H^+_{aq.} + HCO^-_{3,aq.} \rightleftharpoons 2H^+_{aq.} + CO^{2-}_{3,aq.} \end{aligned} \quad . \tag{5.1}$$

The concentration of carbonic acid is very low, so the first step of the equilibrium system can hardly be characterized experimentally. Therefore, it is widely accepted to combine the first step of equilibrium (5.1) giving

$$\begin{aligned} &\left\{CO_{2,aq.} + H_2O \leftrightarrow \left[H_2CO_{3,aq.}\right]\right\} \\ &\xrightleftharpoons{K_1} H^+_{aq.} + HCO^-_{3,aq.} \xrightleftharpoons{K_2} 2 \cdot H^+_{aq.} + CO^{2-}_{3,aq.} \end{aligned} \quad , \tag{5.2}$$

$$\text{with } c\left(\left[H_2CO_{3,aq.}\right]\right) \cong c\left(CO_{2,aq.}\right).$$

The acid constants are given by $pK_1 = 6.35$ and $pK_2 = 10.33$ [51]. Assuming ideality for ionic strengths smaller than 0.1, the law of mass action and the principle of mass preservation give the concentrations of carbonate species depending on the total carbonate concentration $c_{total}(\text{carbonate})$ and $pH = -\log\left[c(H^+)\right]$ to

$$c(\left[CO_{2,aq} \right]) = c_{total}(carbonate)\left[\frac{K_1}{c(H^+)} + \frac{K_1 K_2}{c(H^+)^2} + 1 \right]^{-1}, \quad (5.3)$$

$$c(HCO_{3,aq.}^-) = c_{total}(carbonate)\underbrace{\left[\frac{c(H^+)}{K_1} + \frac{K_2}{c(H^+)} + 1 \right]^{-1}}_{\Lambda\left(HCO_{3,aq}^-\right)_{pH}} \quad (5.4)$$

and

$$c(CO_{3,aq.}^{2-}) = c_{total}(carbonate)\underbrace{\left[\frac{c(H^+)^2}{K_1 K_2} + \frac{c(H^+)}{K_2} + 1 \right]^{-1}}_{\Lambda\left(CO_{3,aq.}^{2-}\right)_{pH}}. \quad (5.5)$$

Equations (5.3), (5.4) and (5.5) give a constant ratio of the three considered carbonate species for any constant pH-value as illustrated in Figure 5.1. The pH-development of the fraction of the three carbonate species is the background of the pH-range, in which calcium carbonate can exist and in which calcium carbonate can be precipitated. At pH-values lower than approximately pH = 5, the excess species is carbon dioxide and calcium carbonate dissolves. From approximately pH = 7 on, the fraction of carbonate ions is sufficiently high to facilitate precipitation. The crystallization range fades at high pH-values, because concurrent crystallization of calcium hydroxide occurs.

Removal of a carbonate ion due to cluster formation or precipitation complies with the removal of a diprotic base, which has to be exchanged by the titration of two OH^- ions in order to keep the pH-value constant. Simultaneously, removal of one single carbonate ion from the buffer equilibrium (5.2) changes the ratio of the three considered carbonate species. Because the pH-value is kept constant, the equilibrium readjusts to the ratio corresponding to the particular pH-value kept constant. Bicarbonate is the excess species at the investigated pH-values and the equilibrium readjustment generates protons.

The amount of protons generated per removed carbonate ion can be calculated from equations (5.4) and (5.5): $\Lambda(HCO_{3,aq.}^-)_{pH}$ and $\Lambda(CO_{3,aq.}^{2-})_{pH}$ are the percentages of the particular ions at a constant pH-value. After the removal of one carbonate ion, the ratio of the percentages maintains constancy due to the readjustment of equilibrium (5.2), i.e. a

fractional number of bicarbonate ions transforms into a fractional number of carbonate ions generating a fractional number of protons.

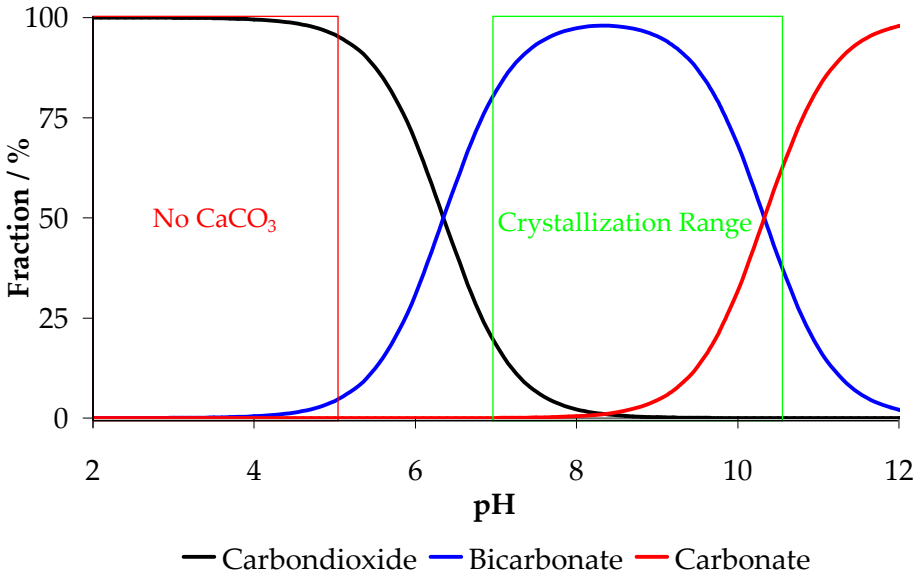

Figure 5.1: Distribution of the different carbonate species in dependence of the pH-value as given by equations (5.3), (5.4) and (5.5).

$\lambda(HCO_{3,aq.}^-)_{pH}$ is the fractional number of bicarbonate ions transformed if a single carbonate ion is removed from the equilibrium and $\lambda(CO_{3,aq.}^{2-})_{pH}$ is the fractional number of carbonate ions generated if a single carbonate ion is removed from the equilibrium then giving

$$\frac{\Lambda(CO_{3,aq.}^{2-})_{pH}}{\Lambda(HCO_{3,aq.}^-)}_{pH} = \text{const.} = \frac{\Lambda(CO_{3,aq.}^{2-})_{pH} - \lambda(CO_{3,aq.}^{2-})_{pH}}{\Lambda(HCO_{3,aq.}^-)_{pH} - \lambda(HCO_{3,aq.}^-)_{pH}}. \tag{5.6}$$

The generation of protons due to deprotonation of carbonic acid (i.e. carbon dioxide, cp. equation (5.2)), is neglected in this regard because the percentage of carbon dioxide decreases fast at the investigated pH-values (approx. 1% at pH = 8.3 and 0.01% at pH = 10.0). Rearrangement of equation (5.6) gives with $\lambda(CO_{3,aq.}^{2-})_{pH} + \lambda(HCO_{3,aq.}^-)_{pH} = 1$ the fractional number of carbonate ions and bicarbonate ions that readjust the equilibrium if a carbonate ion is removed and the pH-value is kept constant

$$\lambda(CO_{3,aq.}^{2-})_{pH} = \frac{\Lambda\left(CO_{3,aq.}^{2-}\right)_{pH}}{\Lambda\left(CO_{3,aq.}^{2-}\right)_{pH} + \Lambda\left(HCO_{3,aq.}^-\right)_{pH}}, \tag{5.7}$$

$$\lambda(HCO_{3,aq.}^{2-})_{pH} = \left[1 + \frac{\Lambda\left(CO_{3,aq.}^{2-}\right)_{pH}}{\Lambda\left(HCO_{3,aq.}^{-}\right)_{pH}}\right]^{-1} . \qquad (5.8)$$

Comparison of equation (5.8) and equilibrium (5.2) shows that the fractional number of bicarbonate ions gives the number of H^+ generated by the buffer equilibrium, and the fractional number of carbonate ions gives the actual number of diprotic base removed if a single carbonate ion is removed from the buffer equilibrium and the pH-value is kept constant.

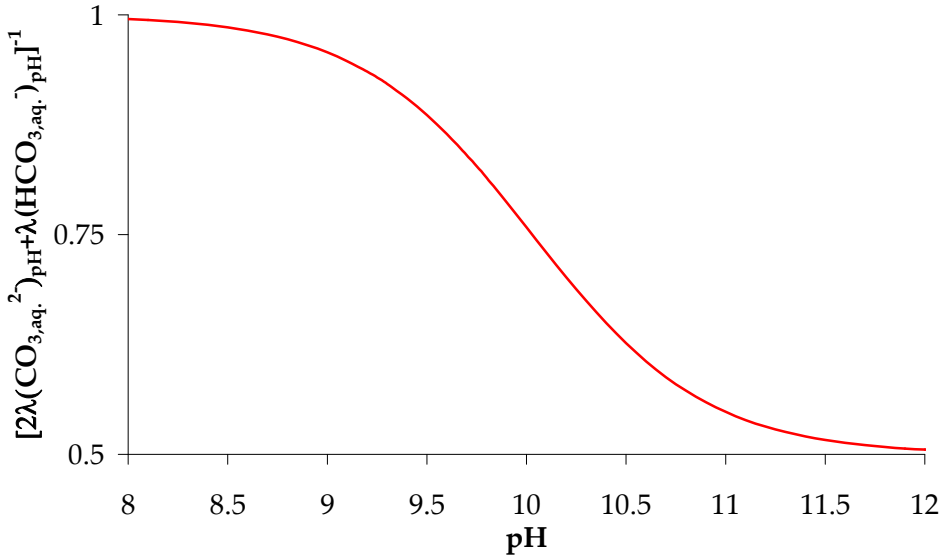

Figure 5.2: The pH-development of $\left[2 \cdot \lambda\left(CO_{3,aq.}^{2-}\right)_{pH} + \lambda\left(HCO_{3,aq.}^{-}\right)_{pH}\right]^{-1}$, cp. equation (5.9). For explanations see text.

Thus, for each carbonate ion removed from the equilibrium,

$$\left[2 \cdot \lambda\left(CO_{3,aq.}^{2-}\right)_{pH} + \lambda\left(HCO_{3,aq.}^{-}\right)_{pH}\right] \ OH^- \text{ ions}$$

have to be titrated in order to keep the pH-value constant, and the amount of carbonate ions bound in clusters and particles can be calculated by pH = constant titration with

$$n_{bound}(CO_3^{2-}) \cong c(NaOH) \cdot V(NaOH) \cdot \frac{1}{2 \cdot \lambda(CO_{3,aq.}^{2-})_{pH} + \lambda(HCO_{3,aq.}^{-})_{pH}} . \qquad (5.9)$$

The pH-development of $\left[2\cdot\lambda\left(CO_{3,aq.}^{2-}\right)_{pH}+\lambda\left(HCO_{3,aq.}^{-}\right)_{pH}\right]^{-1}$ is illustrated in Figure 5.2. It is obvious that a higher volume of NaOH is necessary in pH = constant titration at higher pH-values compared to lower pH-values.

5.2 Calcium Carbonate Precipitation in Absence of Additives

Calcium carbonate precipitation in absence of additives is studied at constant pH-values by a series of critical experiments. Growing supersaturation is established by slow addition of calcium ions into carbonate buffer. The addition of calcium ions is performed in two different experimental setups, respectively, in double diffusion experiments and beaker experiments. In double diffusion experiments (cp. section 4.2.3), a calcium chloride compartment and a carbonate buffer compartment are separated by a dialysis membrane in order to avoid mixing of solution. The dialysis membrane facilitates the diffusion of calcium ions into the carbonate buffer and *vice versa*. In beaker experiments (cp. section 4.2.4), calcium ions are added by slow dosing of calcium solution into carbonate buffer at a rate of 10 µL/min. In the following, both types of experiments are discussed in detail, double diffusion experiments in section 5.2.1 and beaker experiments in section 5.2.2. The results of both experimental setups are compared in section 5.2.3 showing that the different setups give the same results within experimental accuracy, while beaker experiments provide a better resolution. Thus, in following sections, which provide the physicochemical characterization of calcium carbonate precipitation, only beaker experiments are discussed.

5.2.1 Double Diffusion Experiments

The experiments performed in the calcium/water diffusion system (cp. section 4.2.3) are the reference experiments giving the flux of calcium ions from the calcium compartment across the membrane. This flux can be analyzed according to FICK's law. The calcium compartment (index I) and the water compartment (index II) are rigorously stirred and it can be assumed that the gradient of concentration is only maintained across the membrane. The combination of the corresponding transport equations simplifying for a steady state flux gives

$$(5.10)\qquad \begin{aligned} V_I \frac{dc_I(Ca^{2+})}{dt} &= -PA\frac{\Delta c(Ca^{2+})}{d_D} \\ V_{II} \frac{dc_{II}(Ca^{2+})}{dt} &= PA\frac{\Delta c(Ca^{2+})}{d_D} \end{aligned},$$

with volume V, molar concentration c, time t, permeability P, area of the membrane A, gradient of concentration Δc, thickness of the membrane d_D. Rearrangement, combination and integration of (5.10) with appropriate initial condition $\Delta c\left(Ca^{2+}, t=0\right)$ as starting gradient of concentration gives the diffusion parameter Ψ,

$$(5.11)\qquad \Psi = \frac{\ln\left[\frac{\Delta c(Ca^{2+},t)}{\Delta c(Ca^{2+},t=0)}\right]}{\left(\frac{A}{d_D}\left(\frac{1}{V_I(t)}+\frac{1}{V_{II}(t)}\right)\right)} = -Pt\,.$$

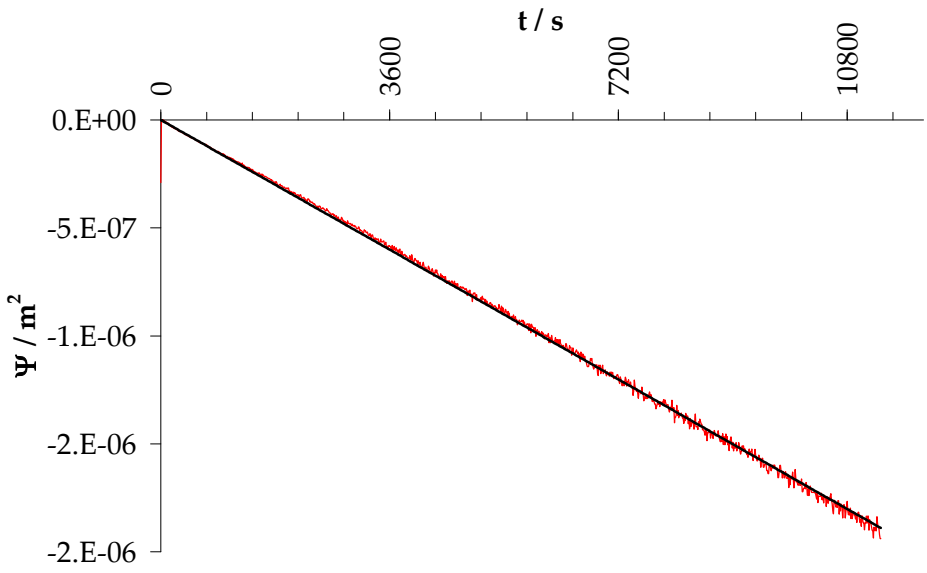

Figure 5.3: Diffusion analysis of a single data set at pH = const. = 9.50 gives a permeability of approx. $1.7 \cdot 10^{-10}$ m² s⁻¹. The flux of calcium ions across the membrane can be considered as steady state flux within the investigated time. Red line gives the measured time development and the black line gives the linear regression yielding the permeability, cp. equation (5.11). For further explanations see text.

The compartment volumes are treated as a function of time here, since the pH-value is kept constant by alternating titration with dilute sodium hydroxide solution and dilute hydrochloric acid (cp. section 4.2.3). Analysis of a single data set at pH = const. = 9.50 according to equation (5.11) is shown in Figure 5.3 giving a permeability of approx.

$1.7 \cdot 10^{-10}$ m^2 s^{-1}. Multiple repetition of the experiment shows that the permeability of the utilized dialysis membrane is fluctuating for different cuts as illustrated in Figure 5.4. The time-development of the in-diffused amount of free calcium ions shows that the permeability is pH-independent within the resolution of the experiments as indicated by the emphasized time-developments at pH = 9.2 and pH = 10.0.

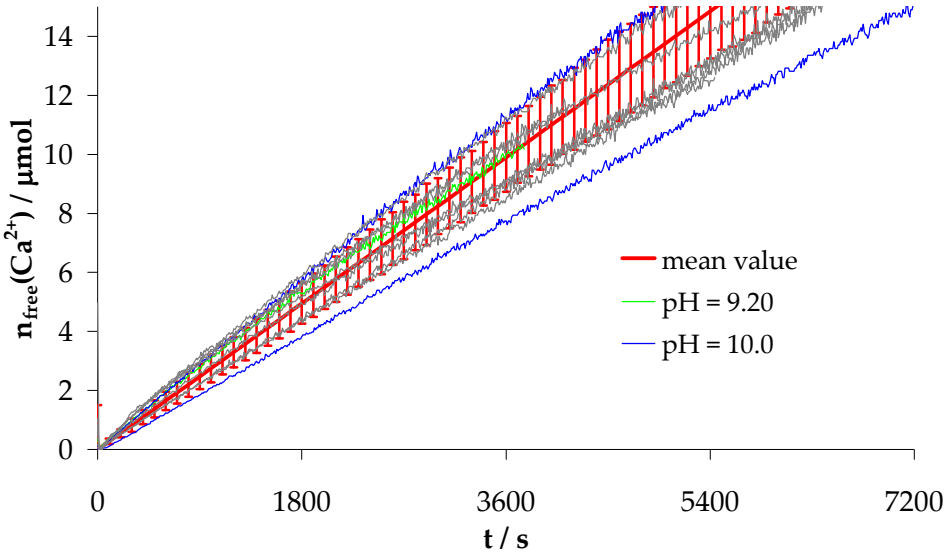

Figure 5.4: Fluctuation of the permeability of the utilized dialysis membrane illustrated by the in-diffused amount of free calcium ions. The permeability is pH-independent within the experiments' resolution as obvious from the emphasized time developments at pH = 9.2 and pH = 10.0. The red line gives the mean value of the slope of initial time-developments and error bars depict the standard deviation of 10 experiments shown.

The red line gives the mean value of initial slopes and error bars depict the standard deviation of 10 measurements at different pH-values. A linear regression of initial slopes is justified due to the steady state flux of calcium ions as demonstrated in Figure 5.3. Replacing water by carbonate buffer, one can expect equal steady state flux of calcium ions due to the same concentration gradients and very similar viscosities of water and the utilized dilute carbonate buffer[2]. However, the in-flux of calcium is ostensibly reduced as illustrated by single experiments illustrated in Figure 5.5. The reference time-development shown is introduced in Figure 5.4. With increasing pH-values, i.e. an increasing fraction of carbonate

[2] 20 °C: η_{water} = 1.0020 cP, η_{buffer} = 1.0039 cP; calculated with the program SEDNTERP, http://www.jphilo.mailway.com/download.htm

ions in the buffer equilibrium (cp. section 5.1), the initial time development of the free calcium ions gets flattened. This means that a considerable amount of free calcium ions is removed from solution.

When a sufficiently high supersaturation is maintained, calcium carbonate nucleates and the amount of free calcium ions drops to a value that corresponds to the solubility concentration of the particular phase formed. This phase is ACC as indicated by polarized light microscopy (cp. Figure 5.6).

The time developments as shown for single experiments in Figure 5.5 again exhibit fluctuations ascribed to permeability fluctuations in analogy to the reference experiments in the calcium/water diffusion system. The fluctuations are exemplary illustrated for the measurements at pH = 9.00 in Figure 5.7.

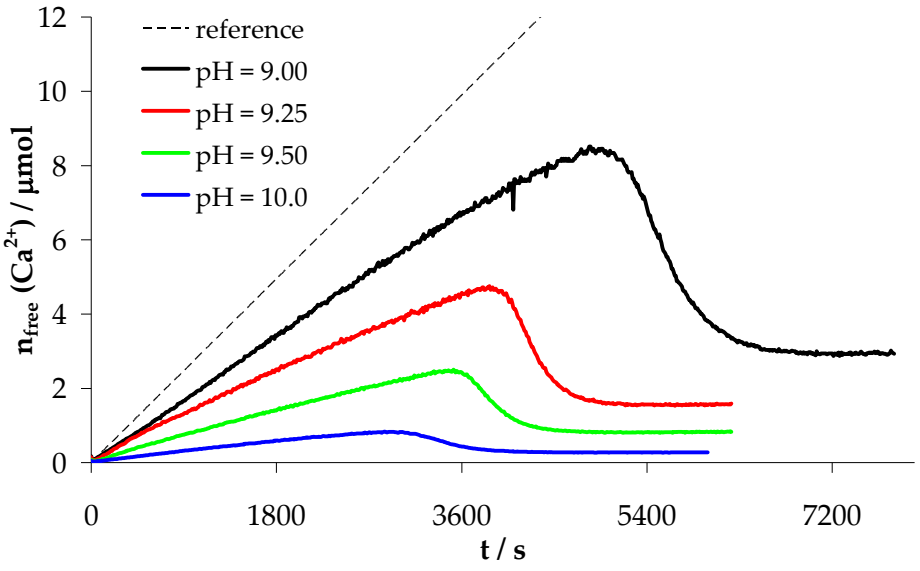

Figure 5.5: Time development of the free amount of calcium ions in the calcium/carbonate buffer diffusion system compared to the calcium/water diffusion system (reference). The time development decreases with increasing pH-values, i.e. calcium carbonate clusters are formed. After nucleation of ACC the free amount of calcium ions drops to a constant value corresponding to the particular solubility concentration.

Again, the mean value of the initial increase is derived from the mean value of the initial slopes and indicated as mean value b.n. The mean value after nucleation is derived from the mean value of the particular constant amounts of calcium and indicated as mean value a.n. The particular standard deviations are determined, respectively. This kind of averaging is

performed analogously with a sample of five single measurements for pH = 9.00, pH = 9.25, pH = 9.50 and pH = 10.0, respectively.

As already indicated, the flattened increase of the free amount of calcium ions can be attributed to the formation of calcium carbonate clusters. This is obvious from a flattened slope of the particular time-developments, while the time-development gets flatter with increasing pH-values, i.e. an increasing fraction of carbonate in the buffer equilibrium. Thus, the difference between the reference time-development of the free amount of calcium in the calcium/water diffusion system and the particular time-developments in the calcium/carbonate buffer diffusion systems gives the bound amount of calcium in calcium carbonate clusters before nucleation and bound in the new phase after nucleation.

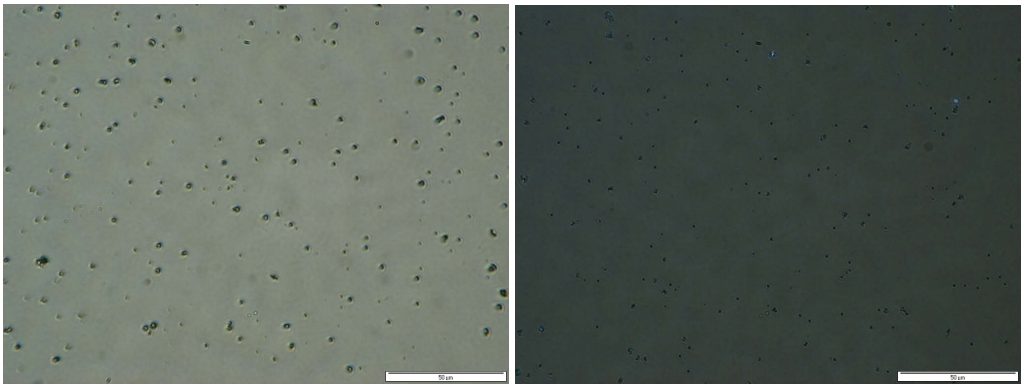

Figure 5.6: Polarized light optical microscopy images of calcium carbonate particles collected 30 minutes after nucleation at pH = 9.00 with parallel polarizers (left) and crossed polarizers (right). The image with crossed polarizers illustrates that the nucleated particles are amorphous and only few particles already become crystalline as indicated by bright spots. Scale bar 50 microns.

The difference is calculated from the mean value of the reference experiment and the particular mean values of the experiments at different pH-values and gives the bound amount of calcium ions. The time developments of bound amounts of calcium ions are illustrated in Figure 5.8 whereas the time of nucleation is averaged from the sample of five measurements, respectively. Error bars depict the particular standard deviations. The time developments reflect the cluster formation and nucleation of the new phase in analogy to Figure 5.5 but for bound amounts of calcium. Calcium binding is more distinct at higher pH-values and can be attributed to a higher fraction of carbonate ions in the buffer equilibrium. This regard is visible in calcium binding before nucleation and after nucleation.

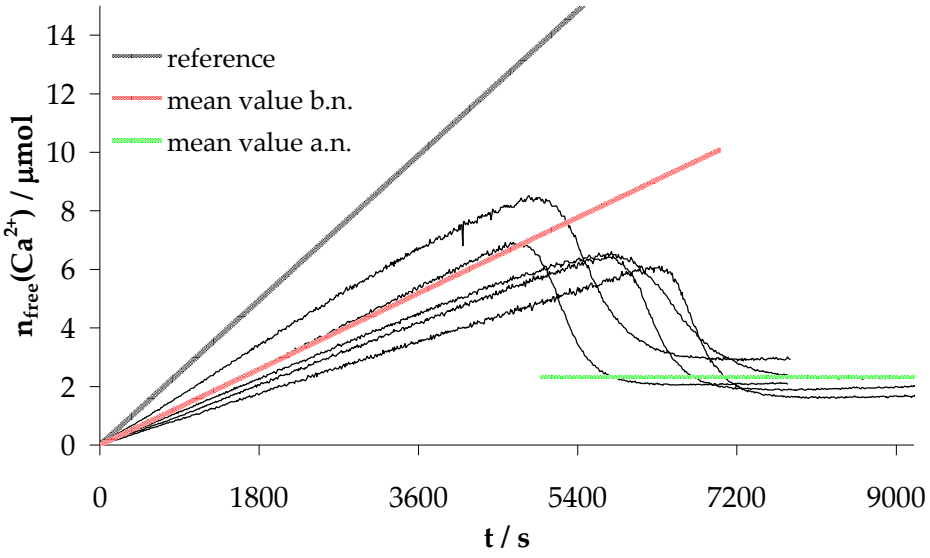

Figure 5.7: Illustration of the averaging of a sample of five measurements in the calcium/carbonate buffer diffusion system at pH = 9.00. For further explanations see text.

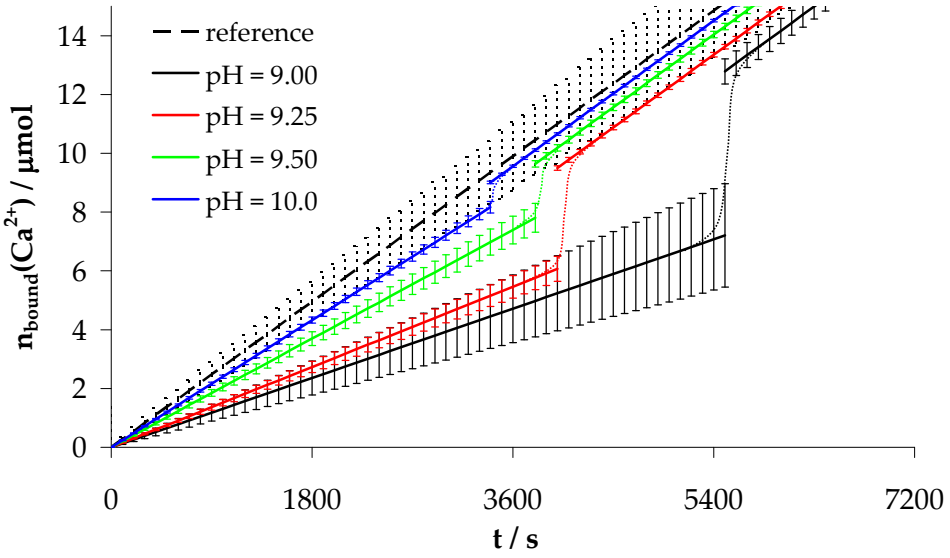

Figure 5.8: Time development of the bound amounts of calcium ions. The bound amount increases suddenly at the time of nucleation and merges a value corresponding to the particular solubility concentration of the formed ACC phase. Calcium binding is more distinct at higher pH-values before and after nucleation due to a higher fraction of carbonate ions in the buffer equilibrium. For further explanations see text.

The cluster formation is apparent in pH = constant titration, too, because the pH-value has to be titrated constant from the beginning of the experiment, i.e. carbonate ions are removed from the buffer equilibrium. The time-development of the necessary volume of 10 mM

NaOH in pH = constant titrations is shown for a sample of five experiments in Figure 5.9 for pH = 9.00 and pH = 10.0, respectively.

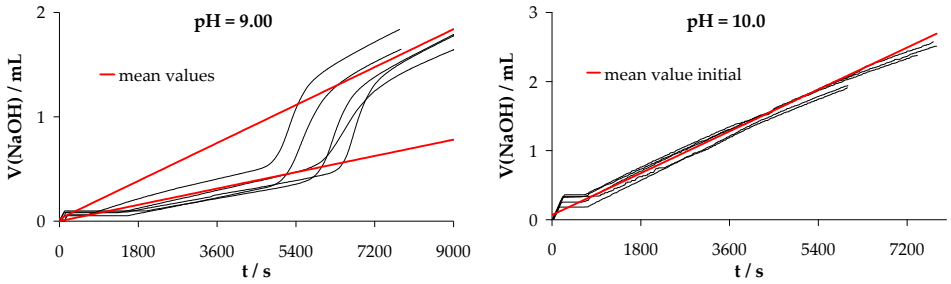

Figure 5.9: Time-development of the necessary volume of 10 mM NaOH in pH = constant titration shown for a sample of five single measurements for pH = 9.00 (left) and pH = 10.0 (right). Mean values show the averaged slopes and intercepts before and after nucleation, respectively, for pH = 9.00. At pH = 10.0, the nucleation event is hardly detectable and only the initial slope and intercept are averaged. For further explanations see text.

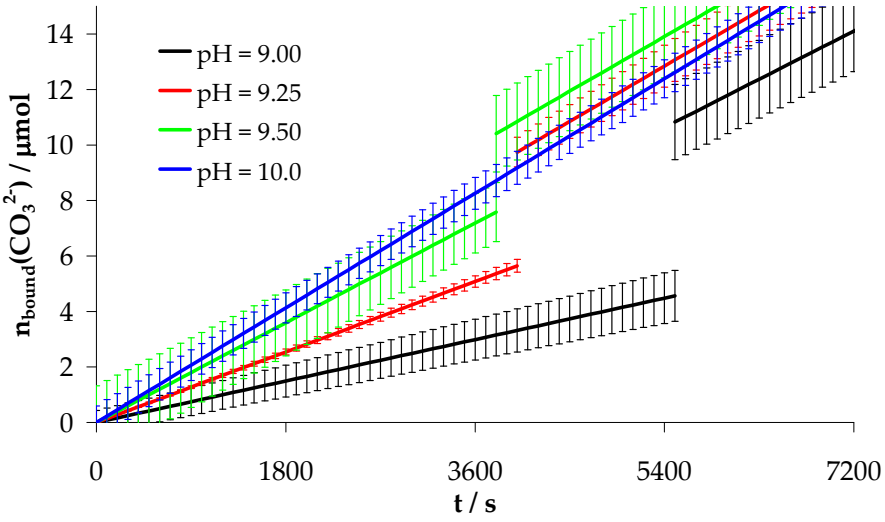

Figure 5.10: Time-development of the bound amounts of carbonate ions as calculated from the mean values of the volume necessary in pH = constant titration. Error bars depict the particular standard deviation. For further explanations see text.

At pH = 9.00, the nucleation event is clearly detectable whereas a linear time development before and after nucleation is obvious, respectively. In analogy to the averaging of the calcium measurements, the initial and final slopes and intercepts of the sample of five measurements are averaged and the particular standard deviations are determined.

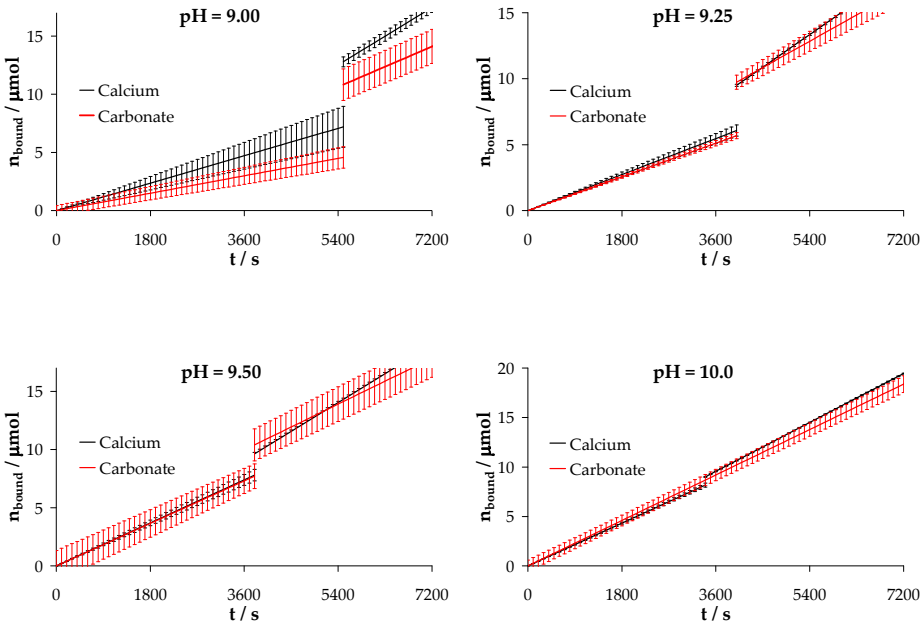

Figure 5.11: Comparison of the time-developments of the bound amounts of calcium (black) and carbonate (red) ions before and after nucleation. Within experimental accuracy, clusters and particles exhibit a composition of $Ca^{2+} : CO_3^{2-} = 1 : 1$. For further explanations see text.

This analysis is done analogously for pH = 9.25 and pH = 9.50. However, at pH = 10.0, the nucleation event is hardly detectable and only the initial volume time-development is averaged. The mean values of the volume-time-development determined in this way can be converted into the bound amounts of carbonate ions as discussed in detail in introducing section 5.1. The derived time-development of the bound amount of carbonate ions is illustrated in Figure 5.10; error bars depict the particular standard deviation. The similarity of the particular time-developments of the bound amounts of carbonate ions and the bound amounts of calcium ions as shown in Figure 5.8, respectively, is obvious. However, the more distinct carbonate binding after nucleation at pH = 10.0 can not be resolved within experimental accuracy.

A detailed comparison of calcium and carbonate binding is presented in Figure 5.11. Within experimental accuracy, calcium and carbonate binding are equal before and after nucleation, respectively, at all pH-values investigated. Only at pH = 9.0, a slight deviation is apparent. However, a composition of $Ca^{2+} : CO_3^{2-} = 1 : 1$ after nucleation is obvious and the flatter time-development of carbonate binding has to be corrected to the steeper calcium binding or *vice versa*, thus indicating equal calcium and carbonate binding at pH = 9.0. The in each case flatter slope in post nucleation carbonate ion binding is peculiar and obviously induces the

covered nucleation event at pH = 10.0. This can be ascribed to a reduced mass transport of calcium ions from the calcium compartment into the carbonate compartment, because nucleation of calcium carbonate takes place in the calcium compartment first, leading to a decrease of the gradient of concentration on one hand and to a possibly reduced permeability of the membrane due to closed pores on the other hand.

5.2.2 Beaker Experiments

Calcium binding is analyzed at much higher resolution in beaker experiments than in double diffusion experiments as demonstrated by comparison of the particular time-developments illustrated in Figure 5.12 and Figure 5.7 (cp. section 5.2.1), because the fluctuation of calcium binding is reduced by exchanging the mass transport of calcium *via* diffusion by dosing calcium solution. Largely, the improvement is due to dispensing with the dialysis membrane and its fluctuations of permeability.

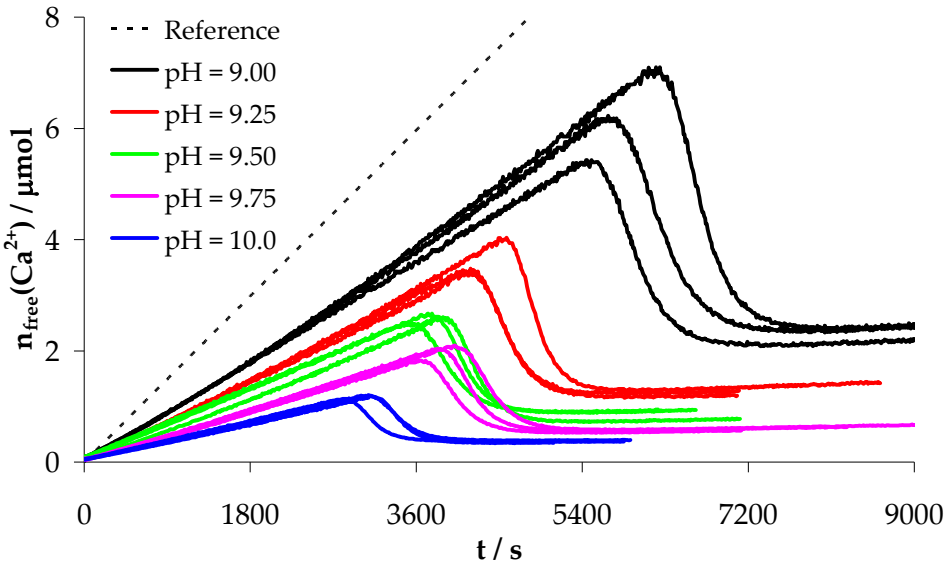

Figure 5.12: Time-development of the free amount of calcium ions measured by a calcium ion sensitive electrode (Ca-ISE) in carbonate buffer at different pH-values. The reference line reflects the amount of calcium ions added by dosing. Calcium ions are bound more distinct at higher pH-values indicating an underlying binding equilibrium with carbonate ions. In comparison to double diffusion experiments, the resolution is improved. For further explanations see text.

Figure 5.13 illustrates the pre-nucleation time-development and post-nucleation time-development of the bound amount of calcium ions as averaged from three single measurements in analogy to the discussion of section 5.2.1.

The resolution of the measurements of bound carbonate ions *via* pH = constant titration is improved as well as the resolution of the measurements of bound calcium ions. Figure 5.14 gives a comparison of the particular bound amounts of calcium ions and carbonate ions, respectively. Black lines give the averaged calcium binding. Red lines illustrate single measurements calculated according to equation (5.9) from the volume of 10 mM NaOH necessary in pH = constant titration. These single measurements have to be offset- and slope-corrected, respectively, in order to fit the measured time-development of the bound amount of calcium.

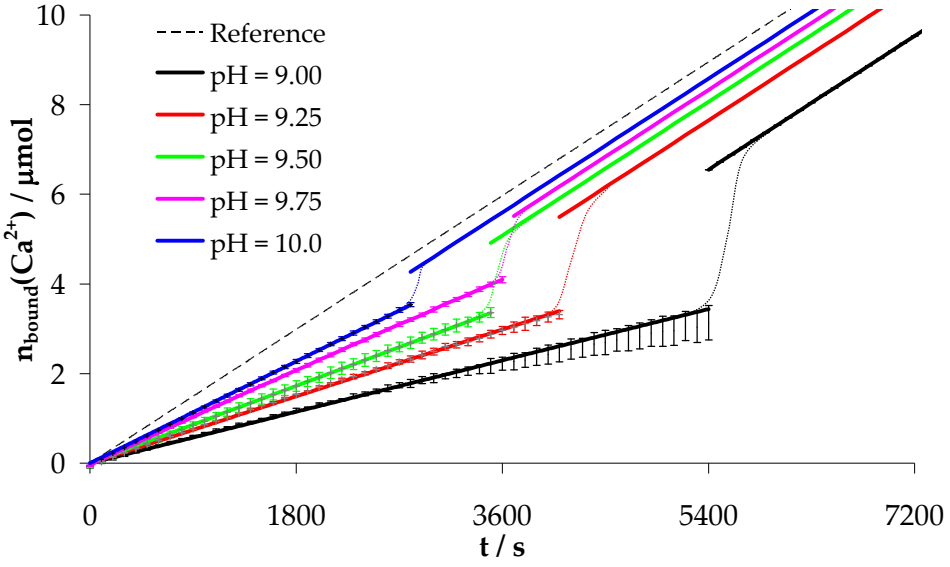

Figure 5.13: Bound amount of calcium ions in clusters (before nucleation) and in particles (after nucleation). For further explanations see text.

These corrections are shown as green lines, respectively. The offset correction is due to initial pH-electrode tune-in and complies with the offset of the linear pre-nucleation time-development if extrapolated to the ordinate. The slope correction is adjusted to a post-nucleation particle composition of Ca^{2+} : CO_3^{2-} = 1 : 1. The slope correction can be attributed to an interaction of different errors possible in pH = constant titration:

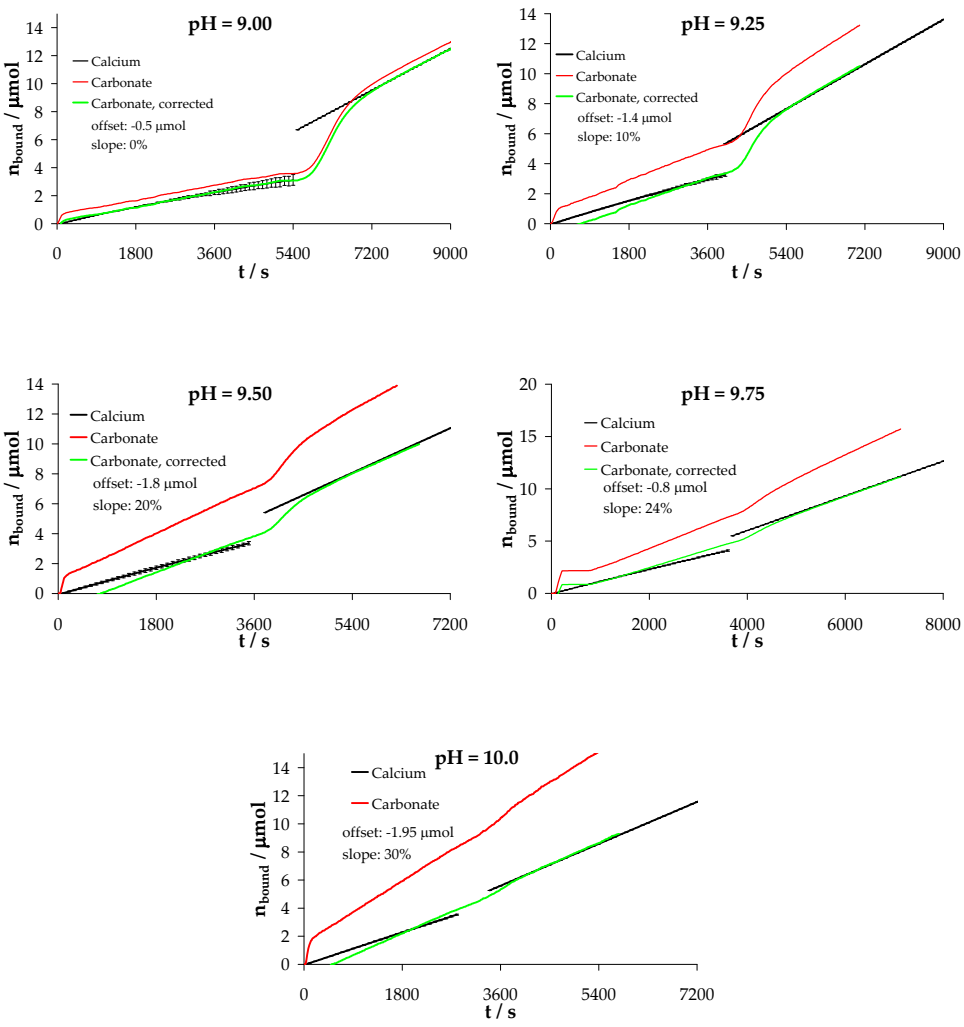

Figure 5.14: Comparison of the time-developments of the bound amounts of calcium and carbonate ions before and after nucleation. Within experimental accuracy, clusters and particles exhibit a composition of $Ca^{2+} : CO_3^{2-} = 1 : 1$. For further explanations see text.

(i) Error of literature pK-values of the carbonate buffer equilibrium giving a changed ratio of bicarbonate and carbonate as applied in equation (5.9) for the calculation of the bound amounts of carbonate from NaOH volumes (cp. Section 5.1),

(ii) growing error in pH-measurements with increasing pH-values attributed to the pH-electrodes membrane properties,

(iii) error of titers of the dilute NaOH and

(iv) possible in-diffusion of atmospheric carbon dioxide with an increased rate at higher pH-values.

The role of each error could not be revealed, while in-diffusion of atmospheric carbon dioxide is proximate but does not result in a distinct error of the bound amount of calcium, because approx. $7.8 \cdot 10^{-5}$ mol of carbonate ions are initially present at pH = 10.0 and the in-diffused extra-amount of carbon dioxide if judged by the slope offset over the entire duration of the experiment is about $3 \cdot 10^{-6}$ mol giving a maximum error of approx. 4% in the carbonate concentration.

In analogy to the discussion of section 5.2.1, the comparison of the time-development of the bound amount of calcium and carbonate ions as illustrated in Figure 5.14 shows that calcium binding is equal to carbonate binding at all times and pH-values. The minor slope-offset of the calculated carbonate binding in the prenucleation stage can be attributed to initial pH-electrode tune-in.

5.2.3 Comparison of Double Diffusion and Beaker Experiments

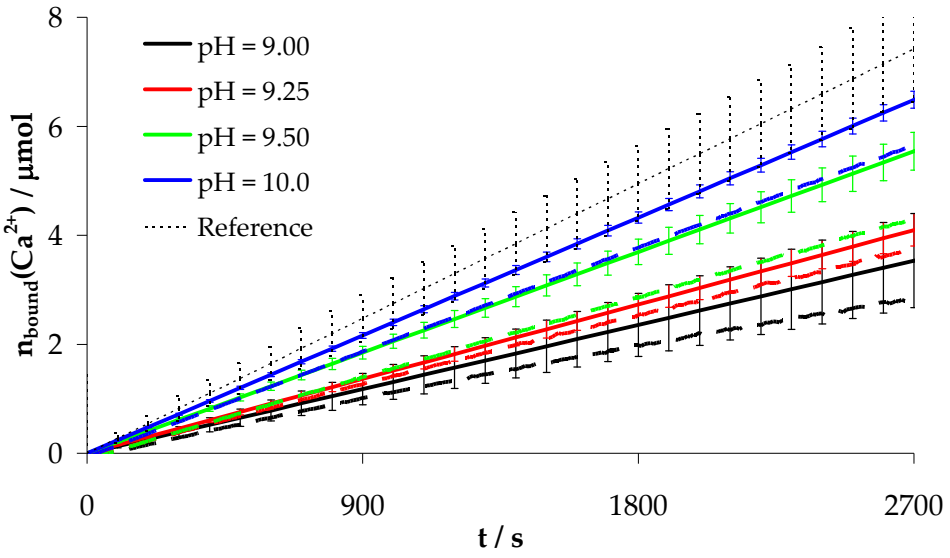

Figure 5.15: Comparison of the bound amounts of calcium ions in the beaker (dashed lines, respectively) and double diffusion experiments (solid lines, respectively), where the beaker experiments are corrected to the double diffusion experiments. The reference line gives the mean value of the experiments in the calcium/water diffusion system. Error bars give standard deviations of double diffusion experiments, respectively. Within experimental accuracy, analogous calcium binding is detected in both experimental setups. For further explanations see text.

Figure 5.15 illustrates the comparison of the time-developments of bound amounts of calcium in beaker and double diffusion experiments in the pre-nucleation stage. Here, the

time-development of the beaker experiments are corrected to the time-development of the double diffusion experiment, respectively: The time-development of the reference experiment of double diffusion experiments is a factor of approximately 1.7 steeper than the time-development of the reference experiment of beaker experiments. Thus, the particular time-developments of beaker experiments are corrected by a factor of 1.7 in order to facilitate comparison with double diffusion experiments.

At pH = 9.00 and pH = 9.25, the time-developments of beaker and double diffusion experiments are congruent taking the standard deviation of single experiments of the double diffusion experiments as depicted in error bars into account. At pH = 9.50 and pH = 10.0, the particular time-developments as analyzed in beaker experiments are out of the standard deviation of single double diffusion measurements. However, it has to be taken into account that the standard deviation of the reference experiment of double diffusion experiments still justifies the assumption of equal time-developments, respectively. The flatter time development of beaker experiments at all pH-values is peculiar. This is to my opinion a sign of insufficient averaging of double diffusion experiments, i.e. a too small sample of experiments, giving a too steep averaged slope. Concurrently, calcium addition into the carbonate buffer in double diffusion experiments –steady state diffusion within approx. 10 mM gradient of concentration throughout 1.74 cm^2 membrane surface- is roughly 1.7 times faster than in beaker experiments– dosing calcium solution in 0.2 µL steps through an open rounding of 2.7 mm- if judged by the slope of reference experiments. Thus, in case of slow dynamics of the cluster equilibrium, one would expect a flatter time-development in double diffusion experiments.

5.2.4 Physicochemical Characterization of the Cluster Equilibrium

As pointed out in sections 5.2.1, 5.2.2 and 5.2.3, the beaker experiments provide higher resolution and are thus evaluated in this section.

The formation of clusters can be quantified by a multiple-binding equilibrium. The carbonate ions are considered as centre-ion and calcium ions as binding ions in cluster formation as illustrated in Figure 5.16, because calcium solution is added to carbonate buffer and carbonate ions are the excess species in the experiments. Thus, it is reasonable to consider a

binding of calcium to carbonate[3]. The analysis is only reasonable in the pre-nucleation stage of the experiments, because after nucleation, the clusters are not detectable due to the formation of the new phase. Therefore, successive analysis is aborted at the time of nucleation.

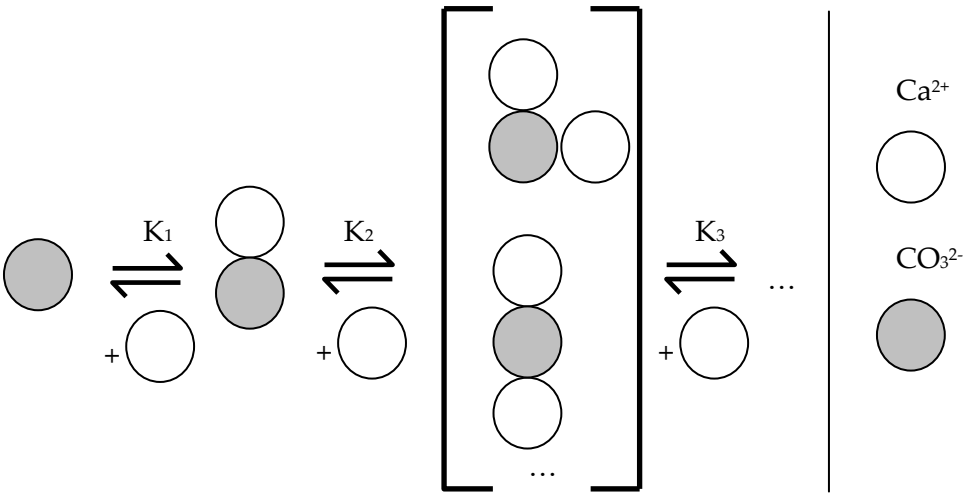

Figure 5.16: Multiple-binding equilibrium for a carbonate centre-ion and binding calcium ions. The bracket indicates that there are various three-dimensional possibilities for the structure of the particular steps, while the opposite arrangement is the most favorable. However, all possible bonding structures in a particular step of the equilibrium system are assumed to be equal and independent. For further explanations see text.

The law of mass action according to Figure 5.16 gives for the concentration of bound calcium $c_{bound}(Ca^{2+})$ and for the total –i.e. bound and free- carbonate concentration $c_{total}(CO_3^{2-})$

$$\begin{aligned} & c_{bound}(Ca^{2+}) = \sum_{i=1}^{n} i \cdot c(CO_3^{2-}Ca_i^{2+}) \\ & = K_1 \cdot c_{free}(Ca^{2+}) \cdot c_{free}(CO_3^{2-}) + 2K_2K_1\left[c_{free}(Ca^{2+})\right]^2 c_{free}(CO_3^{2-}) \text{ and} \\ & +3 \cdot K_3 \cdot ... \end{aligned} \tag{5.12}$$

$$\begin{aligned} & c_{total}(CO_3^{2-}) = \sum_{i=0}^{n} c(CO_3^{2-}Ca_i^{2+}) \\ & = c_{free}(CO_3^{2-}) + K_1 c_{free}(Ca^{2+}) c_{free}(CO_3^{2-}) \ . \\ & +K_2K_1\left[c_{free}(Ca^{2+})\right]^2 c_{free}(CO_3^{2-}) + K_3 \cdot ... \end{aligned} \tag{5.13}$$

[3] The inverted physicochemical scenario –binding carbonate ion to calcium ions- cannot describe the experimental data and is not discussed.

Combination of equations (5.12) and (5.13) gives the ratio of the amount of bound calcium to the total amount of carbonate

$$\frac{n_{bound}(Ca^{2+})}{n_{bound}(CO_3^{2-}) + n_{free}(CO_3^{2-})} = \frac{K_1 c_{free}(Ca^{2+}) + 2K_2K_1\left[c_{free}(Ca^{2+})\right]^2 + 3K_3 \cdot \ldots}{1 + K_1 c_{free}(Ca^{2+}) + K_2K_1\left[c_{free}(Ca^{2+})\right]^2 + K_3 \cdot \ldots} \cdot \tag{5.14}$$

Assuming that all binding structures as illustrated in Figure 5.16 are equal and independent, i.e. $K = K_1 = K_2 = K_3 = \ldots$, and the number of calcium ions that bind to a carbonate ion is x, equation (5.14) gives

$$\frac{n_{bound}(Ca^{2+})}{n_{bound}(CO_3^{2-}) + n_{free}(CO_3^{2-})} = x\frac{K \cdot c_{free}(Ca^{2+})}{1 + K \cdot c_{free}(Ca^{2+})}. \tag{5.15}$$

Rearrangement of equation (5.15) accounting for a constant ratio $\frac{n_{bound}(Ca^{2+})}{n_{bound}(CO_3^{2-})} = 1$ as shown in sections 5.2.1, 5.2.2 and 5.2.3 gives

$$\nu = 1 + \frac{n_{free}(CO_3^{2-})}{n_{bound}(Ca^{2+})} = \frac{1}{x} + \frac{1}{x \cdot K} \cdot \frac{1}{c_{free}(Ca^{2+})}. \tag{5.16}$$

The number of calcium ions that bind a carbonate ion x can be interpreted as the number of equilibria in Figure 5.16. The carbonate ions are considered to provide a 'lattice' for the binding of calcium ions, i.e. the model regards a single –quasi isolated- carbonate ion and analyses the binding of calcium ions to it. 'Microscopic' refers to the exclusive view on such an independent carbonate ion as illustrated in Figure 5.17. The equilibrium constant K characterizes the ion pair formation regarding this microscopic scenario. Moreover, it is important to note that the physicochemical model does not imply calcium ion excess in clusters consisting of several microscopic calcium/carbonate ion pairs if $x > 1$. The carbonate ions in the bulk of a cluster are still considered to be isolated -a 'lattice' for binding calcium ions- and bound calcium ions cannot be assigned exclusively to a particular carbonate ion. Because all binding structures are assumed to be equal and independent (cp. Figure 5.16), a value of $x > 1$ means that a single carbonate ion is capable of additionally binding a calcium ion, which is already bound in a microscopic neighbor-ion pair or a free calcium ion. Thus,

from a macroscopic point of view, the number of calcium ions that can bind a single carbonate ion x is an averaged, dynamic coordination number of microscopic ion pairs, and the macroscopic observation of a ratio of bound ions $Ca^{2+} : CO_3^{2-} = 1 : 1$ does not contradict values $x > 1$. The averaging of x includes the ions which are not bound in clusters and thus does not reflect the exact coordination number in clusters, which is higher.

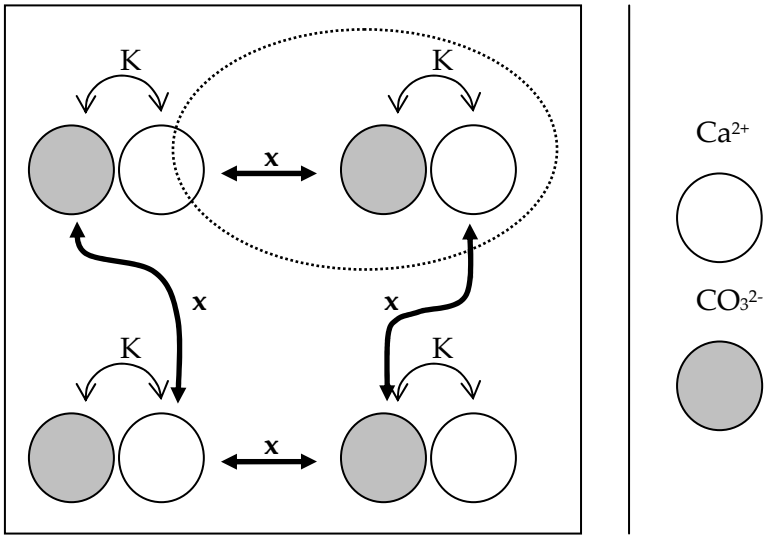

Figure 5.17: Schema clarifying the definition of microscopic ion pairs. One microscopic ion pair, which is considered in the multiple binding equilibrium (cp. Figure 5.16), is indicated by the dashed circle. In the microscopic scenario, the number of calcium ions that bind a carbonate ion x gives calcium ion excess for $x > 1$. In the macroscopic point of view indicated by the solid box, the ratio of bound calcium to bound carbonate is 1:1. The parameter x thus relates to a coordination number. For further explanations see text.

Note that equation (5.16) depends on the free calcium concentration, the particular equilibrium constant and the number of calcium ions bound per carbonate ion only. Thus, $c_{free}(Ca^{2+}, t)$, $n_{bound}(Ca^{2+}, t)$ and $n_{free}(CO_3^{2-}, t)$ have to be known for the evaluation of equation (5.16).

$c_{free}(Ca^{2+}, t)$ is accessible directly from calibration and calcium potential measurements and is shown for a sample of 3 measurements until the time of nucleation in Figure 5.18. The time-development is linear and the particular mean values were fitted by linear regression with origin intercept and are shown as red lines, respectively. $n_{bound}(Ca^{2+}, t)$ is fitted linearly as discussed in section 5.2.2 and shown in Figure 5.12 (cp. section 5.2.2). With the ratio of bound ions $Ca^{2+} : CO_3^{2-} = 1 : 1$, $n_{free}(CO_3^{2-}, t)$ can be calculated by (cp. equation (5.5), section 5.1)

$$n_{free}(CO_3^{2-}, t) = \Lambda\left(CO_{3,aq.}^{-}\right)_{pH}\left[n_{total}(carbonate, t=0) - n_{bound}(Ca^{2+}, t)\right]. \quad (5.17)$$

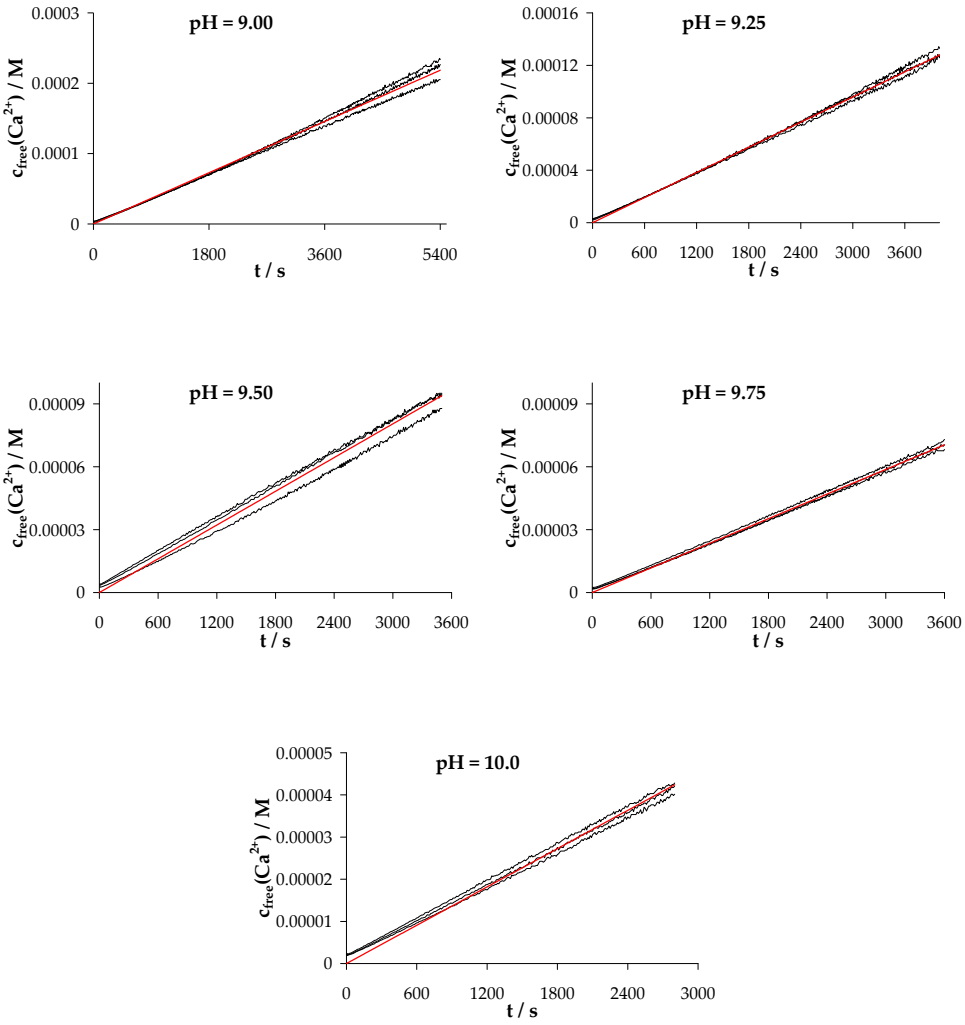

Figure 5.18: Illustration of the linear regression of the mean value of particular time-developments of the free calcium concentration in the pre-nucleation stage. For further explanations see text.

The analyses according to equation (5.16) are shown in Figure 5.19. The analysis gives perfect lines, respectively, with binding parameters

pH = 9.00: x = 1.05; K = 1350 M^{-1},

pH = 9.25: x = 1.08; K = 1250 M^{-1},

pH = 9.50: x = 1.15; K = 967 M^{-1},

pH = 9.75: x = 1.26; K = 890 M^{-1} and

pH = 10.0: x = 1.47; K = 713 M^{-1}.

The number of calcium ions that bind and coordinate a carbonate ion increases with increasing pH-values, while the equilibrium constant decreases. In this regard, it is interesting to interpolate the development of binding parameters. In an empirical approach, this is done by a plot of the particular slopes of the time-developments $c_{free}(Ca^{2+}, t)$ and $n_{bound}(Ca^{2+}, t)$.

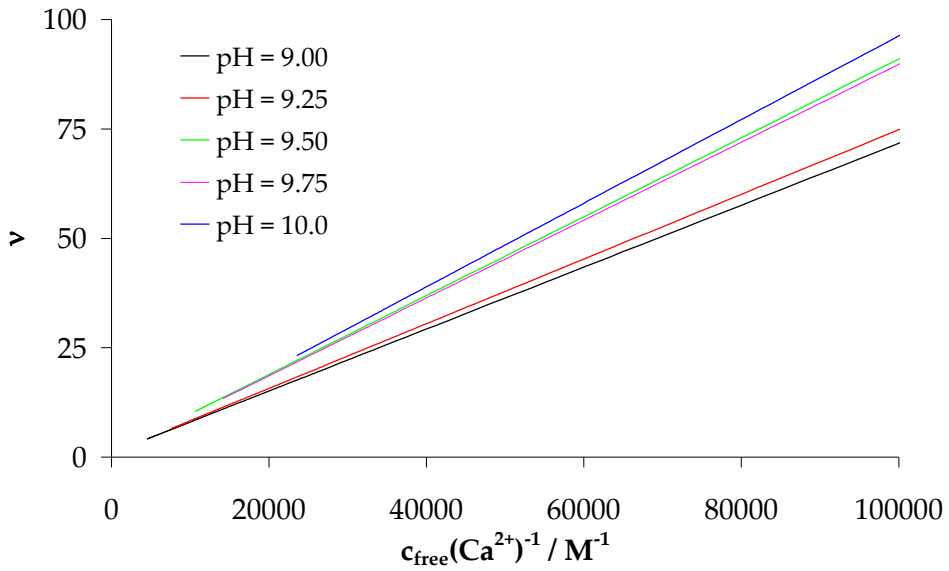

Figure 5.19: Plot of the multiple binding equilibrium parameter ν (cp. equation (5.16)) *versus* the reciprocal concentration of free calcium ions. Note that minimum reciprocal free calcium concentrations correspond to free calcium ion concentrations at the time of nucleation. For further explanations see text.

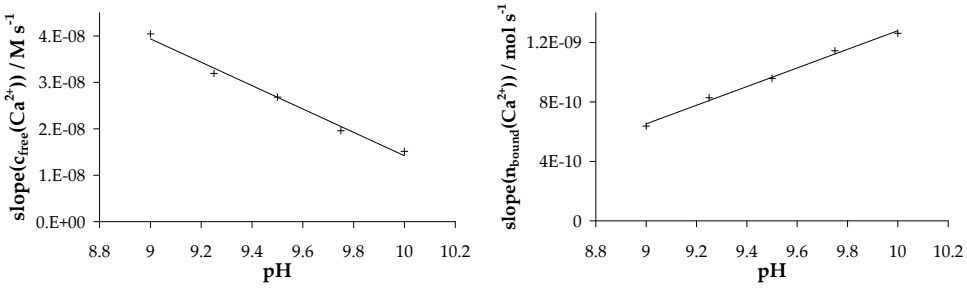

Figure 5.20: Empirical plot of the slopes of the free calcium concentration (cp. Figure 5.18) and of the bound amount of carbonate (cp. Figure 5.13) *versus* pH-values. Both developments can be fitted linearly with regression coefficients as good as 0.990 and 0.994, respectively. For further explanations see text.

This plot is illustrated in Figure 5.20. In both cases, the data can be fitted linearly with minor deviation. The obtained pH-development of slopes facilitates the calculation of the time-

development of the free calcium concentration and of the bound amount of calcium, respectively, and with equation (5.17) the calculation of the free amount of carbonate at other pH-values, respectively, and herewith an interpolation of equation (5.16). This interpolation is performed within steps of 0.1 pH-units and extrapolated to pH = 8.5 and pH = 10.5, respectively. The obtained interpolation of binding parameters is illustrated in Figure 5.21.

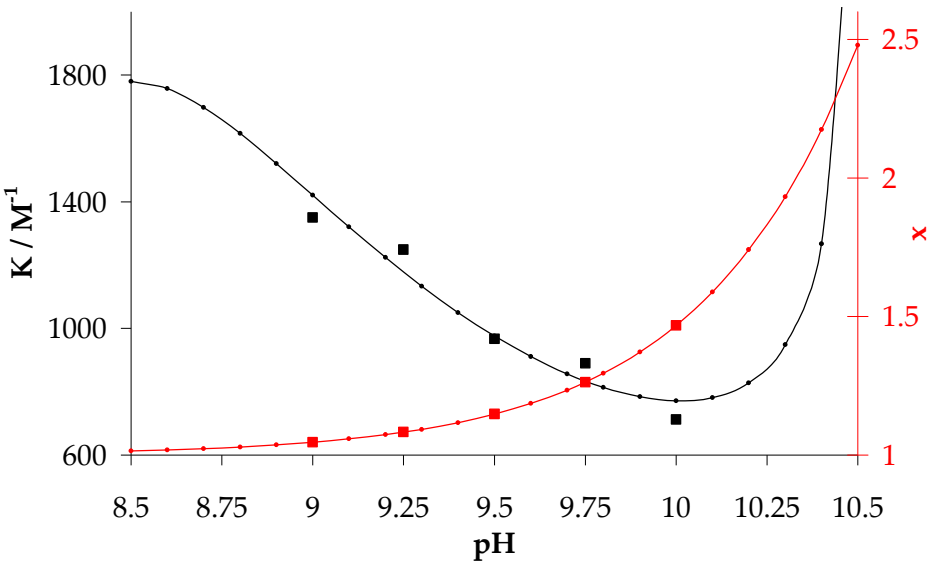

Figure 5.21: Interpolated pH-development of the multiple binding equilibrium parameters (cp. equation (5.16)). Emphasized points give the binding parameters as derived from the plot shown in Figure 5.19. For further explanations see text.

The equilibrium constant K exhibits a minimum value at pH = 10.05, while the number of calcium ions that bind a carbonate ion x –which is the dynamic averaged coordination number of microscopic calcium/carbonate ion pairs (cp. Figure 5.17) in clusters- increases monotonously from x = 1 with increasing pH-value. As already discussed above, it is crucial to note that the derived binding parameters are microscopic parameters in the picture of Figure 5.16 and Figure 5.17. It is obvious that the microscopic equilibrium constant K does not adequately describe the macroscopic scenario, because the increasing coordination number complies with an increased, macroscopic equilibrium constant for the calcium/carbonate ion pair formation in clusters consisting of several microscopic ion pairs. Comparison of the ratio of bound ions Ca^{2+} : CO_3^{2-} = 1 : 1 with equation (5.16) shows that in a macroscopic point of view (x = 1), the slope of a plot of ν *versus* the free calcium concentration gives the reciprocal equilibrium constant for the formation of

calcium/carbonate ion pairs. Thus, the macroscopic equilibrium constant K′ for the formation of calcium/carbonate ion pairs in clusters can be calculated by

$$\mathrm{Ca}^{2+}_{\mathrm{aq.}} + \mathrm{CO}^{2-}_{3,\mathrm{aq.}} \overset{K'}{\rightleftharpoons} \left[\mathrm{CaCO_3}\right]_{\mathrm{cluster,aq.}}$$

$$\frac{c\left(\left[\mathrm{CaCO_3}\right]_{\mathrm{cluster,aq.}}\right)}{c\left(\mathrm{Ca}^{2+}_{\mathrm{aq.}}\right)\cdot c\left(\mathrm{CO}^{2-}_{3,\mathrm{aq.}}\right)} = K' = x \cdot K \qquad (5.18)$$

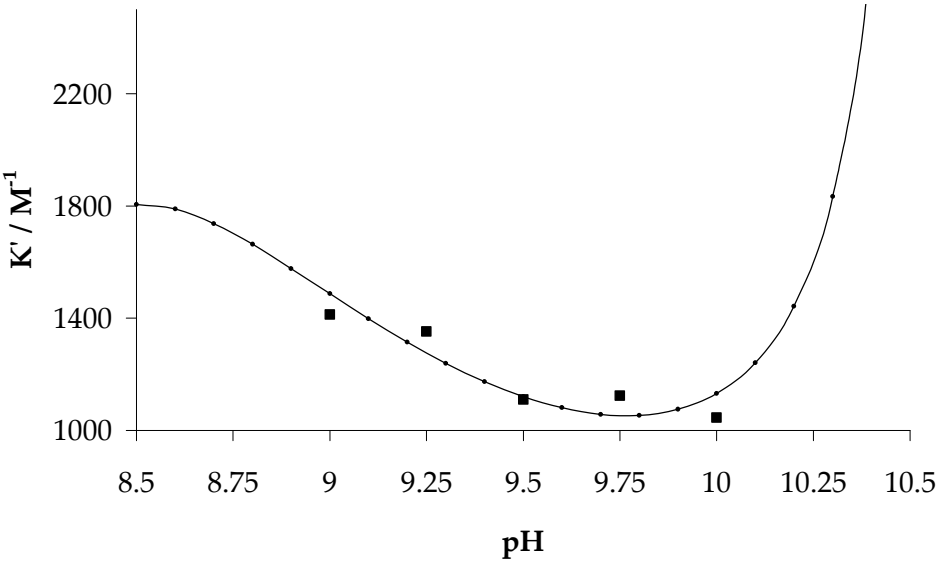

Figure 5.22: Plot of the macroscopic equilibrium constant K′ (cp. equation (5.18)) of cluster formation *versus* pH-value. Emphasized points give the values as calculated from the parameters derived from Figure 5.19. For further explanations see text.

Equation (5.18) accounts for a macroscopically increased strength of binding that is microscopically expressed by an increased number of calcium ions bound per carbonate ion. It is crucial to note that the derived equilibrium constant K′ does not characterize the equilibrium $w \cdot \mathrm{Ca}^{2+}_{\mathrm{aq.}} + w \cdot \mathrm{CO}^{2-}_{3,\mathrm{aq.}} \rightleftharpoons \left\{\mathrm{CaCO_3}\right\}_{w,\mathrm{aq.}}$. The cluster concentration and the particular equilibrium constant are unknown and the number of ions bound in clusters w is not accessible at this point. The cluster sizes will be discussed in section 5.2.6.

The pH-development of the macroscopic equilibrium constant K′ for calcium/carbonate ion pairs in clusters is illustrated in Figure 5.22. The macroscopic binding constant exhibits a minimum value at $\mathrm{pH} \approx 9.80$ and gives with $-RT\ln K' = \Delta_R G^{\otimes}_{\text{ion pair}}$ (R gas constant, T

temperature) the standard free energy of ion pair formation, whose pH-development is illustrated in Figure 5.23.

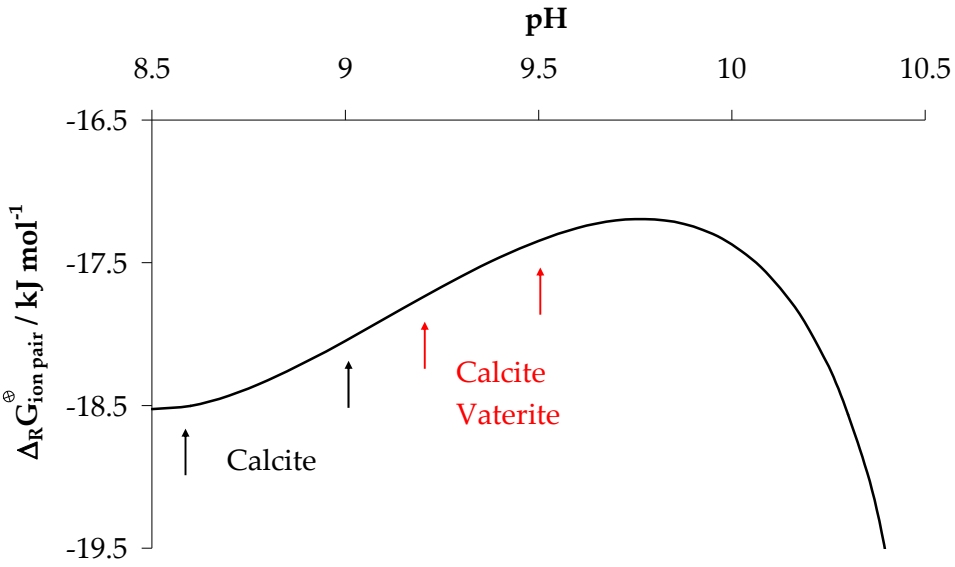

Figure 5.23: GIBBS standard reaction energy $\Delta_R G^{\otimes}_{ion\ pair}$ for the formation of calcium/carbonate ion pairs in calcium carbonate clusters *versus* pH-value. The corresponding minimum in binding energy at pH ≈ 9.80 apparently affects the polymorphs formed from nucleated ACC. Strong binding in clusters give the most stable polymorph calcite, while at weaker binding the least stable crystalline polymorph vaterite is formed additionally. For further explanations see text.

Recently, there is growing evidence that different phases of ACC exist [23, 52-54], i.e. ACC with different short range orders that are similar to the long range order of the particular crystalline polymorph, which is formed out of the particular ACC. X-ray absorption spectroscopy (XAS) and extended X-ray absorption fine structure (EXAFS) studies facilitate the determination of such short range orders in ACC as shown for three types of stable biogenic ACC-species in Figure 5.24 (as discussed in [23]). The coordination shell of calcium ions is different for all three types shown, while the structure is related to the crystalline structure of monohydrocalcite. The *in vivo* stable ACC of *Ficus microcarpa* (c) rapidly converts to calcite if extracted in an aqueous environment, the other two ACC species (a, b) are also stable *in vitro*, while it is not known what structurally differentiates stable ACC forms from non-stable ACC forms. Besides stable biogenic species, ACC occurs as transient precursor phase in biomineralization. XAS and EXAFS studies on such precursor species show that aragonitic short range order is preformed in ACC of the freshwater snail *Biomphalaria glabrata*

[52], and calcitic short range order is preformed in ACC of sea urchin embryos [54]. LAM *et al.* [53] discussed that additives can influence the short range order of *in vitro* nucleated ACC. The change in the microscopic mechanism of cluster formation which affects the binding energy of ions bound in clusters gives a proximate background and basis for the nucleation of different ACC phases that later transform into the particular crystalline polymorph, since the discussed clusters are the precursor species of nucleated ACC.

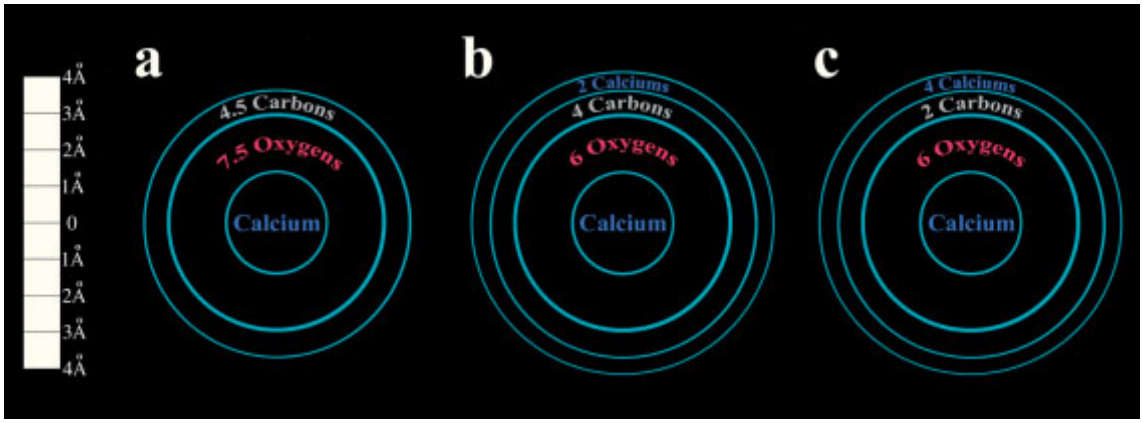

Figure 5.24: Schematic representation (taken from [23]) of the information obtained from EXAFS measurements of biogenic stable ACC of: a) *Pyura pachydermatina* body spicules; b) Cuticle of the lobster *Homarus americanus*; c) Cystoliths from the leaves of *Ficus microcarpa*. The blue circles represent the coordination shells, within which the number of atoms in the shell is reported. The coordination shells are all different and are related to the coordination of crystalline monohydrocalcite.

On one hand, the averaged, dynamic coordination number x increases with increasing pH-value and indicates structural changes of clusters. On the other hand, the binding energy decreases with increasing pH-values indicating that less stable orders can be preformed at higher pH-values. As indicated in Figure 5.23, low averaged, dynamic coordination numbers of $x \approx 1$ facilitates the formation of pure calcite at high binding strength in clusters, while at increasing x and decreasing binding strength, vaterite is nucleated additionally. Figure 5.25 shows WAXS diffractograms of samples collected from the calcium compartment of double diffusion experiments approx. 3 hours after the nucleation of ACC. It is apparent that calcite only is formed at pH-values according to strong ion binding, while with decreasing strength of binding vaterite is formed additionally. Aragonite could not be detected clearly so far.

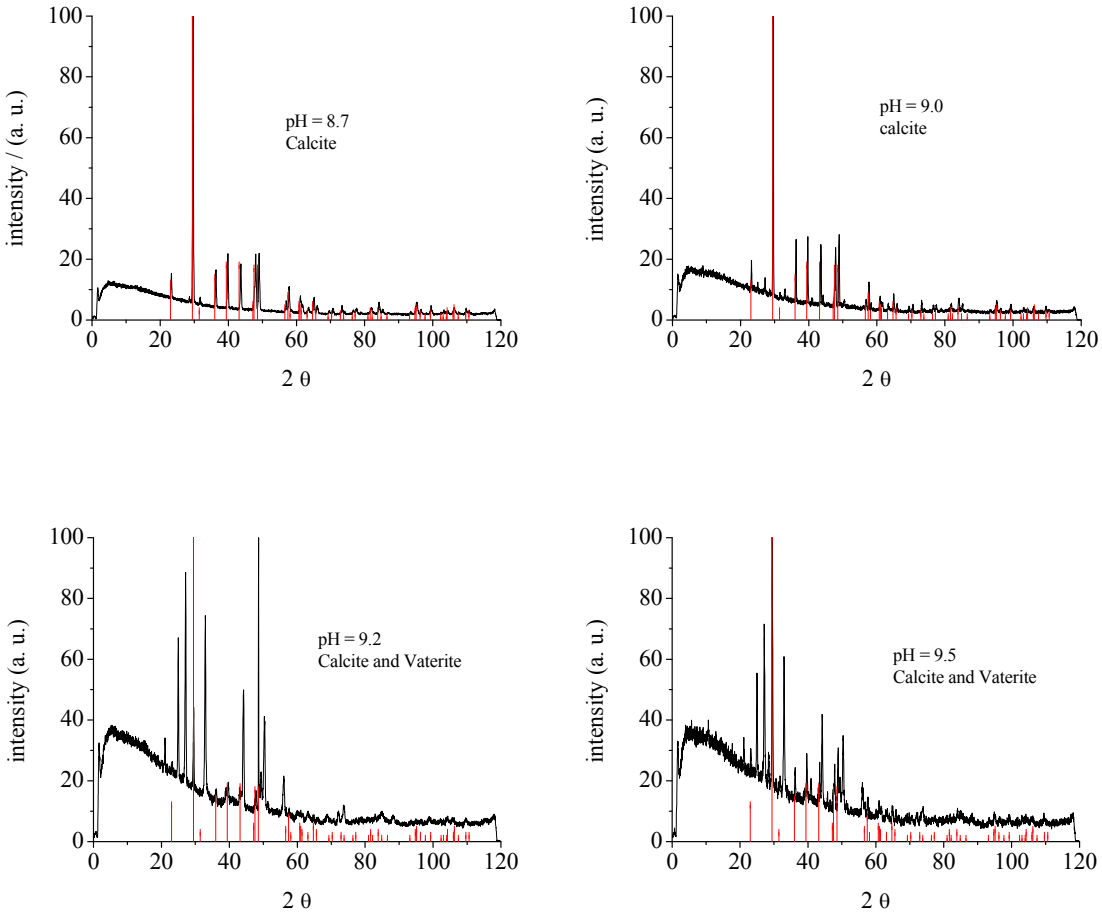

Figure 5.25: WAXS spectra of samples that were drawn 3 hours after nucleation of ACC in the calcium compartment of double diffusion experiments (black). Reference spectrum is shown for calcite, respectively (red). Apparently, only calcite is formed at strong binding of ions in clusters. With decreasing strength of binding, vaterite is detected additionally. Some signals at pH = 9.50 might be related to aragonite but a clear evidence can not be given at this point. All peaks are normalized to the most intense peak. For further explanations see text.

5.2.5 Ion Products

The free ion product can be calculated with the mean values of the free concentration of calcium ions and the free concentration of carbonate ions (cp. section 5.2.4, respectively, equation (5.17)). The time-developments of the free ion products are illustrated in Figure 5.26. Since averaging is not approved during nucleation, the particular time-developments are indicated by dotted lines, respectively. Additionally given are the solubility products of

vaterite, aragonite and calcite as published in [55][4]. At pH = 9.00 to pH = 9.50, the solubility product of the nucleated phase is $3.1 \cdot 10^{-8} M^2$ (ACC I), while the solubility product is $3.8 \cdot 10^{-8} M^2$ (ACC II) at pH = 9.75 and pH = 10.0. The different solubility products can be speculatively ascribed to the formation of different ACC species –less stable ACC II and more stable ACC I (cp. section 5.2.4.).

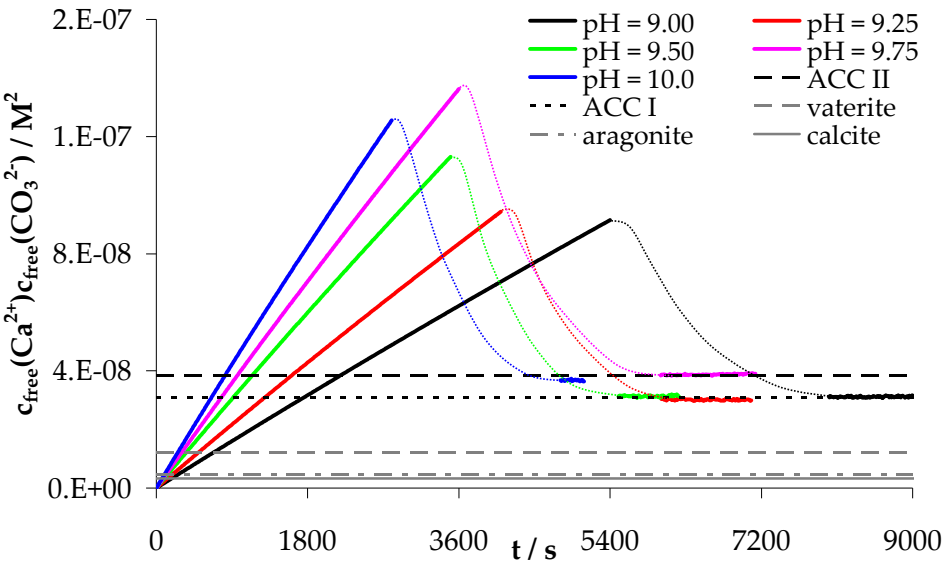

Figure 5.26: Time-development of the free ion product. Two different ACC solubilities can be found. Additionally given are the solubilities of vaterite, aragonite and calcite as determined in [55]. For explanations see text.

Sole detection of ACC II above pH = 9.75 as indicated by the solubility product does not contradict the existence of ACC I in this pH-range, because the most soluble species determines the solubility product. On the other hand, the sole detection of ACC I at lower pH-values does not exclude the existence of less stable ACC species shortly after nucleation, which may dissolve again or transform into other species, which are more stable than

[4] BRECEVIC et al. determine the solubility of ACC giving $4.0 \cdot 10^{-7} M^2$ which is approximately one order of magnitude too high.

ACC I[5]. Furthermore, the solubility of other, intermediate stable ACC-species may be masked by the solubility product of ACC II.

Since the solubility product is determined by the most soluble species, the time-development of the solubility product is not capable of indicating amorphous-crystalline transitions as long as amorphous species are present in the system.

5.2.6 Cluster Size

The cluster size can be experimentally determined in Analytical Ultracentrifugation, which was performed on a Beckman-Coulter XL-I Ultracentrifuge using RAYLEIGH interference optics at 25°C and 60,000 RPM.

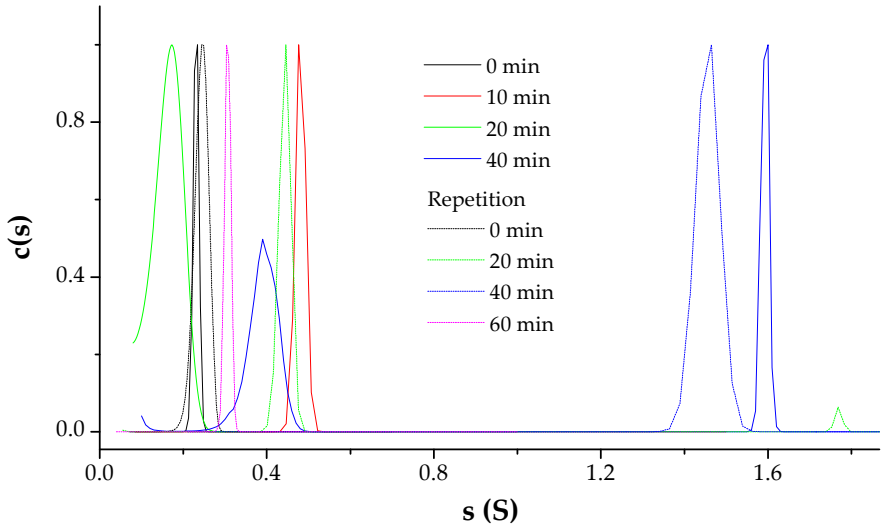

Figure 5.27: Diffusion corrected distribution of sedimentation coefficients in the pre-nucleation stage (pH = 9.00) at different times as indicated. The uncertainity of the sedimentation coefficient of ions is very high, because the sedimentation is very slow and close to the limit of detection. After 20 minutes, a second species with sedimentation coefficient of about 1.5 S can be observed, which is attributed to the clusters. Distributations are normalized to maximum peak for better comparison of data. For further explanations see text.

[5] The WAXS spectra of particles formed 3 hours after nucleation in the calcium compartment of double diffusion experiments shown in section 5.2.4 indicate the presence of vateritic ACC from pH = 9.50 on.

The samples were drawn from the reaction vessel of the carbonate compartment of double diffusion experiments (pH = 9.00) at different times before nucleation of ACC and investigated in self made 12 mm 2.5 ° titanium centerpieces. The diffusion corrected sedimentation coefficient distributions c(s) were calculated using the program Sedfit by P. SCHUCK [46, 47].

The results illustrated in Figure 5.27 show that in the initial reaction phase from 0 minutes to 20 minutes, only one species with sedimentation coefficients between 0.1 S to 0.5 S is obtained. These are the sedimenting ions as the control at 0 minutes reaction time shows. As their sedimentation is very slow and close to the limit of sedimentation analysis, the uncertainty in the sedimentation coefficient is rather high, as is also indicated by a repetition experiment (dashed lines in Figure 5.27). Nevertheless, at 20 minutes, a second larger species with a sedimentation coefficient of about 1.5 S is repeatedly observed, which can be attributed to the clusters. At 60 minutes, macroscopic precipitation was observed so that only dissolved ions were left in the solution. This indicates that the clusters are consumed by precipitation and their concentration is too low for detection.

It is crucial to note that the experiments are performed in carbonate buffer excess and the percentage of ions bound as illustrated in Figure 5.13 does not reflect the effective excess of all free ions. At pH = 9.0, the carbonate buffer consists of approximately 95% bicarbonate ions and approximately 4.5% carbonate ions. Thus, the amount of clusters is small at pH = 9.0 and in the order of 1 weight-% as compared to 99 weight-% ions taking all counter-ions into account, and the Sedfit evaluation routines have been tested whether they can deliver correct sedimentation coefficients for this extreme situation. Simulated data files containing 200 scans were set up for two species with s_1 = 0.3 S, D_1 = 15 cm²/s and s_2 = 1.5 S, D_2 = 8 cm²/s. The respective concentrations of components 1 & 2 were 50 % of both components in data set A and 1 % component 2 in data set B. Both sets were generated without and with noise (standard deviation 0.01).

Fitting both datasets to a non-interacting discrete 2 species model with the LAMM equation yielded the correct input parameters for data set A without and with noise. For data set B, the sedimentation coefficients for both species were correctly determined but the concentration of species 2 was slightly different from the input. Determination of the diffusion corrected sedimentation coefficient distribution yielded the correct sedimentation coefficients for all data sets, but for data set B, the concentrations were slightly lower than the

input parameters. This shows that the applied methodology can distinguish 1 weight-% of a cluster component in a mixture with 99 weight-% ions in terms of sedimentation coefficient. The concentrations, however, shall not be considered.

In summary, AUC reveals a cluster species next to a majority of sedimenting ions. Assuming spherically shaped clusters, equation (3.5) facilitates the calculation of the hydrodynamic diameter d_H from the sedimentation coefficient utilizing

$$f = 3\pi \cdot \eta \cdot d_H,$$

(frictional coefficient f (cp. equation (3.5)), solvent viscosity η) if the partial specific volume $\bar{v}$ of clusters is known. $\bar{v}$ can be calculated by the reciprocal density of clusters, which can be estimated by the densities of ACC and ikaite ($CaCO_3 \cdot 6H_2O$), $\rho_{ACC} = 1.48\ g/mL$, $\rho_{Ikaite} = 1.78\ g/mL$ [56]. The density of ACC is a good estimation since the clusters are considered to be precursors of ACC. However, it is proximate that the clusters contain water molecules and the density of ikaite gives a good approximation of the density of calcium carbonate particles containing a significant amount of water molecules. The cluster size distribution on the basis of the sedimentation coefficient distribution (peaks around 1.5 S, Figure 5.27) using the densities of ACC and ikaite is illustrated in Figure 5.28 reflecting the fluctuations of the underling distribution of sedimentation coefficients, respectively. The hydrodynamic diameter distribution is narrow, respectively, while fluctuating in between 2.1 nm and 2.5 nm assuming a density of clusters corresponding to ACC and fluctuating in between 1.6 nm and 2.0 nm assuming a density of clusters corresponding to ikaite. Assuming a density of clusters in between the density of ACC and ikaite, it is proximate to consider a hydrodynamic diameter of clusters of approximately 2 nm. The number of calcium and carbonate ions in clusters of a hydrodynamic diameter of 2 nm can be estimated on the basis of the number of ions in the unit cell of calcite if the density of calcite is referred to the density of clusters: The unit cell of calcite has the dimension 0.499 nm · 0.499 nm · 1.7061 nm and contains six calcium and six carbonate ions [57], i.e. approximately 30 ions *per* cubic-nm. The density of calcite is 2.71 g/mL and assuming a cluster density of 1.6 g/mL (which is the arithmetic average of the densities of ACC and ikaite), clusters contain approximately 17 ions *per* cubic-nm. The observed hydrodynamic radius gives a spherical volume of approximately 4 cubic-nm containing approximately 70 ions.

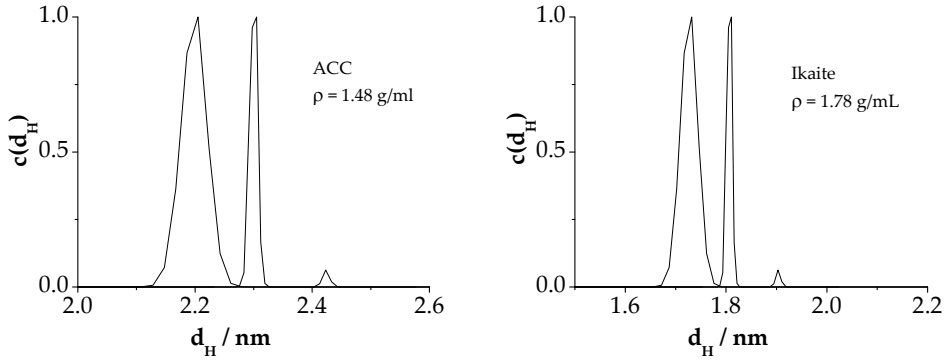

Figure 5.28: Hydrodynamic radius of pre-nucleation stage clusters as determined from the sedimentation coefficient distribution (cp. Figure 5.27, s ≈ 1.5 S) assuming a density of clusters corresponding to ACC (left) and corresponding to ikaite ($CaCO_3 \cdot 6H_2O$, right). In both cases, the hydrodynamic radius is determined to approximately 2 nm. For further explanations see text.

The ultracentrifuge experiments indicate a constant, narrow cluster size within experimental accuracy. This narrow cluster size distribution shows that the equilibria of cluster formation are very fast in comparison to the experimental time scale and the derived cluster size is an averaged value, which can be interpreted as 'motional narrowing'. The averaged cluster size is proximately time-independent as indicated by within experimental accuracy equal size at 20 minutes and 40 minutes reaction time.

The physicochemical characterization of the cluster formation (section 5.2.4) and the -due to fast formation equilibria- narrow cluster size distribution shows that the formation of clusters in the pre-nucleation stage can be described by equilibrium-thermodynamics. Nucleation interferes with these equilibria and leads to the formation of the new phase. Further inconsistencies with CNT and their particular impact on CNT are discussed in section 5.4.

5.2.7 Calcium Carbonate Precipitation at Minimum Cluster Binding Energy

As discussed in sections 5.2.4 and 5.2.5, different ACC species might exist *in vitro* that transform into the particular crystalline polymorph. The solubility products indicate (cp. Figure 5.26, section 5.2.5) the formation of a less stable ACC species at pH = 9.75 and pH = 10 (ACC II) and the formation of a more stable ACC species at lower pH-values (ACC I). The less stable ACC species transforms into vaterite and the more stable species transforms into calcite. The clusters might provide the precursor species of the particularly nucleated ACC;

i.e. at high binding strength in clusters, predominantly ACC I is formed and subsequently pure calcite is obtained. With decreasing binding strength, additionally vaterite and potentially aragonite are finally formed. In this regard, the transformation of clusters into the particular ACC species has to be considered to be a stochastical process: At high binding strength in clusters, the probability of the formation of an ionic arrangement similar to the thermodynamically stable arrangement -which is similar to calcite- is high. Thus, most of clusters will transform into calcitic ACC, while only a negligible number will transform into the other ACC species and then dissolve quickly. This scenario would indicate that calcitic ACC corresponds to ACC I. With decreasing binding strength, the probability of an ionic arrangement similar to thermodynamically less stable arrangements (which are similar to vaterite and aragonite) increases, and vateritic ACC might correspond to ACC II. Concurrently, the averaged, dynamic coordination number x (cp. section 5.2.4) indicates a structural change of clusters with increasing pH-value, i.e. a higher coordination in clusters at low binding strength, when vaterite is formed. This agrees with the higher coordination number found in vaterite (coordination number 12) than found in calcite (coordination number 6). It is crucial to note that the short range order coordination in clusters and particular ACC species may just be close to the crystalline coordination number, while additionally water molecules may be incorporated[6]. Aragonite has a crystalline coordination number of 4, and the formation of aragonite would thus be favored at low pH-values if the averaged, dynamic coordination number x is considered. From the energetic point of view, the probability of the formation of less stable ionic arrangements becomes maximal at the minimum of binding energy, and the analysis of nucleated particles at this point (pH = 9.75, cp. Figure 5.23, section 5.2.4) is especially interesting and presented in this section.

Figure 5.29 shows SEM images of particles formed approximately 5.5 hours after nucleation at pH = 9.75. The excess crystal morphology observed corresponds to the typical morphology often found for vaterite, and is exemplary indicated by a green circle. Furthermore, typical calcite rhombohedra can be found, which are exemplary indicated by red circles.

[6] It has been shown that ACC contains one water molecule per calcium and carbonate ion, anhydrous ACC is only transient [23].

Occasionally, also needle shaped crystals -an often observed morphology of aragonite- can be found as indicated by blue circles.

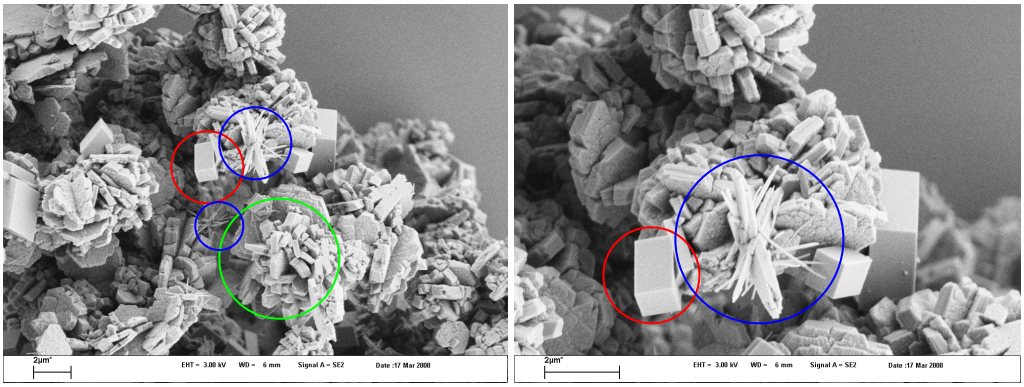

Figure 5.29: SEM images of calcium carbonate particles precipitated at pH = 9.75 approximately 5.5 hours after nucleation. Scale bar 2 microns. For explanations see text.

The WAXS diffractogram of a powder of the nucleated particles shown in Figure 5.29 is illustrated in Figure 5.30 compared to data base diffractograms of vaterite (green), calcite (red) and aragonite (blue), respectively. As already indicated by the observed morphologies, vaterite is the crystalline excess species. The two most intense peaks of calcite can be observed as indicated by red arrows reflecting a minor appearance of calcite. Aragonite cannot be detected clearly due to the overlap of strongest peaks with vaterite.

Light microscopy of the particles formed approximately 400 s after nucleation is presented in Figure 5.31 (left). The micron sized particles are clearly crystalline as indicated by their birefringence (Figure 5.31, right). Polarized light microscopy gives additionally a proof of the existence of smaller nanoparticles, because the shining particles show a caustic [58]. These nanoparticles can be considered to be partly the ACC species, which determines the solubility product (cp. Figure 5.26, section 5.2.5).

These nanoparticles are illustrated in TEM images of the precipitated particles approximately 700 seconds after the nucleation event as shown in Figure 5.32 (a.) (b.). Already in this early stage –the amount of calcium ions has not yet reached the value corresponding to the solubility concentration of nucleated ACC (cp. Figure 5.12)- precursors of vaterite and calcite crystals shown in Figure 5.29 can be found: Figure 5.32 (a.) shows particles of rhombohedral shape, while electron diffraction indicates calcite single crystals (right).

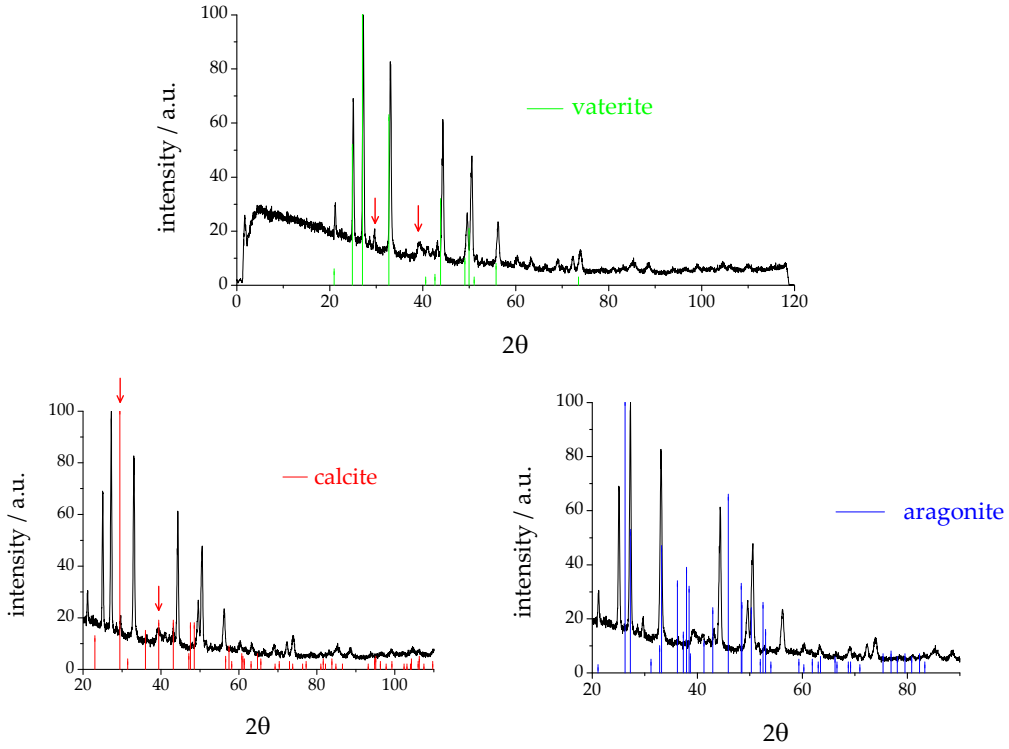

Figure 5.30: WAXS diffractogram of a powder of the nucleated particles illustrated in Figure 5.29 in comparison to data base diffractograms of vaterite (green), calcite (red) and aragonite (blue), respectively. All peaks are normalized to the most intense peak. For explanations see text.

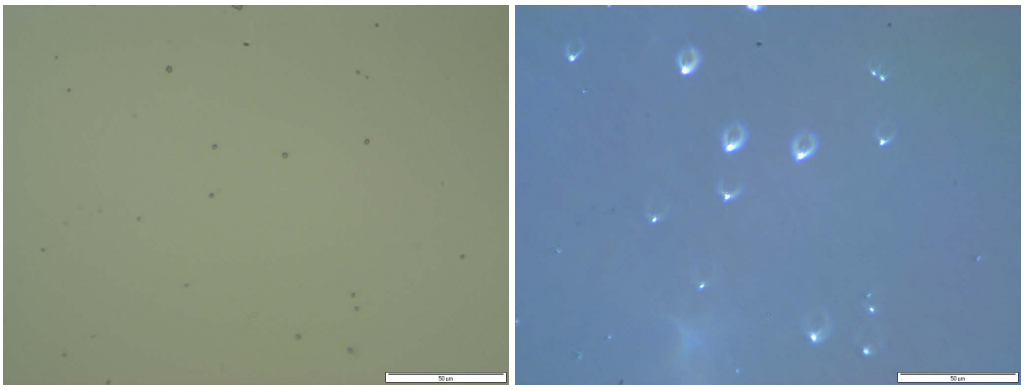

Figure 5.31: Light microscopy (left) and polarized light microscopy (right) images of particles formed approximately 400 s after the nucleation event at pH = 9.75. The micron-sized particles are birefringent, while the caustic around the shining birefringent particles is a sign of present nanoparticles [58]. Scale bar 50 microns.

The texture of the particles refers to density fluctuations, which indicate composition of nanoparticles that can be observed in the surrounding. Figure 5.32 (b.) shows a spherical particle. Again, the texture indicates that the particle is composed of nanoparticles, which

can be found in the surrounding. Despite of the spherical shape and obvious nanoparticles composition, the angular spread in the electron diffraction pattern is low and indicates a high mutual order of nano-crystallites as observed in mesocrystals [11]. The diffraction pattern indicates vaterite.

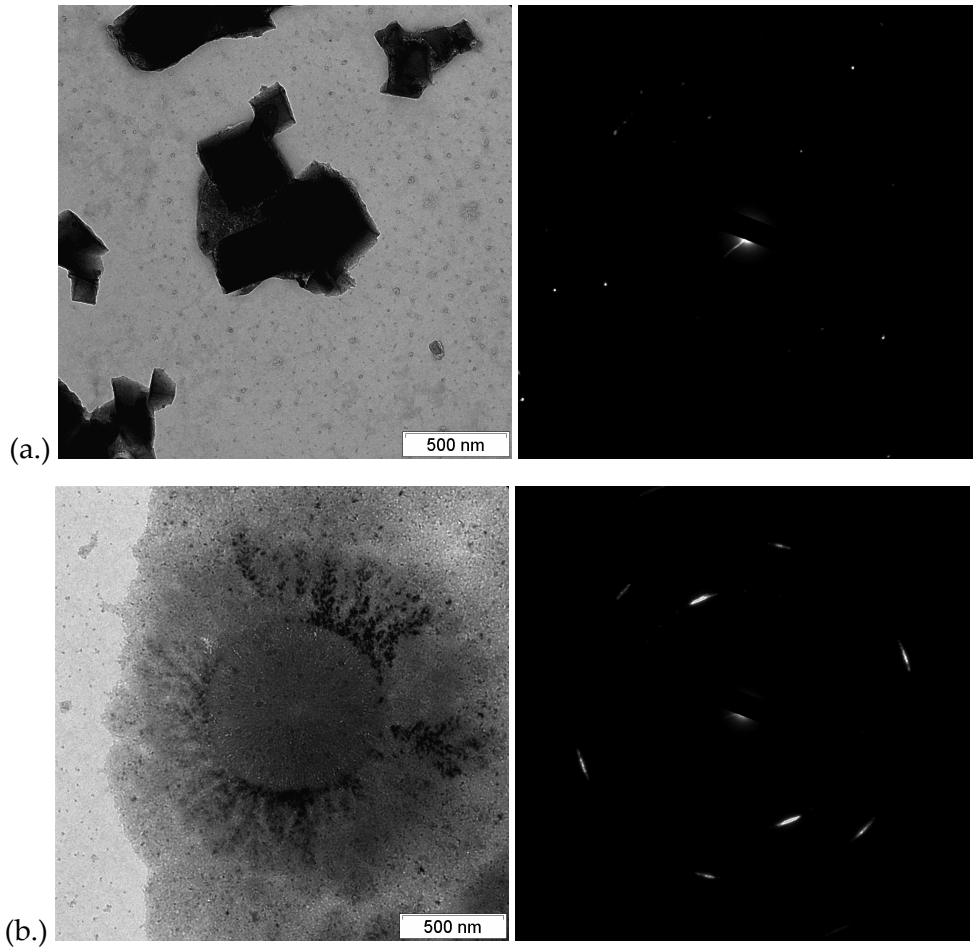

Figure 5.32: TEM images of particles approximately 700 s after nucleation. The texture indicates that the nucleated particles consist of nanoparticles visible in the surrounding area Additionally shown are electron diffraction patterns. The distances of diffraction spots from the center indicate calcite (a.) and vaterite (b.). For further explanations see text.

Crystallinity as indicated by the electron diffraction pattern is not induced by the electron beam, respectively, because crystallinity is independently detected by means of birefringence of the particles in solution, from which they were precipitated (Figure 5.31). It is exceedingly remarkable that the electron diffraction indicates the presence of a single crystal, respectively; it suggests that the nanoparticles in the particles are almost already perfectly aligned, i.e. the crystals shown are mesocrystals.

The nanoparticles, which can be found in the surrounding, show sizes of around 5 nm to 10 nm and are speculatively, partly amorphous calcium carbonate nanoparticles, which determine the solubility product discussed in section 5.2.5. The amorphous character cannot be proven at this point. Bigger particles are formed *via* agglomeration of crystalline nanoparticles of the same species, respectively.

Figure 5.33 shows TEM images of formed particles approximately 3200 seconds after the nucleation event. Predominantly, the spherical vaterite particles have grown, indicating that most of the present nanoparticles are vateritic. The texture of the bigger particles still clearly indicates that they are composed of nanoparticles. Electron diffraction of the big, spherical particles indicates vaterite crystals with high mutual order of nano-crystallites.

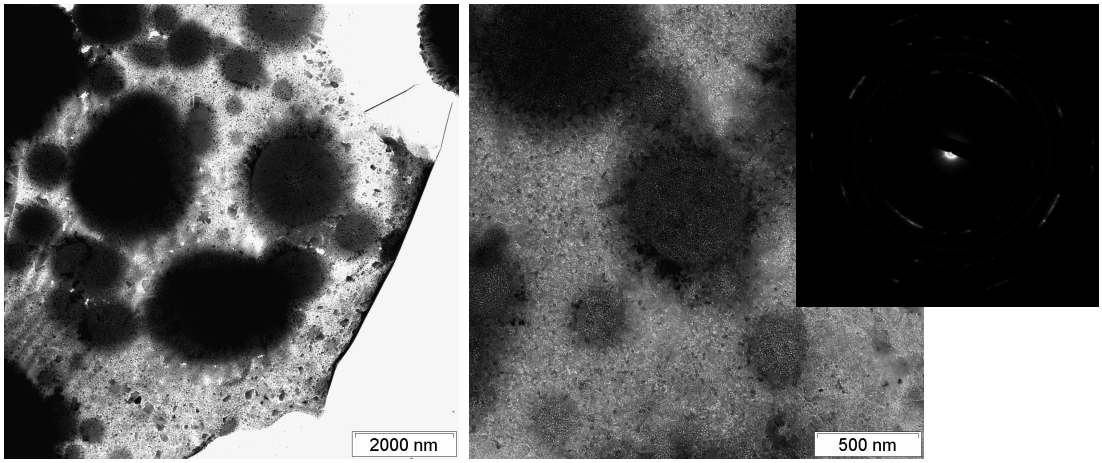

Figure 5.33: TEM images of particles approximately 3200 s after nucleation. The nanoparticles texture is still apparent, while electron diffraction indicates crystallinity with high mutual order of nano-crystallites. The distances of spots from the center indicate vaterite For further explanations see text.

Figure 5.34 shows TEM images of formed particles approximately 4900 seconds after the nucleation event. The number-density of surrounding nanoparticles has decreased remarkably, while the texture of the bigger particles is more even, i.e. the nanoparticles in the bigger particles begin to fuse indicated by a more constant particle density. Rhombohedral (red arrows) and also needle shaped (blue arrows) particles can be found. Figure 5.34 closes the circle to Figure 5.29, which shows SEM images of the particles 5.5 hours after nucleation; the particles have just grown. It is important to note that some details in shown TEM images may display artifacts, since samples were drawn from the beaker experiments at indicated times, put onto TEM grids and quickly dried in vacuum. However, the observation of three

calcium carbonate polymorphs at minimal cluster binding energy supports the speculated mechanism for the formation of different calcium carbonate polymorphs: As discussed in section 5.2.4, EXAFS studies reveal short range order of different ACC species, which transform into the particular long range order of the crystalline polymorph. The analysis of ion products as discussed in section 5.2.5 reveals the existence of at least two ACC species, which may correspond to calcitic and vateritic ACC. Proximately the change in the binding strength in clusters is the basis of the formation of the different ACC species at minimal binding strength. In reverse, the appearance of crystals showing typical morphology of aragonite suggests the existence of a third ACC species corresponding to aragonitic ACC. Particles of the particular polymorphs grow *via* agglomeration of only a single type of nanoparticles. This mechanism shows that all calcium carbonate single crystals arise from mesocrystals in the observed case, although no stabilizing additive is present.

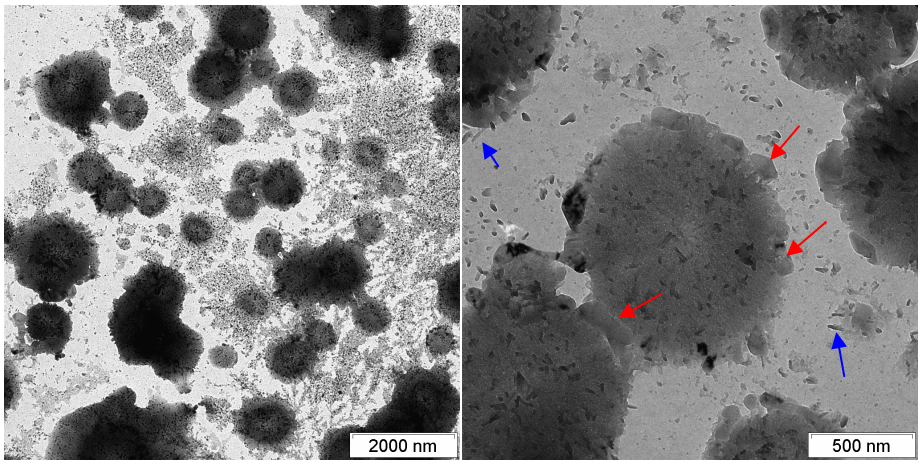

Figure 5.34: TEM images of particles approximately 4900 s after nucleation. The nanoparticles texture is reduced. Red arrows indicate calcitic rhombohedra, blue arrows indicate presumably aragonitic needles. For further explanations see text.

The analysis of calcium carbonate precipitation in presence of additives in the following section will give a proof for the parallel existence of different ACC species after nucleation and it will become evident that the pre-nucleation stage clusters are indeed the precursors of the nucleated ACC particles.

5.3 Calcium Carbonate Precipitation in Presence of Additives

Precipitation of calcium carbonate in presence of additives is studied at the minimum of cluster binding energy at pH = 9.75, because here, an influence of additives on pre-nucleation stage clusters can be expected to be maximal. In the following, the influence of two different types of additives is analyzed: Polyacrylic acid provides a model system for scale inhibitors, i.e. compounds which inhibit nucleation. Peptides provide a model system for compounds that modify crystals, i.e. morphology, polymorph, etc.

5.3.1 Polyacrylic Acid as a Model Compound for Scale Inhibition

As already indicated in section 1, scale formation causes enormous costs in private, public and commercial households, while the mechanism of scale formation is not understood.

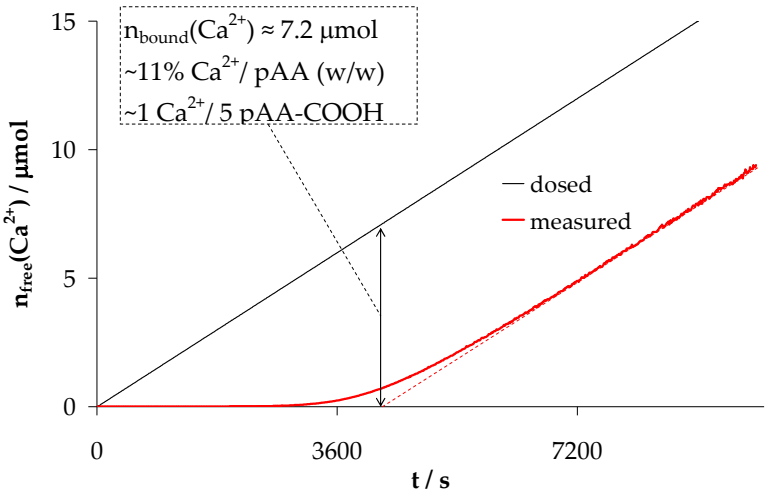

Figure 5.35: Calcium titration of 25 mL 0.1 g/L polyacrylic acid (pAA) solution in water at pH = 9.75. The binding capacity of polyacrylic acid is approximately 11% Ca^{2+}/pAA (w/w) relating to the adsorption of one calcium ion on 5 polymeric carbonic acid groups. For explanations see text.

Polycarboxylates like polyacrylic acid (pAA) or polyaspartic acid providing calcium ion binding capacity are added as scale inhibitors in laundry detergents, dishwashers, cooling circuits, etc. In this section, the action of pAA,

$$H_3C-HC(COOH)\left[-CH_2-HC(COOH)\right]_y-CH_2-H_2C(COOH),$$

as a model compound for scale inhibition is analyzed quantitatively.

The pAA utilized has an averaged molecular weight of 5100 g/mol, i.e. one molecule pAA provides approximately 71 carbonic acid groups. Figure 5.35 illustrates the calcium titration of a solution of 0.1 g/L pAA in pure water. The black line gives the added amount of calcium ions due to dosing and the red line gives the measured amount of calcium ions. The parallel offset of both time-developments is a dimension for the binding capacity of pAA for calcium ions of approximately 11% (w/w). This relates to the adsorption of 15 calcium ions *per* pAA molecule or the binding of one calcium ion to 5 polymeric carbonic acid groups. This binding capacity for free calcium ions is classically considered to be the reason for scale inhibition by pAA –besides growth inhibition of nucleated particles [29, 59]- because the free concentration of calcium ions is significantly lowered.

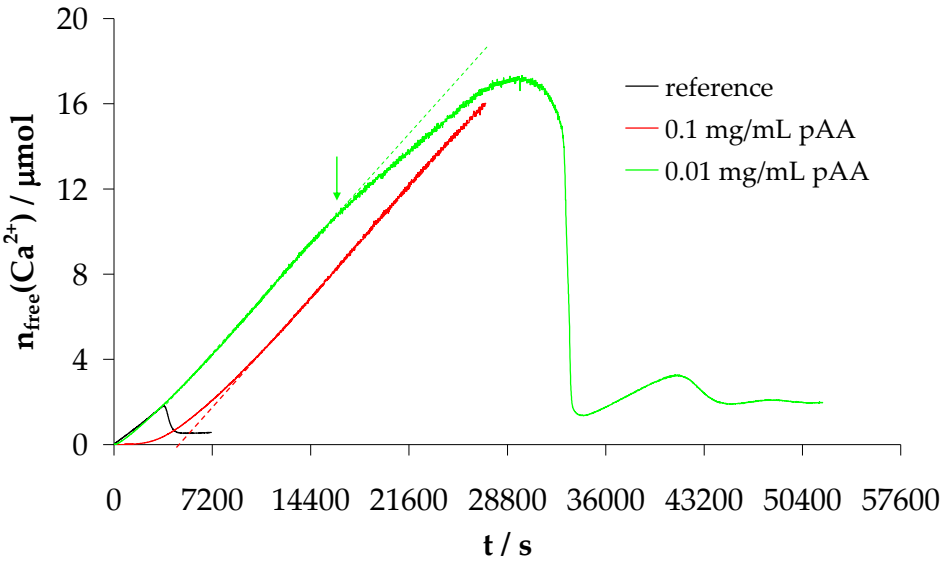

Figure 5.36: Time-development of the free amount of calcium ions in beaker experiments in absence of pAA (reference, cp. also Figure 5.12, black line) and in presence of 0.1 mg/mL polyacrylic acid (pAA, red line) and 0.01 mg/mL polyacrylic acid (pAA, green line). For explanations see text.

However, as obvious from Figure 5.36, the calcium ion binding capacity plays a secondary role in the inhibition of nucleation: Shown is the time-development of the free amount of calcium ions in beaker experiments. The black line gives the reference experiment in absence of pAA (cp. section 5.2.2, Figure 5.12). The red line represents an experiment in presence of 0.1 g/L pAA. In analogy to Figure 5.35, the time development shows the adsorption of calcium ions on the polymer, which sums up to approximately 4% (w/w) as shown in Figure

5.37 relating to the adsorption of one free calcium ion on 14 polymeric carbonic acid groups. This means that pAA can bind less free calcium ions in presence of clusters (cp. Figure 5.35), thus indicating that clusters are adsorbed on pAA. The nucleation is inhibited distinctly, while the experiment was aborted after 7.5 hours. In presence of 0.01 g/L pAA (green line), however, the adsorption of free calcium ions on the polymer is negligible as indicated by the minor offset. Anyhow, the nucleation is inhibited distinctly and takes place approximately 7 hours later than in absence of pAA. Thus, nucleation inhibition is due to the adsorption of the pre-nucleation stage clusters on pAA stabilizing the clusters against nucleation. The equilibrium of cluster formation stays unaffected by the polymer additive as indicated by an unvaried initial slope within experimental accuracy. Beyond, the initial slope is independent of the pAA concentration as indicated by the parallel offset in presence of 0.1 g/L pAA and 0.01 g/L pAA(cp. also Figure 5.37).

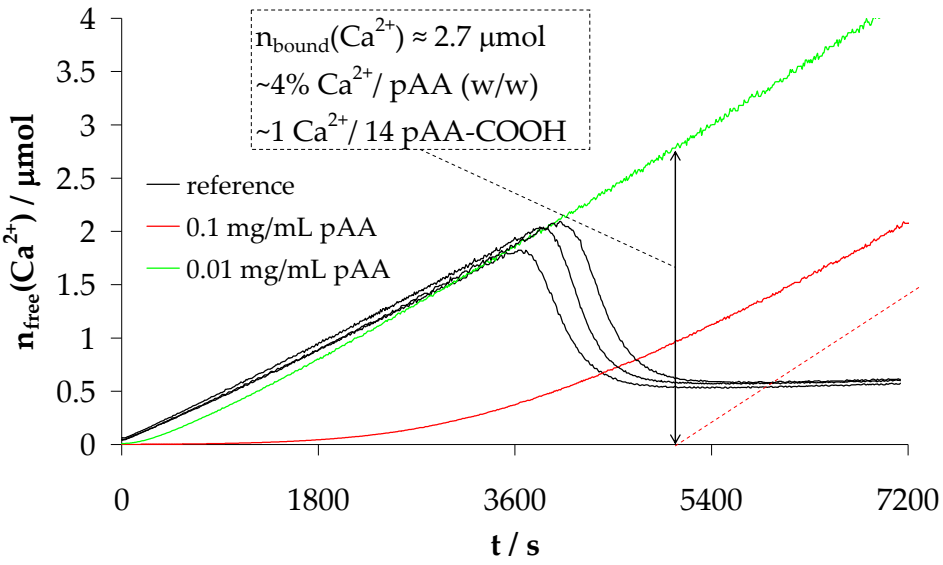

Figure 5.37: Zoom-in of Figure 5.36 clarifying negligible overall-adsorption of calcium ions in presence of 0.01 g/L pAA. The adsorption of free calcium ions is 4% (w/w) in presence of 0.1 g/L pAA relating to approximately 1 free calcium ion bound on 14 polymeric carbonic acid groups. For explanations see text.

An interesting effect in presence of 0.01 g/L pAA is the down-bending of the time-development of the free amount of calcium ions after approximately 4.5 hours as indicated by the green arrow in Figure 5.36. This means that an increased amount of calcium ions is bound, while the system is still stabilized against nucleation. It is proximate, that the

additional amount of ions is not bound in the clusters, because the cluster equilibrium is proven to stay unaffected at earlier times. A possible explanation is that the system is coming close to the spinodal. Here, the system is still metastable, while fluctuations towards the formation of the new phase occur. Such fluctuations are capable of binding additional mass, while the amplitude of the fluctuations coming closer to the spinodal increases and with it the capability of binding more and more mass. This might be indicated by the subsequent down-bending of the shown time-development. Finally, the spinodal is reached and by exceeding the spinodal point, the polymer is not capable of stabilizing the fluctuations of formally infinite amplitude, and spinodal decomposition occurs. This scenario is speculative and not proven at this point. No additional binding of calcium ions can be observed in presence of 0.1 g/L (red curve, Figure 5.36). In the just discussed scenario this would indicate that the spinodal point is influenced by the pAA concentration, which is called 'damping' of fluctuations by an amphiphilic additive.

The influence of pAA on the precipitation of calcium carbonate can be categorized by means of the time-development of the free amount of calcium ions as shown in Figure 5.36 and Figure 5.37.

- type I: adsorption of calcium ions,
- type II: influence on cluster equilibrium,
- type III: inhibition of nucleation due to adsorption of clusters,
- type IV: adsorption on nucleated particles and
- type V: any kind of influence on nucleated particles.

As discussed above, pAA is a type I/III additive. It will be shown in the following that pAA is actually a type I/III/IV/V additive.

A second interesting effect in presence of 0.01 g/L pAA is the new increase of the free amount of calcium ions after the first nucleation event, which tunes-out repeatedly. This effect can be ascribed to the adsorption of clusters (additive type III) and to the adsorption of nucleated particles (additive type IV) on pAA. After the first nucleation event, the due to the continuing addition of calcium ions newly forming clusters are adsorbed on pAA and thus inhibited from instant 'attachment' to the ACC particles formed, which are also adsorbed to pAA [29, 59]. The slope of the new increase is thus flatter than the initial increase, because the clusters still attach to the present ACC particles but at a distinctly reduced rate. Due to less 'free' pAA in the system, a new nucleation is inhibited distinctly shorter. This process

then repeatedly takes place indicating that pAA adsorbed to clusters is partly released due to nucleation, which is obvious from reducing the adsorption surface.

The precipitated particles yielded approximately 6 hours after the first nucleation event in presence of 0.01 g/L pAA are illustrated in Figure 5.38. The SEM images show distinctly different morphologies than obtained in absence of pAA (type V, cp. also Figure 5.29). On one hand, the particles are distinctly smaller than particles formed 5.5 hours after the nucleation event in absence of pAA. This indicates that the particles are formed suddenly and uniformly supporting the speculative formation *via* spinodal decomposition.

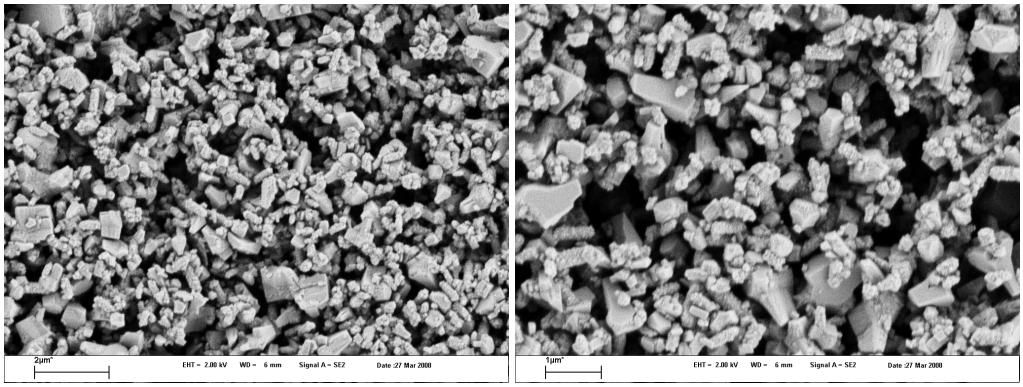

Figure 5.38: SEM images of particles precipitated approximately 6 hours after the first nucleation event at pH = 9.75 in presence of 0.01 g/L pAA. Scale bar 2 microns (left) and 1 micron (right). For explanations see text.

On the other hand, the typical vateritic, spherical morphology is not obtained at all. The particle morphology rather relates to calcitic rhombohedra disturbed in growth. The WAXS diffractogram of the particles is shown in Figure 5.39 and indicates pure calcite. The peaks marked by black arrows relate neither to vaterite nor to aragonite. Most proximately, these peaks can be attributed to traces of calcite monohydrate (data base data not shown, see also section 5.3.2). The formation of pure calcite approximately 6 hours after nucleation in presence of pAA is remarkable, since almost pure vaterite with only traces of calcite and presumably aragonite is precipitated 5.5 hours after nucleation at pH = 9.75 in absence of pAA (cp. section 5.2.7).

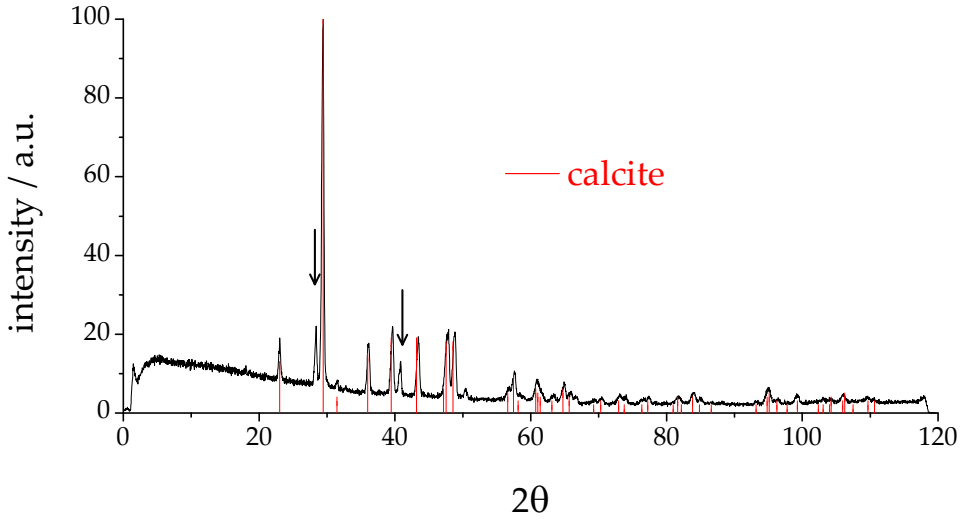

Figure 5.39: WAXS diffractogram of particles precipitated at pH = 9.75 in presence of 0.01 g/L pAA (cp. Figure 5.38) in comparison to a data base calcite diffractogram. The peaks indicated by black arrows correspond neither to vaterite nor to aragonite. Arrows mark peaks, which may relate to traces of calcite monohydrate. For further explanations see text.

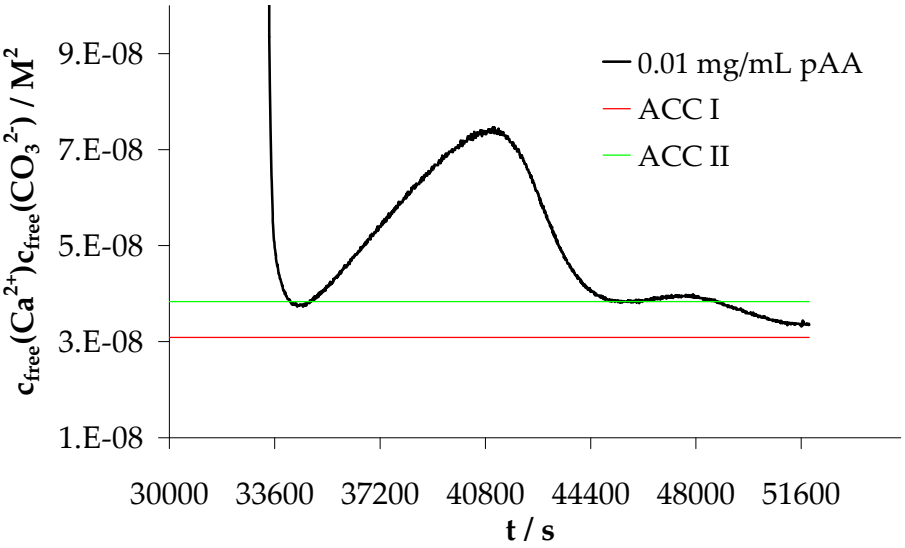

Figure 5.40: Time development of the free ion product in presence of 0.01 g/L pAA after the first nucleation event (cp. Figure 5.36). The solubility products correspond to ACC I (green) and ACC II (red) as determined in section 5.2.5 (cp. Figure 5.26). For explanations see text.

Figure 5.40 illustrates the time-development of the ion product after the first nucleation event at pH = 9.75 in presence of 0.01 g/L pAA. After the first and second nucleation event,

the solubility product drops approximately to the value corresponding to the solubility of ACC II, which is formed in absence of pAA and transforms into vaterite (cp. section 5.2.5, Figure 5.26). However, after the third detectable nucleation event, the solubility product drops to the value corresponding to the solubility product of ACC I, which is otherwise only observed at lower pH-values, at which calcite is formed. At first, this means that no ACC II is present 6 hours after the nucleation event, while it was present before. Since exclusively calcite is detected by WAXS, ACC II has not transformed into vaterite but has dissolved completely for the benefit of ACC I, which transforms into calcite. This process can be understood as OSTWALD ripening on the basis of amorphous precursor species, which takes place only in presence of pAA. Without pAA, both polymorphs can be detected in the time interval from shortly after the nucleation event until 5.5 hours after nucleation. This indicates that OSTWALD ripening for the benefit of calcite in absence of pAA takes place at much longer timescales on the basis of already crystalline particles. In reverse, this indicates that pAA adsorbs preferentially both vateritic clusters and vateritic ACC. The preferential adsorption of vateritic clusters is the basis of the inhibition of nucleation (type III), while the preferential adsorption of precipitated vateritic ACC (type IV) stabilizes this ACC species against crystallization and agglomeration and thus causes its dissolution in presence of other already crystalline species. In this regard, Type V is a direct consequence of type III and type IV preferential for one species. The polymorph switch from predominant vaterite to exclusive calcite (type V) in presence of pAA is thus caused by preferential adsorption of vateritic clusters and vateritic ACC (type III/IV) inhibiting the formation of vateritic crystallites. This might indicate that a polymorph switch can be achieved by adsorption of the particular other amorphous precursor species, respectively, stabilizing them against crystallization and favouring their dissolution. This scenario will become evident to a greater extent in the following section.

5.3.2 Peptides as Model Compounds for Modifiers

There is a huge, almost unmanageable amount of scientific literature dealing with the investigation of the action of additives on crystallization. 'Additives' are designated compounds, which are not essentially part of the resulting crystal but can be incorporated into the crystal lattice, while they show more or less distinct influence on the formed crystalline structures. Additive compounds can be ions, small molecules or polymers. An

especially interesting group of additives are biopolymers (or biomimetic polymers), which are considered to play important roles in biomineralization, see e.g. [60-72].

The peptides analyzed in this thesis are 12-mers described in [73] exhibiting binding affinity to geological aragonite crystals as derived in a phage assay. The sequences according to the one-character-code of amino acids are

IHIKFKQHQNHN (peptide 1),

KRSKFPHKHDVI (peptide 2) and

AVGSTKHKWPPL (peptide 3).

The peptides were analyzed in gas diffusion experiments (cp. section 4.3), which facilitate precipitation of calcium carbonate at increasing pH-values starting at approximately pH = 5-6 and precipitating calcium carbonate at approximately pH = 8.5-9.

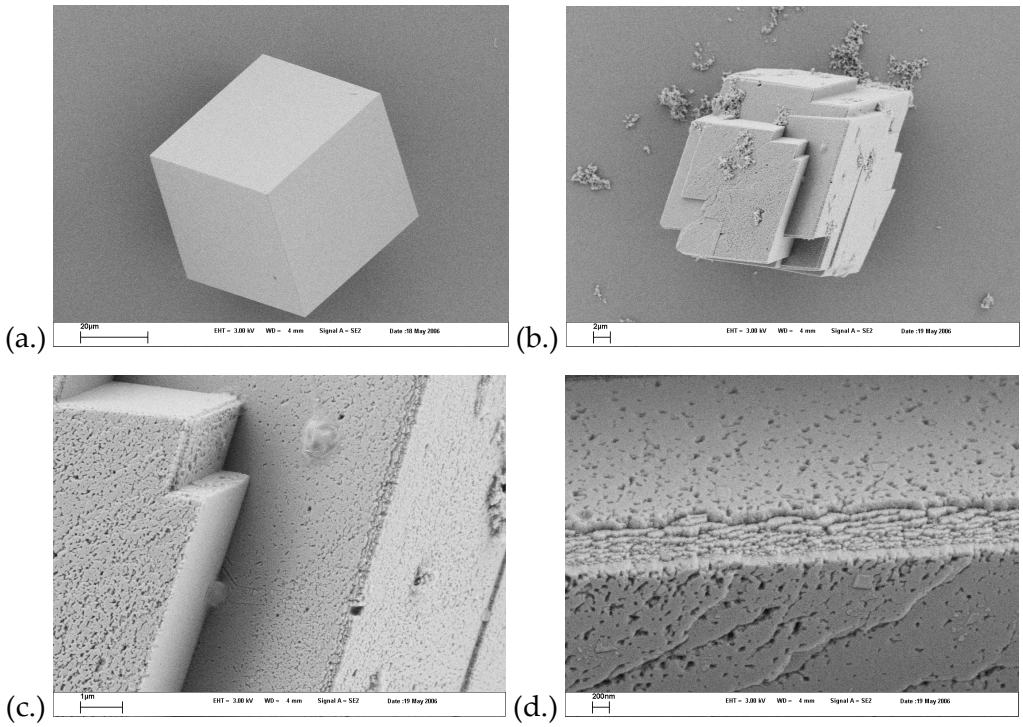

Figure 5.41: SEM images of crystals precipitated in gas diffusion experiments. (a.) Typical calcite rhombohedron precipitated in absence of additives. (b.) – (d.) Calcite crystals precipitated in presence of $1 \cdot 10^{-3}$ M KRSKFPHKHDVI (peptide 2), cp. also Figure 5.42. Scale bar: (a.) 20 microns, (b.) 2 microns, (c.) 1 micron, (d.) 200 nm. For explanations see text.

Thus, this experiment is to produce calcite rhombohedra (cp. section 5.2.4), while peptides were applied with a concentration of $1 \cdot 10^{-3}$ M.

Peptides 1 and 3 do not show any distinct effect on calcium carbonate crystals in gas-diffusion experiments, while peptide 2 causes growth inhibition expressed by developed edges, dislocations and pores (Figure 5.41 (b.) to (d.)) indicating that the peptide adsorbs on (104) faces. The result is very similar to literature results obtained with two different, highly conserved subdomains of the protein family Asprich associated with the prismatic layer of the bivalve *Atrina rigida* as illustrated in Figure 5.42 (results taken from [71]). The subdomains are in the one-character-code of amino acids

DEADEADADEADADEAD (DEAD17) and

ADNDAAETDAADVGTEAEDVADDE (Acidic-2).

Both subdomains are considered to play important roles in biomineralization processes in the calcitic layer of the bivalve by the inhibition of the growth of calcite. In this regard, it is proximate that peptide 2 inhibits calcite growth, too.

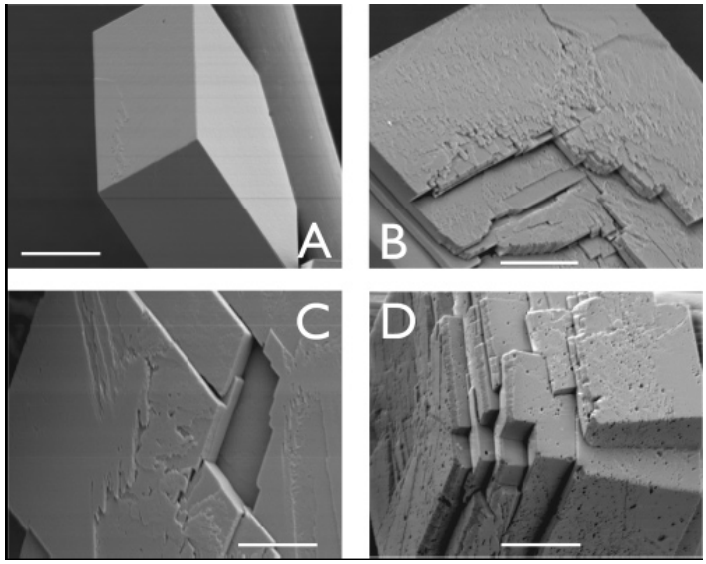

Figure 5.42: SEM images taken from [71]. A: Negative Control featuring typical rhombohedral calcite crystals. B: Crystals grown in presence of DEAD17 subdomain. C: Crystals grown in presence of acidic-2 subdomain. D: Crystals grown in presence of acidic-2-DEAD17 subdomain. Scalebar = 5 μm. For explanations see text.

The influence of the three aragonite binding peptides on the nucleation of calcium carbonate is quantitatively studied at the minimum of binding energy in clusters at pH = 9.75, because

here, the action of additives can be expected to be maximal. Figure 5.43 illustrates the time-development of the free amount of calcium ions for a sample of three reference experiments without additive (cp. also Figure 5.12) and two time-developments, respectively in presence of 0.01 g/L of the particular peptides.

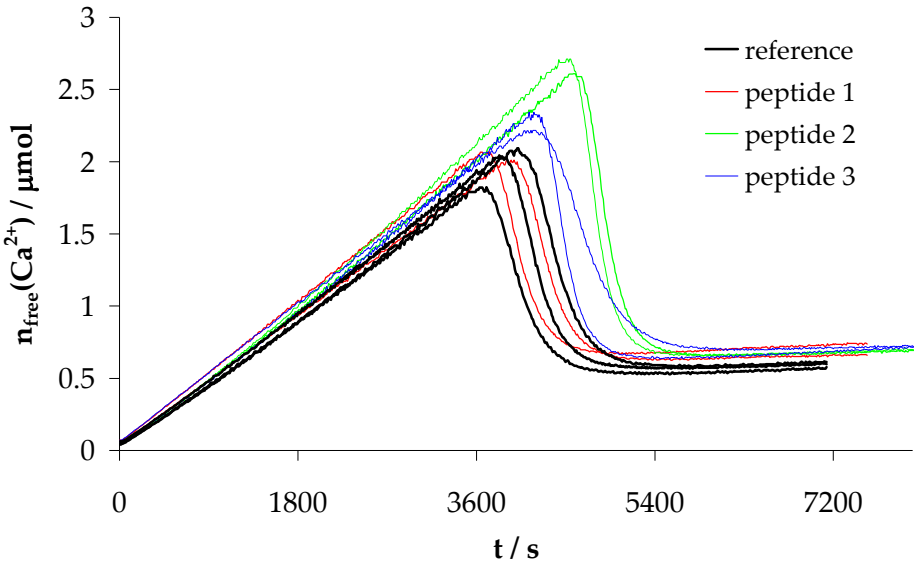

Figure 5.43: Time development of the free amount of calcium ions at pH = 9.75 (cp. also Figure 5.12). 'Reference' indicates the time-development in absence of additives, 'IHIKFKQHQNHN' as indicated peptide 1, 'KRSKFPHKHDVI' as indicated peptide 2 and 'AVGSTKHKWPPL' as indicated peptide 3 at a concentration of 0.01 g/L, respectively. For explanations see text.

It is obvious that the peptides do not bind calcium ions at the applied concentrations, i.e. the peptides are not type I additives (cp. section 5.3.1). The peptides do not change the cluster equilibrium since the pre-nucleation stage slopes are congruent within experimental accuracy: The minor initial slope offset correlates the offset of the amount of calcium ions that corresponds to the solubility concentration of vateritic ACC. This minor offset is probably due to the small peptides affecting the ion exchanger properties of the ion selective membrane. The peptides are neither type II additives (cp. section 5.3.1), therefore. In fact, there is an influence on the time of nucleation (type III, cp. section 5.3.1): Peptide 2 inhibits nucleation for approximately 600 s; peptide 3 just possibly inhibits nucleation for an interval smaller than 300 s, while nucleation inhibition is not detectable at all for peptide 1. This finding directly correlates the effect of the peptides in the gas-diffusion experiment discussed

above, i.e. nucleation inhibition results in a visible effect on the crystal shape while no nucleation inhibition means any visible effect on the crystal shape.

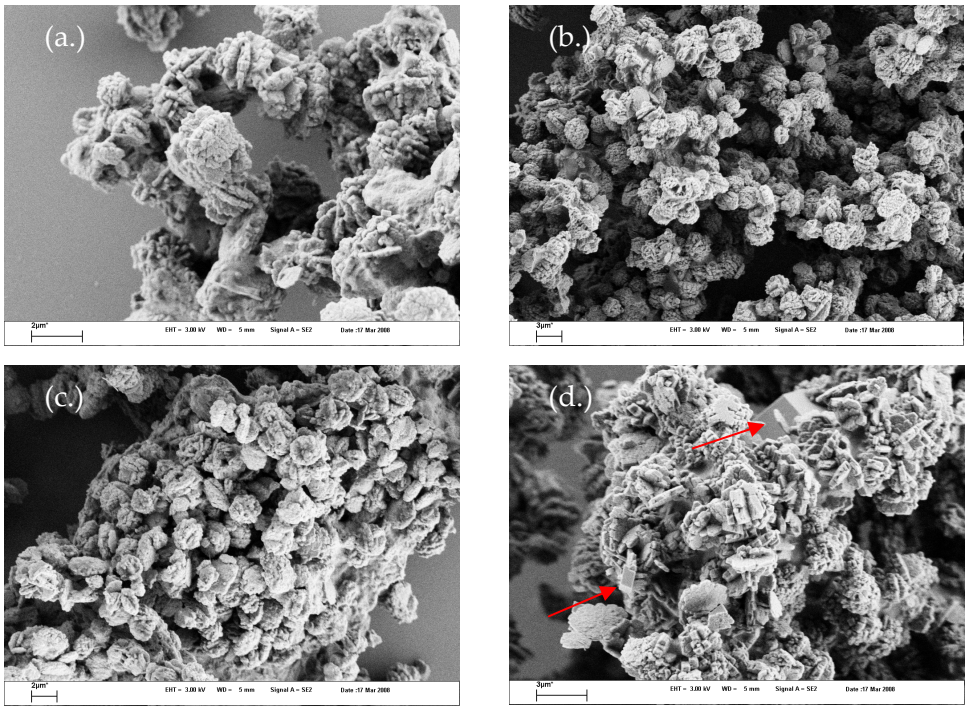

Figure 5.44: Calcium carbonate particles nucleated in presence of 0.01 g/L (a.), (b.) peptide 2 with nucleation inhibition, (c.) peptide 1 with minor nucleation inhibition and (d.) peptide 3 without nucleation inhibition. For explanations see text.

The precipitated particles in presence of peptide additives are shown in Figure 5.44. In comparison to the reference (cp. Figure 5.29), the particles are clotted with peptides, while the predominant vaterite crystals show presumably the same shape. However, it is peculiar that in presence of peptide additives (Figure 5.44 (a.) to (c.)), which inhibit nucleation, no calcite rhombohedra can be found. In presence of peptide 3 (Figure 5.44 (d.)), which shows no nucleation inhibition, the calcite rhombohedra can be found as indicated by red arrows. The adsorption on nucleated particles as well as any kind of influence on nucleated particles of peptide 2 and 3 is proximate (type IV/V, cp. section 5.3.1). Figure 5.45 illustrates a section of the WAXS diffractogram of particles precipitated in presence of peptide 1 (black) in comparison to the WAXS diffractogram of particles precipitated in absence of additives (cyan) and of particles precipitated in presence of 0.01 g/L pAA (red). Additionally given are data base diffraction patterns of calcite and vaterite (red and green columns). The peaks in

presence of peptide 1 and in absence of additives can be assigned to vaterite and the peaks in presence of pAA can be assigned to calcite.

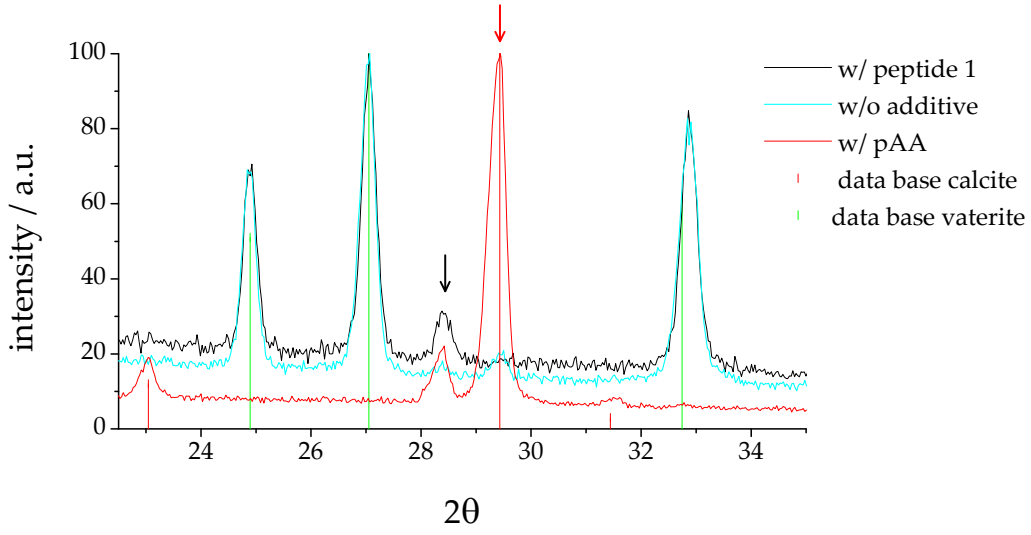

Figure 5.45: WAXS diffractograms of crystal powders of precipitated particles in presence of peptide 1 (black), without additive (cyan) and in presence of 0.01 g/L pAA (red, cp. Figure 5.39) in comparison to data base diffraction patterns of calcite (red column) and vaterite (green column). The red arrow indicates the most intense calcite peak, the black arrow marks the peak, which may relate to calcium carbonate monohydrate. For explanations see text.

The calcite peak indicated by a red arrow occurs also in absence of additives and refers to the minor trace of calcite as already discussed in section 5.2.7, while it does not occur in presence of peptide 1. However, the peak indicated by a black arrow, which is already discussed in section 5.3.1, occurs in presence of peptide 1 and in presence of pAA. As already discussed, this peak might correspond to calcite monohydrate. The calcite rhombohedra shown in Figure 5.44 may thus form out of calcite monohydrate due to the removal of crystal-water in SEM high vacuum or represent calcite monohydrate morphology.

Figure 5.46 illustrates the same sections of WAXS diffractograms of powders of the particles precipitated in presence of peptide 1 (red), peptide 2 (green) and peptide 3 (blue). The most intense calcite peak (position indicated by red arrow) does not occur at all, while the peak that may relate to calcite monohydrate (black arrow) is detectable in presence of peptide 1, hardly detectable in presence of peptide 2 and not detectable in presence of peptide 3. This is in good agreement with the crystal morphologies illustrated in Figure 5.44, where calcite

(possibly calcite monohydrate-) rhombohedra, can be found in presence of peptide 1 but hardly in presence of peptides 2 and 3. This finding indicates that all three peptides are type IV additives (cp. section 5.3.1), i.e. they adsorb on nucleated calcitic ACC (they exhibit calcite binding affinity beyond their aragonite binding affinity, see above). This is obvious for peptide 1 and 2 due to the inhibition of calcite formation. It is obvious for peptide 3 because it inhibits the formation of calcite crystals and additionally the formation of calcite monohydrate.

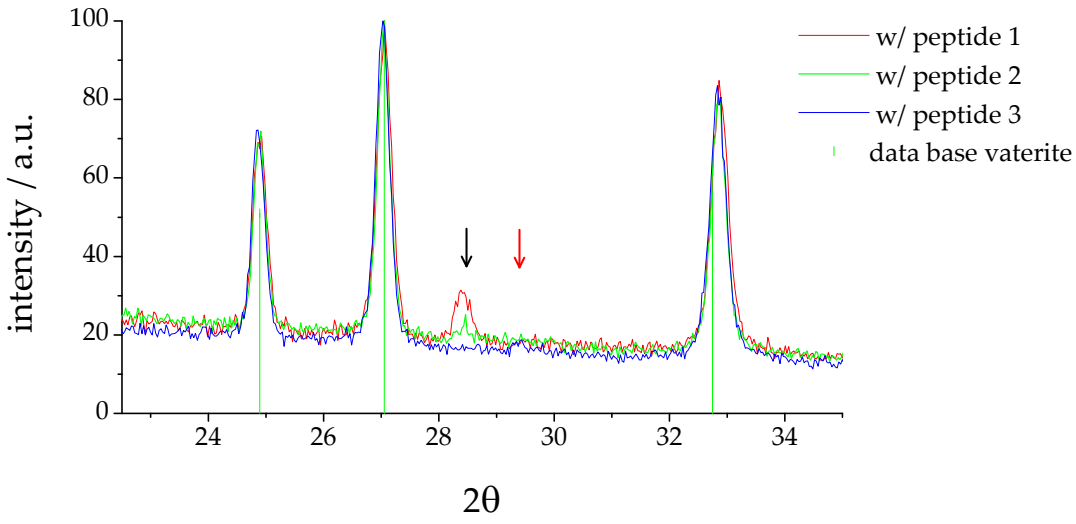

Figure 5.46: WAXS diffractograms of a powder of precipitated particles in presence of peptide 1 (red, cp. Figure 5.45), peptide 2 (green) and peptide 3 (blue). The red arrow indicates the position of the most intense calcite peak and the black arrow indicates the peak, which may relate to calcite monohydrate (cp. also Figure 5.45). For further explanations see text.

In analogy to the discussion of the action of pAA (cp. section 5.3.1), the peptides are capable of binding calcitic clusters and calcitic ACC, stabilizing calcitic ACC against crystallization into calcite (but possibly calcite monohydrate can be formed) and in this way leading to its dissolution. The consequence is that no calcite is obtained (type V additives, cp. section 5.3.1), while peptide 2 is better capable of stabilizing the clusters against nucleation. Furthermore, peptide 1 is proximately adsorbed on nucleated particles but is not capable of inhibiting nucleation. The analysis shows that peptide 1 is a type IV/V, peptide 2 and 3 type III/IV/V additives (cp. section 5.3.1), while the three types can be considered to be independent. One type does not essentially require another except for type V, which bases

on the adsorption of clusters and/or nucleated particles. Peptides 1 and 2 may not show any influence in gas-diffusion experiments because here, the binding strength in clusters is strong.

5.4 Inconsistencies with Classical Nucleation Theory

As already stated in section 5.2.6, pre-nucleation stage cluster formation can be described by equilibrium thermodynamics and is not a purely stochastical process as considered in CNT. This section points out further inconsistencies between CNT and the experimental findings. In CNT, the quantity defining the driving force of phase transition is the supersaturation ratio

$$s = \frac{\left|c_{free}(Ca^{2+}_{aq.})c_{free}(CO^{2-}_{3,aq.})\right|_{solution}}{\left|c_{free}(Ca^{2+}_{aq.})c_{free}(CO^{2-}_{3,aq.})\right|_{ACC}},$$

where $\left|c_{free}(Ca^{2+}_{aq.})c_{free}(CO^{2-}_{3,aq.})\right|_{solution}$ is the free ion product of the particular supersaturated solution and $\left|c_{free}(Ca^{2+}_{aq.})c_{free}(CO^{2-}_{3,aq.})\right|_{ACC}$ is the free ion product in presence of the particular ACC species (cp. also section 5.2.5). However, as shown above, different ACC species may be nucleated in parallel, whereas the solubility product in presence of the different species is determined by the least stable species, i.e. the driving force for the formation of the more stable ACC species is underestimated. On the other hand, the ion product of the prenucleation stage includes the formation of clusters. Thus, in this regard, the concept of the supersaturation ratio as a dimension defining the driving force of phase transition is critical. Figure 5.47 illustrates the time-development of the supersaturation ratio taking cluster formation into account (bold lines) and neglecting cluster formation (fine lines). At pH = 10.0 and pH = 9.75, the supersaturation ratio is calculated on the basis of ACC II, while the supersaturation ratio at pH = 9.50 to pH = 9.00 is calculated on the basis of ACC I. Here, neglecting of cluster formation is analogous to an experiment, where the supersaturation ratio is not measured but calculated from weighted-in ion concentrations. The aberrations are distinct as indicated, respectively, and correlate the percentage of bound amounts of ions as illustrated in Figure 5.13. A straightforward analysis according to equation (2.4) using the supersaturation ratio at the time of nucleation gives the change of GIBBS energy due to phase

transition as listed in Table 5.1. The values demonstrate that the system is stabilized remarkably due to cluster formation at all pH-values, respectively.

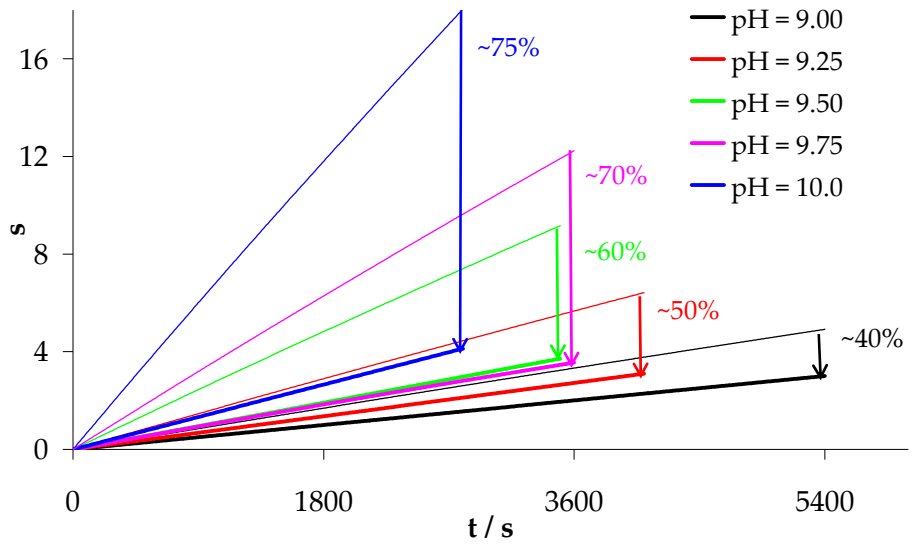

Figure 5.47: Time development of the supersaturation ratio calculated by measured free ion products (taking cluster formation into account, bold lines) and by weighed-in free ion products (neglecting cluster formation, fine lines). The indicated, distinct aberration correlates the percentage of ions bound in clusters as illustrated in Figure 5.13. For further explanations see text.

The clustering phenomenon may be attributed to entropy gain due to the release of water molecules out of hydration layers. This effect can be simplified as

$$\begin{aligned} & N\left\{Ca^{2+}\cdot\left|H_2O\right|_w\right\} + N\left\{CO_3^{2-}\cdot\left|H_2O\right|_x\right\} \\ & \rightleftharpoons \left\{\left(CaCO_3\right)_N\cdot\left|H_2O\right|_y\right\} + z\cdot H_2O \quad , \\ & \text{with } 2\cdot N \ll z \end{aligned} \tag{5.19}$$

where $\left\{X\cdot\left|H_2O\right|_{w/x/y}\right\}$ designates the hydrated species, respectively. Cluster formation may generate an increased number of degrees of freedom as expressed by the higher number of molecules on the right side of equilibrium (5.19). In this regard, the minimum of binding strength (cp. section 5.2.4) may be attributed to a pH-dependent change of ionic hydration layers and may be in the end an entropic effect, too.

The presented concept of pre-nucleation cluster formation is most likely a common phenomenon for the precipitation of hardly soluble, ionic compounds. Figure 5.48 illustrates

the time development of the free amount of calcium ions in 10 mM phosphate buffer and 1 mM oxalate at pH = 8.0, respectively[7]. In both cases, a considerable amount of calcium ions is bound in clusters in complete analogy to the calcium carbonate example (cp. Figure 5.12).

	$\Delta_R G_{p.t.}$ / kJ·mol^{-1}, cp. equation (2.4)	
pH	w/ cluster formation	w/o cluster formation
9.00	-2.7	-3.9
9.25	-2.8	-4.6
9.50	-3.3	-5.5
9.75	-3.6	-6.2
10.0	-4.1	-7.2

Table 5.1: Classically calculated change in GIBBS energy due to phase transition taking cluster formation into account and neglecting cluster formation at the investigated pH-values, respectively. For explanations see text.

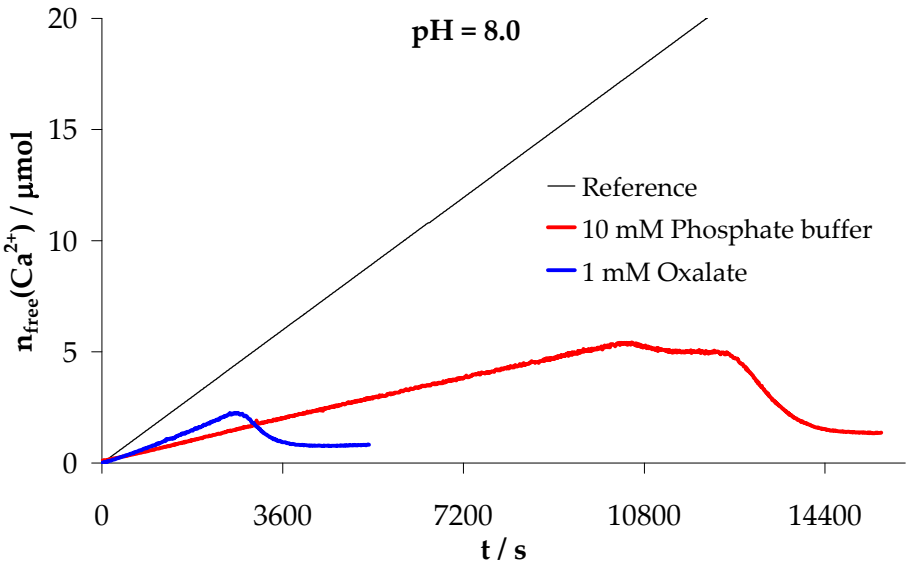

Figure 5.48: Time development of the free amount of calcium ions in 10 mM phosphate buffer (red) and 1 mM oxalate (blue) at pH = 8.0, respectively. The black line (reference) gives the amount of calcium ions that is added by dosing. A considerable amount of ions is bound in clusters, respectively (cp. also Figure 5.12): For further explanations see text.

[7] The time-development in phosphate buffer shows two successive nucleation events, which probably refer to the more complicated calcium phosphate phase diagram with numerous polymorphs.

6 Conclusion and Outlook

The quantitative analysis of calcium carbonate precipitation shows that pre-nucleation stage clusters form by means of equilibrium thermodynamics and not just on basis of stochastical fluctuations as considered in classical nucleation theory. Furthermore, the determined average cluster size –determined by means of Analytical Ultracentrifugation independently proving the existence of clusters- is bigger than one would expect on basis of classical considerations. Indeed, a novel species has been discovered, which can be considered to be the earliest species, which occurs during calcium carbonate precipitation. The system is stabilized remarkably by cluster formation, i.e. the driving force of phase transformation is reduced in comparison to classical considerations. The clustering phenomenon may be due to entropy gain caused by release of water molecules out of ionic hydration layers.

A speculative and simplified mechanism of calcium carbonate precipitation in absence of additives is illustrated in Figure 6.1. Prenucleation stage clusters form by means of equilibrium thermodynamics. The size distribution of the clusters is currently unknown. Likely, various different short range orders can be formed, which might locally differ in single clusters. The average short range order distribution depends on the pH-value by the binding strength in clusters, i.e. calcitic short range order dominates at high binding strength and other short range orders become probable at low binding strength. How many different structures can form and if these can be clearly distinguished yet is unknown. As the free amount of calcium ions is found to be low in comparison to the ions bound in clusters prior to nucleation, and the adsorption of polymers is capable of stabilizing the system against nucleation, the nucleation event may be caused by a critical cluster concentration, which leads to aggregation of clusters forming amorphous precursors of the new phase. Depending on the dominating short range order in a particular amorphous precursor particle, which is proximately the basis of the detection of two solubility products of precipitated ACC and which has been already discussed in the literature, or on basis of a random nucleation event, the amorphous precursors crystallize forming a (nano)-crystallite of the particular polymorph. These crystallites aggregate and align forming early crystals, which can be considered to be mesocrystals showing high mutual order of crystallites. In a last step, the crystallites of the early crystals may fuse forming the late crystals, which can subsequently

re-crystallize along the OSTWALD rule of stages. Ripening along OSTWALD's rule of stages may not distinctly occur in the early stages, because the process could be considered to be fast enough to be under kinetic control.

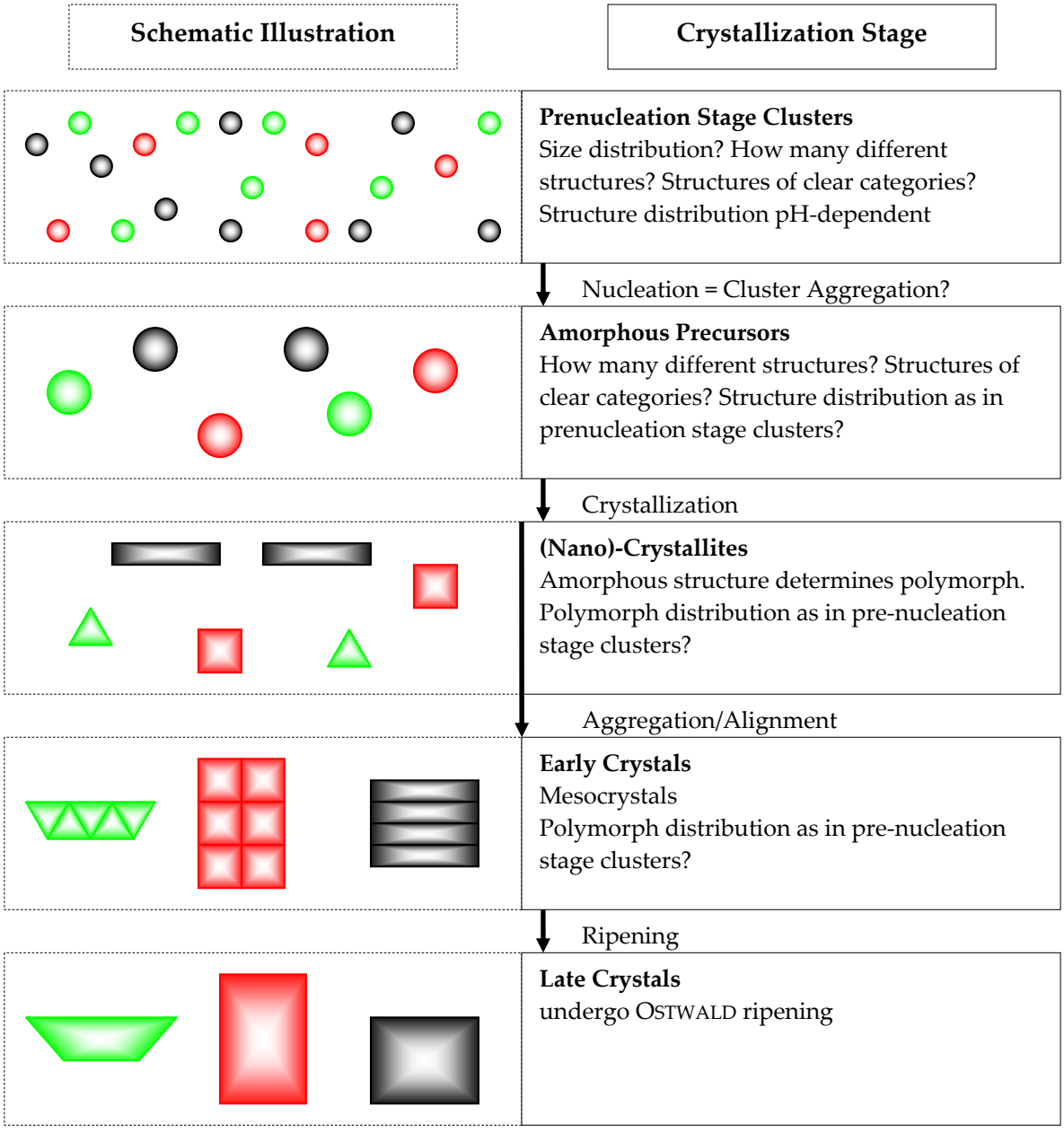

Figure 6.1: Speculative, simplified mechanism of calcium carbonate precipitation in absence of additives. Single ions are left out for the purpose of clarity. For explanations see text.

This speculative mechanism can explain the impact of additives on calcium carbonate crystallization. Additives can act already in the pre-nucleation stage by adsorption of ions and clusters. The adsorption stabilizes the system against nucleation, i.e. against aggregation

of clusters. Here, the additives may preferentially adsorb certain structures, and preferential adsorption would lead to a minor aggregation (nucleation) of these structures. Additives can be adsorbed on nucleated amorphous precursor particles stabilizing them against crystallization. Such stabilization can overcome the kinetic control along OSTWALD's rule of stages and the particularly stabilized amorphous precursor would dissolve for the benefit of nucleation of crystallites of the polymorph corresponding to those ACC precursors, which are less stabilized against nucleation. Additive adsorption may subsequently stabilize the primary mesocrystals against crystallite fusion.

The pre-nucleation stage cluster formation has been qualitatively shown for calcium phosphate and calcium oxalate as further important Biominerals, too, and thus can be considered to be a common phenomenon occurring during the precipitation of sparingly soluble crystalline compounds. This finding is important for the fundamental understanding of crystallization and nucleation-inhibition and modification by additives with impact on materials of huge scientific and industrial importance as well as for better understanding of the mass transport in crystallization. It can provide a novel basis for simulation and modelling approaches. New mechanisms of scale formation in Bio- and Geomineralization and also in scale inhibition on the basis of the newly reported reaction channel need to be considered. Concerning Biomineralization, also the mechanism of polymorph selection may be more common, which is yet not proven but plausible on the basis of experimental results of this work.

The developed experimental procedure allows the quantitative analysis of different precursor species and of the action of additives on the particular precursor species. It is now possible to quantitatively describe the action of additives. It can be shown, in which stage of precipitation the additives act and different actions on the precipitation can be detected. Strong influence on pre-nucleation clusters as detected by the distinct inhibition of nucleation by pAA leads to a strong influence on precipitated particles obvious from the polymorph switch from vaterite, which is predominantly formed in absence of additives, to pure calcite. However, the rather weak influence of peptide additives on pre-nucleation stage clusters leads to a minor effect on precipitated particles –pure vaterite lacking calcite traces is finally obtained. This regard is peculiar and it is proximate to speculate that nucleation inhibition bases on specific adsorption of pre-nucleation stage clusters, i.e. pAA could be less

capable of nucleation inhibition at lower pH-values (where calcite is formed anyway), while the peptide additives could be better capable of nucleation inhibition at lower pH-values. This will become more evident by means of future experiments. Concurrently, the amount and types of future experiments cannot be completely specified: The newly found cluster-precursor species has to be characterized better. The physicochemical characterization yet provides a major step, while the structure should be studied in more detail. EXAFS studies as applied in the literature for the analysis of different ACC species cannot be utilized since they require a dry sample. However, it may be possible to obtain different ACC species, which can be analyzed utilizing EXAFS. The characterization of pre-nucleation stage clusters could be facilitated by cryo-HRTEM, which could give information on particular cluster sizes and structures. The quantitative analyses of the action of numerous additives, which are already known to facilitate mesocrystal formation or polymorph switch, etc., are other interesting series of experiments. It is now quantitatively possible to relate the additive-action to the additive concentration, which is known to have a distinct influence, as well as to other experimental variables.

The discussed mechanism is a major progress in understanding the nucleation of the calcium carbonate system [74]. Neutral clusters –not ions- are the interacting species with additives that control and/or inhibit the formation of later precursor phases (ACC or PILP), the formation of polymorphs and crystal morphology and even of mesocrystals. Moreover, the pH-dependent binding strength of ions in clusters offers multiple new possibilities for additive controlled crystallization and scale inhibition. It also affects the CO_2 binding in the carbon cycle and with it the world climate, which is a topic of great current importance and attention. Much more CO_2 is bound in carbonate than can be assumed from the solid $CaCO_3$ sediments and therefore, the ocean chemistry (here pH-value) is of greater importance than assumed so far.

7 Abstract

This thesis provides a novel view on the early stage of crystallization utilizing calcium carbonate as a model system. Calcium carbonate is of great economical, scientific and ecological importance, because it is a major part of water hardness, the most abundant Biomineral and forms huge amounts of geological sediments thus binding large amounts of carbon dioxide.

The primary experiments base on the evolution of supersaturation *via* slow addition of dilute calcium chloride solution into dilute carbonate buffer. The time-dependent measurement of the Ca^{2+} potential and concurrent pH = constant titration facilitate the calculation of the amount of calcium and carbonate ions bound in pre-nucleation stage clusters, which have never been detected experimentally so far, and in the new phase after nucleation, respectively. Analytical Ultracentrifugation independently proves the existence of pre-nucleation stage clusters, and shows that the clusters forming at pH = 9.00 have a proximately time-averaged size of altogether 70 calcium and carbonate ions. Both experiments show that pre-nucleation stage cluster formation can be described by means of equilibrium thermodynamics. Effectively, the cluster formation equilibrium is physico-chemically characterized by means of a multiple-binding equilibrium of calcium ions to a 'lattice' of carbonate ions. The evaluation gives GIBBS standard energy for the formation of calcium/carbonate ion pairs in clusters, which exhibits a maximal value of approximately -17.2 kJ mol^{-1} at pH = 9.75 and relates to a minimal binding strength in clusters at this pH-value.

Nucleated calcium carbonate particles are amorphous at first and subsequently become crystalline. At high binding strength in clusters, only calcite (the thermodynamically stable polymorph) is finally obtained, while with decreasing binding strength in clusters, vaterite (the thermodynamically least stable polymorph) and presumably aragonite (the thermodynamically intermediate stable polymorph) are obtained additionally. Concurrently, two different solubility products of nucleated amorphous calcium carbonate (ACC) are detected at low binding strength and high binding strength in clusters (ACC I $3.1 \cdot 10^{-8}$ M^2, ACC II $3.8 \cdot 10^{-8}$ M^2), respectively, indicating the precipitation of at least two different ACC species, while the clusters provide the precursor species of ACC. It is proximate that ACC I

may relate to calcitic ACC[8] –i.e. ACC exhibiting short range order similar to the long range order of calcite- and that ACC II may relate to vateritic ACC, which will subsequently transform into the particular crystalline polymorph, respectively. Detailed analysis of nucleated particles forming at minimal binding strength in clusters (pH = 9.75) by means of SEM, TEM, WAXS and light microscopy shows that predominantly vaterite with traces of calcite forms. The crystalline particles of early stages are composed of nano-crystallites of approximately 5-10 nm size, respectively, which are aligned in high mutual order as in mesocrystals. The analyses of precipitation at pH = 9.75 in presence of additives –polyacrylic acid (pAA) as a model compound for scale inhibitors and peptides exhibiting calcium carbonate binding affinity as model compounds for crystal modifiers- shows that ACC I and ACC II are precipitated in parallel: pAA stabilizes ACC II particles against crystallization leading to their dissolution for the benefit of crystals that form from ACC I and exclusively calcite is finally obtained. Concurrently, the peptide additives analogously inhibit the formation of calcite and exclusively vaterite is finally obtained in case of one of the peptide additives.

Moreover, the action of additives can be categorized into at least five different types: (I) calcium ion binding capacity (pAA), (II) impact on pre-nucleation stage cluster equilibrium (not observed), (III) adsorption of pre-nucleation stage clusters causing nucleation inhibition (pAA, two of three peptides), (IV) adsorption of nucleated particles (pAA, three peptides) and (V) any resulting influence on nucleated particles (pAA, three peptides). The influence of additives on nucleated particles bases on one or more of the other types and includes the formation/stabilization of mesocrystals, impact on crystal morphologies (pAA) and polymorph switch (pAA, peptides, see above).

These findings show that classical nucleation theory is hardly applicable for the nucleation of calcium carbonate. The metastable system is stabilized remarkably due to cluster formation, while clusters forming by means of equilibrium thermodynamics are the nucleation relevant species and not ions. Most likely, the concept of cluster formation is a common phenomenon occurring during the precipitation of hardly soluble compounds as qualitatively shown for

[8] Different types of short range orders occurring in ACC have been already discussed in the literature.

calcium oxalate and calcium phosphate. This finding is important for the fundamental understanding of crystallization and nucleation-inhibition and modification by additives with impact on materials of huge scientific and industrial importance as well as for better understanding of the mass transport in crystallization. It can provide a novel basis for simulation and modelling approaches. New mechanisms of scale formation in Bio- and Geomineralization and also in scale inhibition on the basis of the newly reported reaction channel need to be considered.

8 Kurzfassung

Die vorliegende Arbeit zeichnet ein neuartiges Bild der frühen Kristallisationsphase von Calciumcarbonat. Calciumcarbonat hat als Hauptbestandteil der Wasserhärte und als weit verbreitetes Biomineral und Geomineral, das als Sediment in den Ozeanen große Mengen Kohlendioxid bindet, große Bedeutung. Die grundlegenden Experimente basieren auf der sehr langsamen Einstellung von Übersättigung, die durch langsame Zugabe verdünnter Calciumlösung in verdünnten Carbonatpuffer erreicht wird. Zeitabhängige Messung des Ca^{2+} Potentials bei gleichzeitiger pH = konstant Titration zeigt, dass zeitgemittelt vor der Nukleation gleiche Stoffmengen von Calcium- und Carbonat Ionen in Clustern gebunden sind, die bis jetzt noch nicht experimentell nachgewiesen werden konnten. Analytische Ultrazentrifugation belegt unabhängig die Existenz der Cluster, und es zeigt sich, dass sich die bei pH = 9,00 bildenden Cluster zeitgemittelt aus insgesamt etwa 70 Calcium und Carbonat Ionen bestehen. Die Experimente weisen darauf hin, dass sich die Clusterbildung auf der Grundlage von Gleichgewichtsthermodynamik beschreiben lässt. Ein multiples Bindungsgleichgewichtsmodell ermöglicht die Bestimmung der freien Standard Reaktionsenthalpie für die Bildung von Calcium/Carbonat Ionenpaaren in den Clustern, die ein Maß für die Bindungsstärke in Clustern darstellt. Die Bindungsstärke weist ein Minimum bei pH = 9,75 ($\Delta_R G^{\otimes}_{\text{ion pair}} \cong -17,2$ kJ mol^{-1}) auf, und es zeigt sich, dass außerhalb dieses Minimums amorphes Calciumcarbonat ausfällt, das sich letztendlich in Calcit (das thermodynamisch stabile Calciumcarbonat Polymorph) umwandelt, während im Minimum und in der Nähe des Minimums amorphes Calciumcarbonat ausfällt, das sich letztendlich hauptsächlich in Vaterit (das thermodynamisch am wenigsten stabile Polymorph), Calcit und möglicherweise Spuren von Aragonit (das Polymorph mittlerer Stabilität) umwandelt. Gleichzeitig treten zwei unterschiedliche Löslichkeitsprodukte für das bei hoher und niedriger Bindungsstärke in Clustern ausgefällte, amorphe Calciumcarbonat auf (ACC I $3,1 \cdot 10^{-8}$ M^2, ACC II $3,8 \cdot 10^{-8}$ M^2). Das zeigt, dass die sich vor der Nukleation bildenden Cluster Vorläuferspezies (Precursor) des ausgefällten, amorphen Calciumcarbonats darstellen, wobei ACC I in der Literatur diskutiertem, calcitischem ACC entsprechen und ACC II vateritischem Calcit entsprechen kann. Eine detaillierte SEM, TEM, WAXS und Lichtmikroskopie Untersuchung der bei minimaler Bindungsstärke in Clustern (pH = 9,75)

ausgefällten Partikel zeigt, dass sich hauptsächlich Vaterit mit Spuren von Calcit und möglicherweise Aragonit bildet. Die sich früh bildenden, kristallinen Partikel sind jeweils aus nano-Kristalliten von etwa 5 -10 nm Größe aufgebaut, die wie in Mesokristallen eine hohe wechselseitige Ordnung aufweisen.

Die Untersuchung der frühen Kristallisation in Gegenwart von Additiven wurde ebenfalls bei minimaler Bindungsstärke in Clustern durchgeführt. Als Additive wurden Polyacrylsäure (PAA) als Beispiel für einen Hemmstoff gegen die Bildung von Verkalkungen und drei Peptide, die Bindungsaffinität zu Calciumcarbonat zeigen, als Beispiel für Kristallisations-Modifikatoren untersucht. Die Analyse zeigt, dass ACC I und ACC II parallel ausfallen; pAA stabilisiert ACC II gegenüber Kristallisation und führt dazu, dass es sich zugunsten von Kristallen, die sich aus ACC I bilden, auflöst, wobei letztendlich reines Calcit erhalten wird. Die Peptide hingegen hemmen die Bildung von Calcit in analoger Weise, wobei in einem Fall letztendlich reines Vaterit entsteht.

Weiterhin kann die Wirkungsweise von Additiven in mindestens fünf Kategorien unterteilt werden: (I) Adsorption von Calcium Ionen (PAA), (II) Auswirkung auf das Cluster-gleichgewicht (nicht beobachtet), (III) Adsorption der Cluster, die zur Hemmung der Nukleation führt (PAA, zwei der drei untersuchten Peptide), (IV) Adsorption ausgefällter Partikel (PAA, Peptide) und (V) jeglicher Einfluss auf ausgefällte Partikel (PAA, Peptide). Der Einfluss eines Additivs auf ausgefällte Partikel basiert auf mindestens einer der anderen Kategorien und beinhaltet die Bildung, bzw. Stabilisierung von Mesokristallen, Wirkung auf Kristallmorphologien (PAA) oder den Einfluss auf gebildete Polymorphe (PAA, Peptide, s. o.).

Die Ergebnisse zeigen, dass die klassische Nukleationstheorie auf die Nukleation von Calciumcarbonat kaum anwendbar ist. Das metastabile System wird durch die Clusterbildung deutlich stabilisiert, und nicht Ionen, sondern Cluster sind die relevanten Spezies in der Nukleation. Wahrscheinlich ist das gefundene Konzept der Clusterbildung ein allgemeines Phänomen, das während der Kristallisation aller schwer löslichen Substanzen auftritt, da es auch für Calciumoxalat und Calciumphosphat qualitativ gezeigt werden konnte. Das Ergebnis ist wichtig für das fundamentale Verständnis der Nukleation, von Nukleationshemmung und der Modifikation von Kristallen mit Auswirkungen auf Materialen von großer industrieller und auch wissenschaftlicher Bedeutung. Ferner gibt es einen Hinweis, wie Masse während der Kristallisation –auch in Lebewesen- transportiert

werden kann und es kann einen neuen Ansatz für Kristallisationssimulationen liefern. Auf der Basis dieses neuartigen Reaktionskanals müssen neue Kristallisations-Mechanismen in Bio- und Geomineralization in Betracht gezogen werden.

9 References

1. Available from: http://commons.wikimedia.org/wiki/Image:Kesselstein_k.jpg.
2. Available from: http://commons.wikimedia.org/wiki/Image:Protein_crystals_grown_in_space.jpg.
3. Available from: http://www.planktonworld.com/.
4. Mullin, J.W., *Crystallization*. 4th ed. 2001, Woburn, MA: Butterworth-Heinemann.
5. Volmer, M., *Kinetik der Phasenbildung*. 1939, Dresden: Steinkopff.
6. Knezic, D., J. Zaccaro, and A.S. Myerson, *Nucleation induction time in levitated droplets.* Journal of Physical Chemistry B, 2004. **108**(30): p. 10672-10677.
7. Izmailov, A.F., A.S. Myerson, and S. Arnold, *A statistical understanding of nucleation.* Journal of Crystal Growth, 1999. **196**(2-4): p. 234-242.
8. Becker, R. and W. Döring, *Kinetic treatment of germ formation in supersaturated vapour.* Annalen Der Physik, 1935. **24**(8): p. 719-752.
9. De Yoreo, J.J., Vekilov, P. G., *Principles of crystal nucleation and growth.* Reviews in Mineralogy & Geochemistry, 2003. **54 (Biomineralization)**: p. 57-93.
10. Niederberger, M. and H. Cölfen, *Oriented attachment and mesocrystals: Non-classical crystallization mechanisms based on nanoparticle assembly.* Physical Chemistry Chemical Physics, 2006. **8**(28): p. 3271-3287.
11. Cölfen, H. and M. Antonietti, *Mesocrystals and Non Classical Crystallization*. 2008, Weinheim: Wiley.
12. Cölfen, H. and M. Antonietti, *Mesocrystals: Inorganic superstructures made by highly parallel crystallization and controlled alignment.* Angewandte Chemie-International Edition, 2005. **44**(35): p. 5576-5591.
13. Mann, S., *Biomineralization, Principles and Concepts in Bioinorganic Materials Chemistry*. 2001, Oxford: Oxford University Press.
14. Lowenstam, H.A. and S. Weiner, *On Biomineralization*. 1989, New York: Oxford University Press.
15. Bäuerlein, W., ed. *Biomineralization, Progress in Biology, Molecular Biology and Application*. 2nd completely revised and extended ed. 2004, Wiley-VCH: Weinheim.
16. Yu, S.H., H. Cölfen, K. Tauer, and M. Antonietti, *Tectonic arrangement of BaCO3 nanocrystals into helices induced by a racemic block copolymer.* Nature Materials, 2005. **4**(1): p. 51-U5.
17. Marsh, M.E., in *Biomineralization, Progress in Biology, Molecular Biology and Application* W. Bäuerlein, Editor. 2004, Wiley-VCH: Weinheim. p. 197.
18. Politi, Y., T. Arad, E. Klein, S. Weiner, and L. Addadi, *Sea urchin spine calcite forms via a transient amorphous calcium carbonate phase.* Science, 2004. **306**(5699): p. 1161-1164.

19. Gehrke, N., *Retrosynthese von Perlmutt*, in *Max-Planck-Institute of Colloids and Interfaces*. 2006, Universität Potsdam: Potsdam.
20. Kulak, A.N., P. Iddon, Y.T. Li, S.P. Armes, H. Cölfen, O. Paris, R.M. Wilson, and F.C. Meldrum, *Continuous structural evolution of calcium carbonate particles: A unifying model of copolymer-mediated crystallization.* Journal of the American Chemical Society, 2007. **129**(12): p. 3729-3736.
21. Horn, D. and J. Rieger, *Organic nanoparticles in the aqueous phase - theory, experiment, and use.* Angewandte Chemie-International Edition, 2001. **40**(23): p. 4331-4361.
22. Müller-Steinhagen, H. and Q. Zhao, *Investigation of low fouling surface alloys made by ion implantation technology.* Chemical Engineering Science, 1997. **52**(19): p. 3321-3332.
23. Addadi, L., S. Raz, and S. Weiner, *Taking advantage of disorder: Amorphous calcium carbonate and its roles in biomineralization.* Advanced Materials, 2003. **15**(12): p. 959-970.
24. Xu, A.W., Y.R. Ma, and H. Cölfen, *Biomimetic mineralization.* Journal of Materials Chemistry, 2007. **17**(5): p. 415-449.
25. Gower, L.B. and D.J. Odom, *Deposition of calcium carbonate films by a polymer-induced liquid-precursor (PILP) process.* Journal of Crystal Growth, 2000. **210**(4): p. 719-734.
26. Sinn, C.G., R. Dimova, and M. Antonietti, *Isothermal titration calorimetry of the polyelectrolyte/water interaction and binding of Ca2+: Effects determining the quality of polymeric scale inhibitors.* Macromolecules, 2004. **37**(9): p. 3444-3450.
27. Pontoni, D., J. Bolze, N. Dingenouts, T. Narayanan, and M. Ballauff, *Crystallization of calcium carbonate observed in-situ by combined small- and wide-angle X-ray scattering.* Journal of Physical Chemistry B, 2003. **107**(22): p. 5123-5125.
28. Bolze, J., D. Pontoni, M. Ballauff, T. Narayanan, and H. Cölfen, *Time-resolved SAXS study of the effect of a double hydrophilic block-copolymer on the formation of CaCO3 from a supersaturated salt solution.* Journal of Colloid and Interface Science, 2004. **277**(1): p. 84-94.
29. Rieger, J., *A new approach towards an understanding of scaling in the presence of polycarboxylates.* Tenside Surfactants Detergents, 2002. **39**(6): p. 221-225.
30. Navrotsky, A., *Energetic clues to pathways to biomineralization: Precursors, clusters, and nanoparticles.* Proceedings of the National Academy of Sciences of the United States of America, 2004. **101**(33): p. 12096-12101.
31. Perry, C.C., *Silicification: The processes by which organisms capture and mineralize silica*, in *Biomineralization*. 2003. p. 291-327.
32. Furrer, G., B.L. Phillips, K.U. Ulrich, R. Pothig, and W.H. Casey, *The origin of aluminum flocs in polluted streams.* Science, 2002. **297**(5590): p. 2245-2247.
33. Casey, W.H. and T.W. Swaddle, *Why small? The use of small inorganic clusters to understand mineral surface and dissolution reactions in geochemistry.* Reviews of Geophysics, 2003. **41**(2).

34. Larson, M.A. and J. Garside, *Solute Clustering in Supersaturated Solutions.* Chemical Engineering Science, 1986. **41**(5): p. 1285-1289.
35. Kashchiev, D., *Nucleation, Basic Theory with Applications*. Vol. 1. 2000, Oxford: Butterworth-Heinemann.
36. Farkas, L., *The speed of germinitive formation in over saturated vapours.* Zeitschrift Für Physikalische Chemie--Stöchiometrie Und Verwandtschaftslehre, 1927. **125**(3/4): p. 236-242.
37. Reiss, H., J.L. Katz, and E.R. Cohen, *Translation-Rotation Paradox in Theory of Nucleation.* Journal of Chemical Physics, 1968. **48**(12): p. 5553-&.
38. Zettlemoyer, A.C., ed. *Nucleation*. 1969, Dekker: New York. 109.
39. Nadykto, A.B. and F. Yu, *Simple correction to the classical theory of homogeneous nucleation.* Journal of Chemical Physics, 2005. **122**(10).
40. Oxtoby, D.W. and R. Evans, *Nonclassical Nucleation Theory for the Gas-Liquid Transistion.* Journal of Chemical Physics, 1988. **89**(12): p. 7521-7530.
41. Cahn, J.W. and J.E. Hilliard, *Free energy of a nonuniform system- 1. Interfacial free energy.* Journal of Chemical Physics, 1958. **28**(2): p. 258-267.
42. Kelton, K.F., *Crystal nucleation in liquids and glasses.* Solid State Physics-Advances in Research and Applications, 1991. **45**: p. 75-177.
43. Laaksonen, A., V. Talanquer, and D.W. Oxtoby, *Nucleation - Measurements, Theory and Atmospheric Applications.* Annual Review of Physical Chemistry, 1995. **46**: p. 489-524.
44. Oxtoby, D.W., *Homogeneous Nucleation - Theory and Experiment.* Journal of Physics-Condensed Matter, 1992. **4**(38): p. 7627-7650.
45. J. H. Seinfeld, S.P., *Atmospheric Chemistry and Physics: From Air Pollution to Climate Change*. 1998, New York: Wiley.
46. Schuck, P., *Size-distribution analysis of macromolecules by sedimentation velocity ultracentrifugation and Lamm equation modelling.* Biophysical Journal, 2000. **78**(3): p. 1606-1619.
47. Available from: http://www.analyticalultracentrifugation.com.
48. Neira C, A., M.S. Fernandez, J. Retuert, and J.L. Arias, *Effect of the crystallization chamber design on the polymorphs of calcium carbonate using the sitting-drop method.* Materials Research Society Symposium Proceedings, 2004. **EXS-1(Architecture and Application of Biomaterials and Biomolecular Materials)**: p. 321-326.
49. Carpino, L.A., A. Elfaham, C.A. Minor, and F. Albericio, *Advantageous applications of azabenzotriazole (triazolopyridine)-based coupling reagents to solid-phase peptide-synthesis.* Journal of the Chemical Society-Chemical Communications, 1994(2): p. 201-203.
50. Chan, W.C. and P.D. White, eds. *Fmoc Solid Phase Peptide Synthesis: A Practical Approach*. 2000, Oxford University Press: New York.
51. Lide, D.R., ed. *Handbook of Chemistry and Physics*. 75th ed. 1994, CRC Press: Boca Raton.

52. Hasse, B., H. Ehrenberg, J.C. Marxen, W. Becker, and M. Epple, *Calcium carbonate modifications in the mineralized shell of the freshwater snail Biomphalaria glabrata.* Chemistry-a European Journal, 2000. **6**(20): p. 3679-3685.
53. Lam, R.S.K., J.M. Charnock, A. Lennie, and F.C. Meldrum, *Synthesis-dependant structural variations in amorphous calcium carbonate.* Crystengcomm, 2007. **9**(12): p. 1226-1236.
54. Politi, Y., Y. Levi-Kalisman, S. Raz, F. Wilt, L. Addadi, S. Weiner, and I. Sagi, *Structural characterization of the transient amorphous calcium carbonate precursor phase in sea urchin embryos.* Advanced Functional Materials, 2006. **16**(10): p. 1289-1298.
55. Brecevic, L. and A.E. Nielsen, *Solubility of amorphous calcium-carbonate.* Journal of Crystal Growth, 1989. **98**(3): p. 504-510.
56. Coelfen, H. and A. Voelkel, *Application of the density variation method on calcium carbonate nanoparticles.* Progress in Colloid and Polymer Science, 2006. **131**: p. 126-128.
57. Available from: http://www.mindat.org/min-859.html.
58. Tyrrell, J. *Optical microscope tracks nanoparticles*. 2008 Available from: http://nanotechweb.org/cws/article/tech/33406.
59. Rieger, J., T. Frechen, G. Cox, W. Heckmann, C. Schmidt, and J. Thieme, *Precursor structures in the crystallization/precipitation processes of CaCO3 and control of particle formation by polyelectrolytes.* Faraday Discussions, 2007. **136**: p. 265-277.
60. Weiss, I.M., S. Kaufmann, K. Mann, and M. Fritz, *Purification and characterization of perlucin and perlustrin, two new proteins from the shell of the mollusc Haliotis laevigata.* Biochemical and Biophysical Research Communications, 2000. **267**(1): p. 17-21.
61. Sollner, C., M. Burghammer, E. Busch-Nentwich, J. Berger, H. Schwarz, C. Riekel, and T. Nicolson, *Control of crystal size and lattice formation by starmaker in otolith biomineralization.* Science, 2003. **302**(5643): p. 282-286.
62. Pokroy, B., E. Zolotoyabko, and N. Adir, *Purification and functional analysis of a 40 kD protein extracted from the Strombus decorus persicus mollusk shells.* Biomacromolecules, 2006. **7**(2): p. 550-556.
63. Michenfelder, M., G. Fu, C. Lawrence, J.C. Weaver, B.A. Wustman, L. Taranto, J.S. Evans, and D.E. Morse, *Characterization of two molluscan crystal-modulating biomineralization proteins and identification of putative mineral binding domains.* Biopolymers, 2004. **73**(2): p. 291-291.
64. Levi, Y., S. Albeck, A. Brack, S. Weiner, and L. Addadi, *Control over aragonite crystal nucleation and growth: An in vitro study of biomineralization.* Chemistry-a European Journal, 1998. **4**(3): p. 389-396.
65. Lei, M., P.G. Li, Z.B. Sun, and W.H. Tang, *Effects of organic additives on the morphology of calcium carbonate particles in the presence of CTAB.* Materials Letters, 2006. **60**(9-10): p. 1261-1264.

66. Kim, I.W., E. DiMasi, and J.S. Evans, *Identification of mineral modulation sequences within the nacre-associated oyster shell protein, n16.* Crystal Growth & Design, 2004. **4**(6): p. 1113-1118.
67. Gotliv, B.A., L. Addadi, and S. Weiner, *Mollusk shell acidic proteins: In search of individual functions.* Chembiochem, 2003. **4**(6): p. 522-529.
68. Gerbaud, V., D. Pignol, E. Loret, J.A. Bertrand, Y. Berland, J.C. Fontecilla-Camps, J.P. Canselier, N. Gabas, and J.M. Verdier, *Mechanism of calcite crystal growth inhibition by the N-terminal undecapeptide of lithostathine.* Journal of Biological Chemistry, 2000. **275**(2): p. 1057-1064.
69. Gaskin, D.J.H., K. Starck, and E.N. Vulfson, *Identification of inorganic crystal-specific sequences using phage display combinatorial library of short peptides: A feasibility study.* Biotechnology Letters, 2000. **22**(15): p. 1211-1216.
70. DeOliveira, D.B. and R.A. Laursen, *Control of calcite crystal morphology by a peptide designed to bind to a specific surface.* Journal of the American Chemical Society, 1997. **119**(44): p. 10627-10631.
71. Collino, S., I.W. Kim, and J.S. Evans, *Identification of an "acidic" C-terminal mineral modification sequence from the mollusk shell protein Asprich.* Crystal Growth & Design, 2006. **6**(4): p. 839-842.
72. Belcher, A.M., X.H. Wu, R.J. Christensen, P.K. Hansma, G.D. Stucky, and D.E. Morse, *Control of crystal phase switching and orientation by soluble mollusc-shell proteins.* Nature, 1996. **381**(6577): p. 56-58.
73. Belcher, A.M., in *Biomineralization*, E. Bäuerlein, Editor. 2000, Wiley-VCH: Weinheim. p. 247.
74. Unwin, P.R., *Concluding Remarks - Crystal growth and nucleation: tracking precursors to polymorphs.* Faraday Discussions, 2007. **136**: p. 409-416.

10 Appendix

10.1 List of Abbreviations

a	activity
A	area
A_N	numerical aperture
ACC	amorphous calcium carbonate
AUC	Analytical Ultracentrifugation
c	molar concentration
C	electrode intercept
CNT	classical nucleation theory
d_D	thickness of dialysis membrane
d_{LM}	definite limit of optical resolution
D	diffusion coefficient
f	frictional coefficient
f_H	HELMHOLTZ free energy per molecule
F	HELMHOLTZ free energy
F_A	FARADAY constant, F_A = 96,485 C mol^{-1}
F_b	buoyant force
F_c	centrifugal force
F_d	frictional force
G	Gibbs energy
h	PLANCK constant, h = $6.626 \cdot 10^{-34}$ J s
k	BOLTZMANN constant, k = $1.381 \cdot 10^{-23}$ J K^{-1}
$\hat{k}$	nucleation rate
$\hat{k}_0$	kinetic prefactor
K	microscopic equilibrium constant of Ca^{2+}/CO_3^{2-} ion pair formation in clusters
K_1, K_2,…	equilibrium constant characterizing the carbonate buffer equilibrium OR the multiple binding equilibrium
K’	macroscopic equilibrium constant of Ca^{2+}/CO_3^{2-} ion pair formation in clusters

m	mass
M	molecular weight
n	amount of substance
n_r	refractive index
N	number of particles in a supersaturated system
N_A	AVOGADRO's number, $N_A = 6.022 \cdot 10^{23}\,mol^{-1}$
NCNT	non-classical nucleation theory
p	pressure
P	permeability
PILP	polymer induced liquid precursor
r	radius
$\vec{r}$	position vector
R	universal gas constant, R = 8.314 J K^{-1} mol^{-1}
s	supersaturation ratio
s_{AUC}	sedimentation coefficient
SEM	scanning electron microscope/microscopy
T	temperature
TEM	transmission electron microscope/microscopy
U	potential
v	molecular volume
$\bar{v}$	partial specific volume
v_e	electron velocity
v_{AUC}	velocity of a sedimenting particle
V	volume
w	number of ions/ion pairs/particles bound in clusters
W	number of ions/particles in a subcritical system
WAXS	wide angle x-ray scattering
x	number of calcium ions that bind a carbonate ion (microscopic parameter)
z	valency; number of electrons transferred
γ	surface GIBBS energy
η	viscosity

θ	BRAGG angle
λ	number of ions that readjust the buffer equilibrium after the removal of a single carbonate ion
λ_{dB}	DE BROGLIE wavelength
λ_{LM}	wavelength of light
Λ	percentage of a species of the carbonate buffer equilibrium
μ	chemical potential
ν	multiple binding equilibrium parameter
ρ	density
ρ_m	molecular number density
σ	surface tension
φ	selectivity coefficient
Ψ	diffusion parameter
ω	angular velocity